

In situ Infrared Spectroscopy under Hydrothermal Conditions

Application for Aqueous Phase Reforming

Kamila Koichumanova

**IN SITU INFRARED SPECTROSCOPY
UNDER HYDROTHERMAL CONDITIONS
APPLICATION FOR AQUEOUS PHASE REFORMING**

DISSERTATION

Kamila Koichumanova

Graduation committee:

Prof. dr. ir. J. W. M. Hilgenkamp, chairman	University of Twente
Prof. dr. ir. Leon Lefferts, promoter	University of Twente
Prof. dr. K. Seshan, promoter	University of Twente
Dr. Barbara Mojet, assistant promoter	University of Twente
Prof.dr. S.R.A. (Sascha) Kersten	University of Twente
Prof. dr. Ir. R.G.H. (Rob) Lammertink	University of Twente
Prof.dr.ir. E.J.M. (Emiel) Hensen	Eindhoven University of Technology (TU/e)
Prof. dr. J.H. (Harry) Bitter	Wageningen UR (University & Research centre)
Prof. dr. Thomas Bürgi	University of Geneva, Switzerland

The research described in this thesis was carried out at the Catalytic Processes and Materials (CPM) group of the University of Twente, The Netherlands.

This research was performed within the framework of the CatchBio programme. The author gratefully acknowledges the support of the Smart Mix Program of the Netherlands Ministry of Economic Affairs, Agriculture and Innovation and the Netherlands Ministry of Education, Culture and Science, project number 053.70.002.



CatchBio

Cover design and cover photo: Kamila Koichumanova

Printed by: Gildeprint – www.gildeprint.nl

Copyright © Kamila Koichumanova, 2015.

All rights reserved. No part of this document may be reproduced or transmitted in any form or by any means, electronic, mechanical, photocopying, recording or otherwise without prior written permission of the copyright holder.

Author's email: kamilakoichumanova@gmail.com

ISBN number 978-90-365-3963-0

DOI-number: 10.3990/1.9789036539630

**IN SITU INFRARED SPECTROSCOPY
UNDER HYDROTHERMAL CONDITIONS**

APPLICATION FOR AQUEOUS PHASE REFORMING

DISSERTATION

to obtain
the degree of doctor at the University of Twente,
on the authority of the rector magnificus
Prof. dr. H. Brinksma
on account of the decision of the graduation committee,
to be publicly defended
on Wednesday October 7th 2015 at 14:45

by

Kamila Koichumanova

born on February 1st 1987

in Almaty, Kazakhstan

This dissertation has been approved by:

Prof. dr. ir. L. Lefferts (Promoter)

Prof. dr. K. Seshan (Promoter)

Dr. B.L. Mojet (Assistant Promoter)

Dedicated to my parents and my sister

Посвящается моим родителям и моей сестре

Aut non tentaris, aut non perfice
Either carry it through, or don't make the attempt at all
(Ovid)

Или вовсе не берись или доводи до конца
(Овидий)

Победу одержит лишь тот, кто сражается.

Table of Contents

Chapter 1. General introduction	1
1. <i>In situ</i> studies in heterogeneous catalysis	2
2. Characterization methods	2
3. Infrared Spectroscopy.....	4
4. Aqueous Phase Reforming (APR).....	6
5. <i>In situ</i> spectroscopic techniques in aqueous environments.....	9
6. ATR-IR spectroscopy as a tool for liquid (aqueous) phase <i>in situ</i> studies	10
Scope and outline of the thesis	11
References.....	12
Chapter 2. ATR-IR spectroscopic cell for <i>in situ</i> studies at solid-liquid interface at elevated temperatures and pressures.....	17
1. Introduction	18
1.1 <i>In situ</i> studies of chemical reactions.....	18
1.2 Total Internal Reflection.....	19
1.3 ATR-IR Cells.....	20
2. Design of the ATR-IR cell with a cylindrical IRE for high temperature / pressure applications.....	21
2.1 Peripheral (reactor) setup	22
2.2 Optical settings	23
2.3 IRE materials.....	25
2.4 Catalyst immobilization method	26
2.5 Results of spray coating catalysts on ZnSe IRE.....	28
3. Hydrodynamics of the flow in the Tunnel cell.....	30
3.1 Modelling and simulation of the fluid dynamics in the ATR-IR cell.....	31
3.2 Flow simulations.....	32
3.3 Experimental validation of ATR-IR cell with ZnSe IRE with and without catalyst layer.....	38
4. Conclusions.....	41
5. Acknowledgements.....	41
6. References.....	42
Chapter 3. Towards stable catalysts for the aqueous phase conversion of ethylene glycol for renewable hydrogen.....	47
1. Introduction	48
2. Experimental Section	49

2.1 Catalyst preparation	49
2.2 Catalyst characterization	49
2.3 Kinetic experiments.....	50
2.4 ATR-IR experiments	50
3. Results and Discussion	51
4. Conclusions.....	58
5. Acknowledgements.....	58
6. References.....	58
7. Supplementary information	61

Chapter 4. An *in situ* ATR-IR spectroscopy study of aluminas under aqueous phase reforming conditions **63**

1. Introduction	64
2. Experimental.....	67
2.1 Catalyst preparation	67
2.2 Catalyst characterization.....	67
2.3 Catalyst immobilization	67
2.4 ATR-IR spectra acquisition.....	68
2.5 Temperature Programmed Oxidation	69
2.6 Raman spectroscopy	69
2.7 Solid state ¹ H and ²⁷ Al MAS NMR analysis	69
3. Results.....	70
3.1 <i>In situ</i> ATR-IR spectra and peak assignments	70
3.2 Influence of temperature - stepwise heating.....	71
3.3 ATR-IR spectra in presence of ethylene glycol	72
3.4 Direct heating scheme	74
3.5 Raman spectroscopy	75
3.6 ²⁷ Al MAS NMR spectroscopy	75
3.7 ¹ H MAS NMR spectroscopy.....	76
3.8 Temperature programmed oxidation.....	77
4. Discussion.....	77
4.1 Influence of temperature on boehmite formation.....	77
4.2 Direct vs. stepwise heating.....	78
4.3 Boehmite formation from γ -Al ₂ O ₃	79
5. Conclusions.....	81
6. Acknowledgements.....	81
7. References.....	81
8. Supplementary information	84

Chapter 5. <i>In situ</i> ATR-IR studies in aqueous phase reforming of hydroxyacetone on Pt/ZrO₂ and Pt/AlO(OH) catalysts: the role of aldol condensation	87
1. Introduction	88
2. Experimental	89
2.1 Catalyst preparation	89
2.2 Catalyst characterization	89
2.3 Acidity measured by NH ₃ TPD and Pyridine adsorption IR spectroscopy	90
2.4 <i>In situ</i> ATR-IR spectroscopy	90
2.5 ATR-IR data processing	91
2.6 DFT calculations of IR spectra	92
3. Results	92
3.1 Catalyst characterization	92
3.2 <i>In situ</i> ATR-IR results	93
3.3 Acidity of supports studied by IR of pyridine adsorption and TPD NH ₃	98
3.4 Characterization of deactivated catalysts and supports	100
4. Discussion	101
4.1 Hydroxyacetone appearance in the cell	101
4.2 Hydroxyacetone washout with water	103
4.3 Adsorbed CO – water gas shift reaction	103
4.4 Identification of adsorbed species	105
4.5 Nature of the support in aldol condensation	108
4.6 Deactivation of the catalysts due to coke formation	108
5. Conclusions	109
6. Acknowledgements	109
7. References	110
8. Supplementary Information	113
Chapter 6. Conclusions and Recommendations	119
Summary	125
Краткое содержание	127
Samenvatting	131
Acknowledgements	133
List of Scientific Contributions	135

Chapter **1**

General introduction

Introduction

1. *In situ* studies in heterogeneous catalysis

The performance of a catalyst in a chemical reaction can be evaluated based on the quantities of the converted reactants or of the reaction products, as well as on product selectivities. A clear correlation between the activity of the catalyst and its (surface) structure is key for catalyst development in heterogeneous catalysis. In heterogeneous catalysis, reactants are converted on the surface of the catalyst, in particular on specific locations called “active sites”. The nature of the active site can be influenced by its environment since catalysts undergo various physical and chemical changes under the reaction conditions. Therefore, understanding the structure of the active sites under realistic reaction conditions is essential for understanding the reaction sequences that take place. Traditionally, correlation of the catalyst activity with its structure is established based on the evaluation of the properties of catalyst before (fresh) and after (used) the reaction. This approach gives indirect information about the active site, whereas characterization of the catalyst during the reaction, called “*in situ*” (Latin for “on site”), provides direct information about the state of the active site and the structure of the surface species. The simultaneous measurement of the catalytic activity and selectivity is additional information that can be used to unravel the catalytic reaction sequence. Generally, this approach is called “*operando*” (Latin for “working”).

Several reviews have been published in the last two decades emphasizing the importance of *in situ* and *operando* studies for catalyst design [1, 2]. The development of new analytical techniques, in particular, spectroscopic approaches has allowed one to gain fundamental information about catalyst structures in the working state. Most of the *in situ* techniques have been reviewed extensively in recent years [3-7].

2. Characterization methods

A number of analytical techniques are available for catalyst characterization. The main principle utilized in all techniques is a comparison of the signal sent to the sample with the signal received from the sample. Therefore, clear understanding of the interaction of the radiation with the sample is essential. In general, analytical techniques can be classified based on the types of excitation (photons, electrons, ions, electromagnetic field, heat, neutrals; inward arrows in **Figure 1**) or by type of radiation gathered (outward arrows in **Figure 1**).

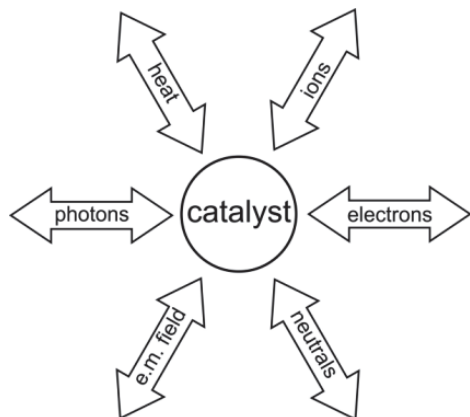


Figure 1. Diagram representing most of characterization techniques based on type of excitation (inward arrow) and obtained information (outward arrow). Reproduced from ref. [8].

Some of the most common characterization techniques used in heterogeneous catalysis are summarized in **Table 1** together with some examples of the information gathered from the techniques. They involve techniques that allow identification of the reaction intermediates (FTIR, NMR, UV-Vis) or state of the catalyst under controlled environments (XRD, Raman, XPS, XAS, TPO/TPR, TEM, SEM). Most of the current techniques require special conditions in order to collect information (*e.g.*, high vacuum in TEM, SEM, STEM) and/or to increase the signal to noise ratio. Several recent developments allow operation at close to ambient gas pressures (XPS, environmental-SEM).

Information collected from the surface of the catalyst can also contain information about the reactant, products or intermediates. Data analysis in this case becomes a challenging task, since surface species have to be distinguished from the bulk species. Additionally some of the species may have no role in the reaction, called “spectator species”, thus they need to be excluded from the reaction pathways of interest. Another aspect of *in situ* investigation is its applicability at conditions realistic to catalysis, *e.g.*, higher temperatures and pressures. Since most of the reactions are performed at temperatures higher than room temperature and pressures higher than atmospheric pressure, performing *in situ* studies requires heating of the samples and/or creating high pressure of the reactants/solvents. This can be particularly difficult to realize in spectroscopic cells. Heat transfer, mass transfer, and hydrodynamics of the flow have to be investigated and adjusted in order to ensure the proper reaction conditions.

High temperatures and pressures can also influence the signal strength or create distortions in phenomena utilized in the spectroscopic method. Broadening of the signal, baseline shift, etc. are examples of such changes. Thermal stability and chemical resistance of the materials used in building spectroscopic cells are also important aspects in the development.

Table 1. Common characterization tools used in catalysis [8, 9].

Technique	Excitation type (wavelength)	Information gathered
X-Ray Fluorescence (XRF)	Photons (0.01 nm – 10 nm)	Elemental composition
X-Ray Diffraction (XRD)		long range structural order (XRD) short range structural order (X-ray absorption fine structure)
X-Ray Photoelectron Spectroscopy (XPS)		Elemental composition, oxidation state
X-Ray Absorption (XAS) (EXAFS, XANES)		Coordination environment and oxidation state of metals and metal ions
UV-Vis Spectroscopy	Photons (UV: 10 nm – 380 nm), (visible: 380 – 700 nm)	Electronic d-d and charge transfer transitions of transition metal ions
Infrared (IR) Spectroscopy	Photons (700 nm – 1 mm)	Vibrational spectra of reaction mixtures and adsorbed molecules
Raman Spectroscopy		Vibrational spectra of metal oxides and organic deposits, such as coke
Electron Energy Loss Spectroscopy (EELS)	Electrons	Lattice vibrations, vibrational modes of adsorbed species, electronic transitions
Transmission/Scanning/Scanning Tunneling Electron Microscopy (TEM / SEM / STM)	Electrons (<1 Å)	Surface structure, size and shape of supported particles
Thermal Gravimetric Analysis (TGA)	Heat	Oxidation temperatures of carbon deposits, coke, desorption of adsorbed molecules
Temperature Programmed Oxidation / Reduction / Desorption (TPO / TPR / TPD)	Heat	Oxidation/reduction temperatures of metals, coke, desorption of adsorbed molecules
Nuclear Magnetic Resonance (NMR)	Electromagnetic Field (frequency 400-700 MHz / 0.5 – 1 m)	Identification of molecular structure formed via chemical shift values
Solid State MAS NMR (Magic angle spinning)		

3. Infrared Spectroscopy

IR spectroscopy is a versatile technique applied in surface characterization of the catalyst (surface hydroxyls, Brønsted, Lewis acid - base sites). A general selection rule of IR spectroscopy is a change of dipole moment during the excitation. This distinguishes Infrared from Raman spectroscopy, where the selection rule requires the change in molecular polarizability during the vibration. One of the common applications of IR spectroscopy is a characterization of surface properties based on interaction with probe molecules (CO, NO, pyridine, etc.). The correlation between the frequency of IR bands of probe molecule with the strength of the bond to the surface was first reported by Eischens and collaborators [10]. In their work, different frequencies for CO adsorbed on Cu, Pt, Ni and Pd metal particles dispersed on high surface area Cab-o-sil support were observed. Later, a theoretical explanation was given by Blyholder and coworkers [11], suggesting different extents of the bonding of CO (through the electron lone pair of the

carbon atom) to the metal and π back-donation from the d orbitals of the metal to the carbon-oxygen antibonding orbital.

The introduction of Fourier-Transform infrared spectrometer utilizing a Michelson interferometer allowed higher signal to noise ratio and shorter scanning times. Several designs are available for FTIR spectroscopy based on the nature of the analyzed sample. Schematic drawings of the most common configurations are shown in **Figure 2**.

Transmission IR is one of the most commonly used techniques, where the sample is pressed into a self-supporting wafer or pellet and exposed to the gases of interest. In this case, IR light is shone on a flat area of the pellet. (**Figure 2a**). *In situ* high temperature gas phase studies can be performed by heating a sample in a controlled gas environment. However, transmission FTIR setups still suffer from limitations such as (i) sample pellet has to be sufficiently thin to allow collection of sufficient transmitted IR intensity, (ii) catalyst has to be sturdy enough to allow production of self-supporting wafer, (iii) mass transport issues may exist in the cell.

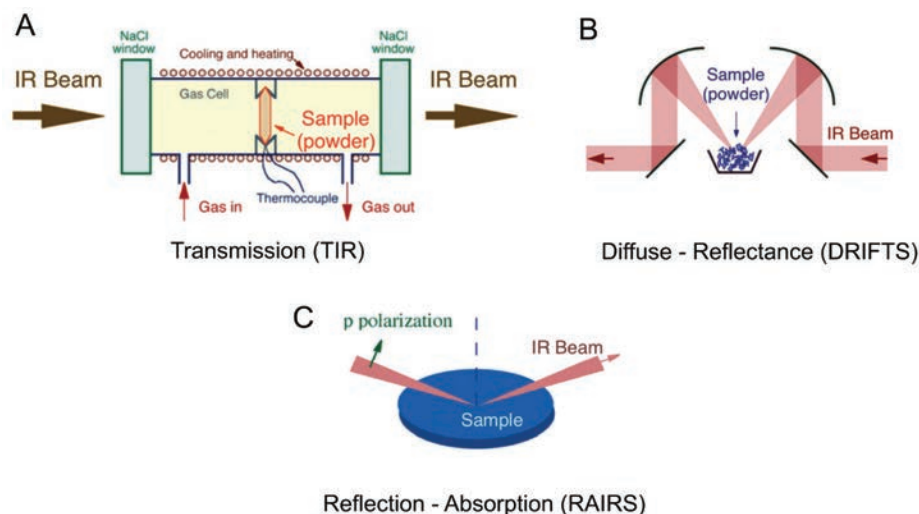


Figure 2. Common setups used for the characterization of catalytic samples using infrared absorption spectroscopy. Top, left: transmission (TIR) mode, top, right: diffuse reflectance (DRIFTS) mode, bottom, right: reflection-absorption (RAIRS) mode. Reproduced from ref. [12].

Diffuse Reflectance FTIR (DRIFT) spectroscopy, on the other hand, allows analysis of powder samples without the need for any particular sample preparation compared to transmission FTIR. In this case powder sample can be loosely placed in a basket and irradiated by IR beam (**Figure 2b**), while scattered light is collected using high area parabolic mirror. DRIFTS allows use of catalysts that are not easily pressed into pellets, moreover, the band intensities are several times higher than in transmission FTIR. However, reproducibility of DRIFTS is poor due to variations in scattering coefficients with cell geometry and sample loading procedure, which also complicate quantification

of the intensities. Additionally, only the top layer of the sample is probed, which can be an issue in high temperature studies due to temperature gradients across the bed.

Reflection-Absorption Infrared spectroscopy (RAIRS) is another type of FTIR where the beam is bounced from a flat reflective surface before collection (**Figure 2c**). RAIRS is widely used for characterization of low surface area samples. Low IR absorption intensities are typically obtained, however polarization modulation can improve signal to noise ratios.

Attenuated Total Reflectance Infrared spectroscopy, the central theme of this thesis, is another widely used technique for the characterization of powders and metal films. In the following sections, the working principle, advantages and drawbacks will be outlined. However, firstly one of the key application areas for the future, *in situ* studies of reactions in aqueous phase is introduced.

4. Aqueous Phase Reforming (APR)

Many of the liquid phase reactions *e.g.*, deoxygenation, hydrogenation, steam reforming occur in aqueous medium. One such case is Aqueous Phase Reforming (APR), which is analogous to the Steam Reforming (SR) process. In this case water is a reaction medium as well as a reactant. Industrial SR was developed for production of syngas (CO + H₂) from methane using water as an oxidant. This reaction is strongly endothermic and is carried out at temperatures above 750 °C and pressures below 25 bar, where water is present in the gas phase. In contrast, APR is carried out at milder temperatures (150 - 350 °C, 10 - 250 bar) and water is kept in liquid phase by applying pressure [13-15]. The phase diagram of water given in **Figure 3** shows the pressures required to keep water in liquid phase at elevated temperatures.

APR is typically used for valorization of waste aqueous streams containing 5 - 20% of organic compounds [16]. Such streams can come from food industry, paper production, biomass processing etc. In APR, these organic compounds can further be converted to hydrogen or alkanes without the need for evaporation of large amounts of water. Hydrogen produced in APR can be used in hydrogenation of bio-oil produced in biomass pyrolysis [17-20]. It was reported in literature, that bio-oil is poor in quality compared to crude oil due to its acidity and high oxygen content [21-23]. Thus, hydrogen from APR can be used in hydro-deoxygenation reactions of bio-oil lowering the acidity and removing oxygen in form of water. **Scheme 1** illustrates a sustainable approach in using biomass for the production of fuels.

Additionally, the conditions of APR favor the Water Gas Shift (WGS) reaction (**Equation 1**), which maximizes the hydrogen production from the carbon monoxide and water [14, 24].



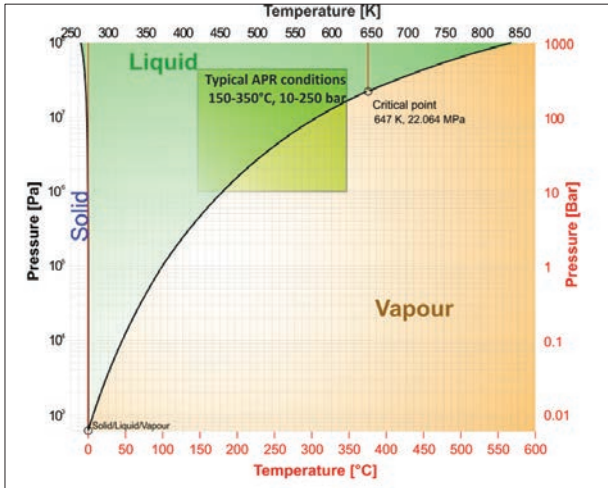
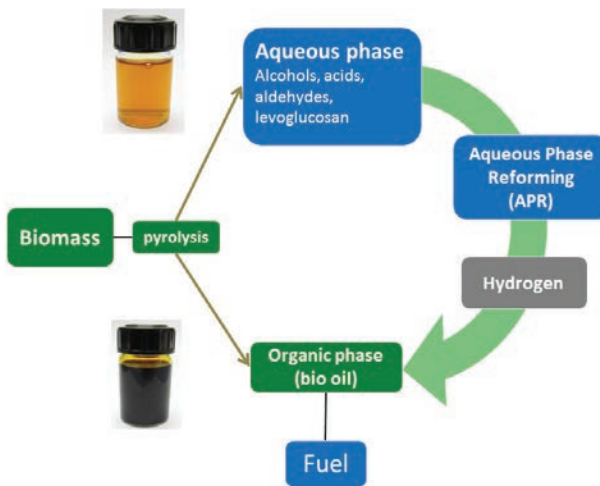


Figure 3. Phase diagram of water.



Scheme 1. APR in a biomass processing scheme.

The reaction equation (**Equation 2**) describes APR with WGS in the case of ethylene glycol, which is one of the most studied oxygenates:



Since H_2 , CO and CO_2 are formed as products of APR, consecutive methanation or Fischer-Tropsch reactions that consume hydrogen resulting in production of alkanes can negatively affect hydrogen yields [14]. Thus, selectivity towards hydrogen vs. alkanes has to be considered while developing efficient catalysts for APR targeted at hydrogen production.

Model compounds for APR reported in literature include methanol, ethanol, ethylene glycol, glycerol, sorbitol and acetic acid [18, 25-32]. Other compounds such as levoglucosan, hydroxyacetone (acetol), which are present in aqueous phase of bio-oil in significant quantities, are less studied. Thus, broadening the pool of model compounds for APR is a next step in the direction of converting the real aqueous phase obtained from biomass.

Noble metals supported on oxides have been reported as catalysts for APR [24, 33-39]. Pt, Ru, Rh, Ni and their bimetallic combinations are active in C-C cleavage forming adsorbed C_1 species. These C_1 species undergo steam reforming and subsequent WGS reaction to maximize hydrogen yields and minimize formation of alkanes. Metal oxides such as alumina, silica are the most used supports due to their ability to activate water creating surface hydroxyl groups [28, 29, 31, 40-42]. Thus, catalysts used in APR exhibit bifunctional properties favoring both reforming and WGS reactions. However, catalyst deactivation and stability of the catalyst supports under APR conditions are important issues that need to be addressed. A typical APR catalyst, Pt/ Al_2O_3 , has been reported to deactivate in hot compressed water medium due to support transformation, subsequent surface area collapse, Pt blockage and Pt sintering [17]. Hydration of alumina and formation of boehmite ($AlO(OH)$) has been reported under these conditions [31, 43, 44]. In this respect the use of hydrothermally stable supports for catalyst preparation such as zirconia or boehmite is a promising solution. Alternatively, carbon-based materials, such as activated/mesoporous carbon, carbon nanotubes (CNT) can also be used due to their chemical stability. Ru/CNT catalyst was reported as an efficient catalyst for APR of ethylene glycol [34].

Coking is a typical problem during steam reforming using Ni catalyst. In industry coking is minimized by operation at higher temperatures and high steam to carbon ratios (~ 3). In APR coking is also a severe problem. Side reactions that can take place on the support can lead to deposition of coke and deactivation of the catalyst. For example, acidity of the support can catalyze dehydration reactions resulting in the formation of unsaturated components. They can further oligomerize/polymerize into aromatics, which are precursors of coke. Thus, selection of the support with low acidity can suppress coke formation. Aldol condensation reaction of aldehydes and ketones can also lead to coke, for example aldol condensation of acetone was reported as a side reaction in steam reforming of acetone on Pt/ ZrO_2 catalyst [45]. Thus, understanding the reaction sequences that lead to condensation/oligomerization of the reactant or intermediate products on the surface of the catalyst, and correlation of the surface properties to the nature of coke precursors, can help in designing an active catalyst that is stable against deactivation.

5. *In situ* spectroscopic techniques in aqueous environments

Due to growing number of reactions performed in aqueous environments, such as the APR reaction described in section 4, the applicability of spectroscopic techniques, initially developed for gas-solid interfaces, has to be revised and improvements for liquid phase operation have to be considered. The recent review by Shi *et al.* [46] addresses these issues and summarizes the latest advances in *in situ* spectroscopic tools for aqueous environments with examples of vibrational techniques (FTIR, Raman), X-ray techniques (XAS, XPS, XRD), resonance techniques (MAS NMR, EPR), electron excitation, UV-Vis spectroscopy and imaging techniques (SEM, TEM, STM, AFM).

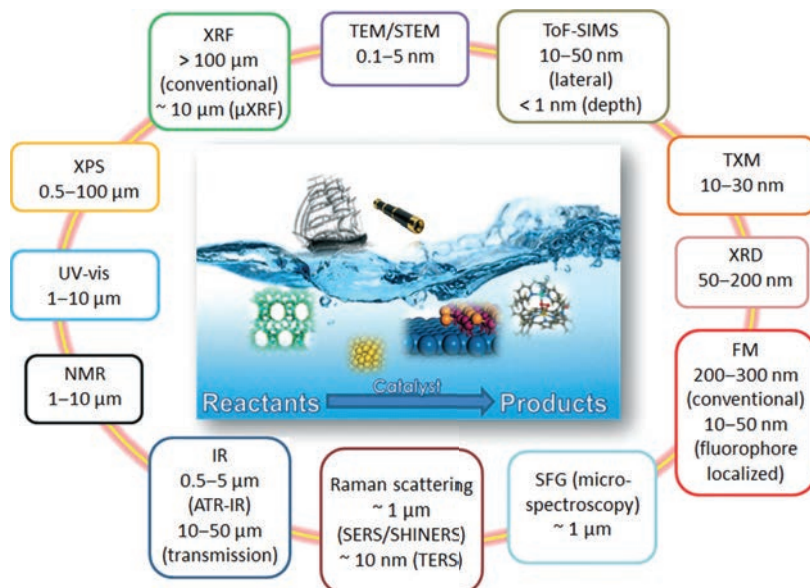


Figure 4. *In situ* characterization techniques applicable to aqueous phase catalytic systems along with their typical spatial resolutions. Abbreviations used in the figure: IR: infrared spectroscopy; ATR-IR: attenuated total reflectance infrared spectroscopy; SERS: surface enhanced Raman scattering; TERS: tip-enhanced Raman scattering; SHINERS: shell-isolated nanoparticle enhanced Raman scattering; SFG: sum frequency generation; UV-vis: ultraviolet-visible spectroscopy; XRD: X-ray diffraction; NMR: nuclear magnetic resonance; TEM: transmission electron microscopy; STEM: scanning transmission electron microscopy; TXM: transmission X-ray microscopy; FM: fluorescence microscopy; (μ)XRF: (micro)X-ray fluorescence; XPS: X-ray photoelectron spectroscopy; ToF-SIMS: time-of-flight secondary ion mass spectrometry. Reproduced from ref. [46].

Figure 4 provides a list of *in situ* spectroscopic and microscopic techniques that are applicable to aqueous environments along with their typical spatial resolutions. As shown in the figure, most of the techniques provide information about the state of the catalyst (its morphology, shape or oxidation state), however only few of the techniques provide information about the reaction adsorbates and reaction sequences. FTIR spectroscopy, in particular, ATR-IR spectroscopy, has the ability to provide this information.

6. ATR-IR spectroscopy as a tool for liquid (aqueous) phase *in situ* studies

Many studies have used FTIR at the gas/solid interface, using transmission IR or DRIFTS as discussed in the previous sections. However, the application of FTIR spectroscopy at the liquid/solid interface especially aqueous phase/solid interface requires an alternative approach in order to minimize absorption interference of IR light with water. Attenuated Total Reflection Infrared Spectroscopy (ATR-IR) allows one to overcome this and is an ideal tool to study reactions in the aqueous phase. In ATR-IR light is guided inside the optical element (typically ZnSe trapezoidal prism) due to multiple internal reflections, and reflected light is then collected by detector. A sample is deposited on the external surface of the element and the evanescent wave, generated at the reflection points between the element and the sample, penetrates into the sample (**Figure 5**). Thus, the benefit of ATR-IR spectroscopy is that it can be used not only for powders and thin films, but also for solids in the presence of highly absorbing liquids, *e.g.*, water.

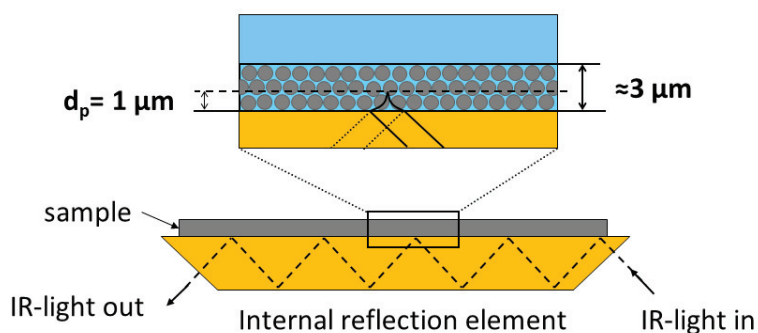


Figure 5. Principle of ATR-IR spectroscopy.

Several reviews have been published in the last decade [3, 46-50] summarizing the details of the ATR-IR technique and its applications in different reactions *e.g.*, inorganic ions sorption on metal oxy-hydroxides [50], nitrite/nitrate hydrogenation on Pd/Al₂O₃ [6, 51], hydrogenation of ethyl pyruvate in supercritical ethane over Pt/Al₂O₃ [49], selective oxidation of benzyl alcohol over Pd/Al₂O₃ [49], Knoevenagel condensation between benzaldehyde and ethyl cyanoacetate on aminopropyl-modified silica [3].

The ATR-IR cell designs vary depending on the shape of the optical element and the conditions of the reaction of interest. Flat flow-through cells are mostly used due to the simplicity in sample preparation, availability and price of the cells. Alternatively, ATR-IR cells with cylindrical optical elements are also available. In this case, the whole surface area of the element is used for reflections improving signal to noise ratio. Immerse ATR probes are also reported for batch type operations. In this case, the optical element is placed on the tip of the probe immersed in to the stirred tank reactor

providing information about the liquid composition. Extensive reviews on ATR-IR cell designs are available with details of the cell geometries and applications [3, 47, 52]. Further details of the ATR-IR spectroscopy and the design of the cylindrical "Tunnel" cell are provided in **Chapter 2**.

Scope and outline of the thesis

The aim of the work described in this thesis relate to the development of an *in situ* spectroscopic tool that is applicable for studies at the solid - liquid interface at the conditions of aqueous phase reforming reaction. The ATR-IR spectroscopy was chosen for this purpose based on its applicability to aqueous solutions as reported in literature. However, the conditions of APR reaction brought additional constraints for operation at high temperature/pressure aqueous conditions in the ATR-IR cell.

The details of the *in situ* ATR-IR cell and the experimental setup are given in **Chapter 2**. The optical and hydrodynamic aspects of the ATR-IR cell are also discussed together with the catalyst immobilization method.

In **Chapter 3** the performance of the Pt/Al₂O₃ catalyst in APR of ethylene glycol is discussed, with the results showing catalyst deactivation caused by support transformation and coverage of Pt particles with boehmite. The ATR-IR cell was used to confirm formation of boehmite and show its stability in hydrothermal conditions. The performance Pt/AlO(OH) catalyst was further studied, resulting in more stable and active catalyst compared to Pt/Al₂O₃.

The kinetics of alumina transformation into boehmite under hydrothermal conditions is discussed in **Chapter 4**, showing the applicability of ATR-IR spectroscopy for material chemistry studies. The results showed the delay of the transformation in the presence of Pt particles as well as oxygenates in the solution.

The application of ATR-IR spectroscopy for the investigation of surface adsorbate species during APR reaction is shown in **Chapter 5**. In particular, APR of hydroxyacetone on Pt/AlO(OH) and Pt/ZrO₂ catalysts is discussed showing the appearance of surface adsorbates on zirconia. Experimental evidence together with DFT calculations of IR spectra of possible products were used for peak assignments. Catalyst deactivation pathways are suggested based on the structures of the adsorbates.

Finally, **Chapter 6** summarizes the outcomes of the work and gives recommendations for future scientific investigations using the developed ATR-IR cell.

References

1. Bañares, M.A., *Operando spectroscopy: The knowledge bridge to assessing structure-performance relationships in catalyst nanoparticles*. *Advanced Materials*, 2011. **23**(44): p. 5293-5301.
2. Topsøe, H., *Developments in operando studies and in situ characterization of heterogeneous catalysts*. *Journal of Catalysis*, 2003. **216**(1-2): p. 155-164.
3. Andanson, J.M. and A. Baiker, *Exploring catalytic solid/liquid interfaces by in situ attenuated total reflection infrared spectroscopy*. *Chem Soc Rev*, 2010. **39**(12): p. 4571-84.
4. Foster, A.J. and R.F. Lobo, *Identifying reaction intermediates and catalytic active sites through in situ characterization techniques*. *Chem Soc Rev*, 2010. **39**(12): p. 4783-93.
5. Lamberti, C., A. Zecchina, E. Groppo, and S. Bordiga, *Probing the surfaces of heterogeneous catalysts by in situ IR spectroscopy*. *Chem Soc Rev*, 2010. **39**(12): p. 4951-5001.
6. Mojet, B.L., S.D. Ebbesen, and L. Lefferts, *Light at the interface: the potential of attenuated total reflection infrared spectroscopy for understanding heterogeneous catalysis in water*. *Chem Soc Rev*, 2010. **39**(12): p. 4643-55.
7. Vimont, A., F. Thibault-Starzyk, and M. Daturi, *Analysing and understanding the active site by IR spectroscopy*. *Chem Soc Rev*, 2010. **39**(12): p. 4928-50.
8. Niemantsverdriet, J.W., *Spectroscopy in Catalysis*. 2007: Wiley VCH.
9. Tinnemans, S.J., J.G. Mesu, K. Kervinen, T. Visser, T.A. Nijhuis, A.M. Beale, D.E. Keller, A.M.J. Van Der Eerden, and B.M. Weckhuysen, *Combining operando techniques in one spectroscopic-reaction cell: New opportunities for elucidating the active site and related reaction mechanism in catalysis*. *Catalysis Today*, 2006. **113**(1-2): p. 3-15.
10. Eischens, R.P. and W.A. Pliskin, *The Infrared Spectra of Adsorbed Molecules*, in *Advances in Catalysis*. 1958. p. 1-56.
11. Blyholder, G., *Molecular orbital view of chemisorbed carbon monoxide*. *Journal of Physical Chemistry*, 1964. **68**(10): p. 2772-2778.
12. Zaera, F., *Infrared Absorption Spectroscopy of Adsorbed CO: New Applications in Nanocatalysis for an Old Approach*. *ChemCatChem*, 2012. **4**(10): p. 1525-1533.
13. Huber, G.W., R.D. Cortright, and J.A. Dumesic, *Renewable alkanes by aqueous-phase reforming of biomass-derived oxygenates*. *Angewandte Chemie-International Edition*, 2004. **43**(12): p. 1549-1551.
14. Dumesic, J.A., E.L. Kunkes, R.R. Soares, and D.A. Simonetti, *An integrated catalytic approach for the production of hydrogen by glycerol reforming coupled with water-gas shift*. *Applied Catalysis B-Environmental*, 2009. **90**(3-4): p. 693-698.
15. Huber, G.W. and J.A. Dumesic, *An overview of aqueous-phase catalytic processes for production of hydrogen and alkanes in a biorefinery*. *Catalysis Today*, 2006. **111**(1-2): p. 119-132.
16. Hoang, T.M.C., A.K.K. Vikla, and K. Seshan, *Aqueous phase reforming of sugar derivatives: Challenges and Opportunities*, in *Biomass Sugars for non-fuel applications*. 2015, RSC Green Chemistry Series.
17. De Vlieger, D.J.M., B.L. Mojet, L. Lefferts, and K. Seshan, *Aqueous Phase Reforming of ethylene glycol - Role of intermediates in catalyst performance*. *Journal of Catalysis*, 2012. **292**: p. 239-245.

18. de Vlieger, D.J.M., A.G. Chakinala, L. Lefferts, S.R.A. Kersten, K. Seshan, and D.W.F. Brillman, *Hydrogen from ethylene glycol by supercritical water reforming using noble and base metal catalysts*. Applied Catalysis B: Environmental, 2012. **111-112**: p. 536-544.
19. DeVlieger, D.J.M., D.B. Thakur, L. Lefferts, and K. Seshan, *Carbon Nanotubes: A Promising Catalyst Support Material for Supercritical Water Gasification of Biomass Waste*. ChemCatChem, 2012. **4**(12): p. 2068-2074.
20. Vispute, T.P., H.Y. Zhang, A. Sanna, R. Xiao, and G.W. Huber, *Renewable Chemical Commodity Feedstocks from Integrated Catalytic Processing of Pyrolysis Oils*. Science, 2010. **330**(6008): p. 1222-1227.
21. Kersten, S.R.A., W.P.M. van Swaaij, L. Lefferts, and K. Seshan, *Options for Catalysis in the Thermochemical Conversion of Biomass into Fuels*, in *Catalysis for Renewables*. 2007, Wiley-VCH Verlag GmbH & Co. KGaA. p. 119-145.
22. Vitasari, C.R., G.W. Meindersma, and A.B. de Haan, *Water extraction of pyrolysis oil: The first step for the recovery of renewable chemicals*. Bioresource Technology, 2011. **102**(14): p. 7204-7210.
23. Lédé, J., F. Broust, F.T. Ndiaye, and M. Ferrer, *Properties of bio-oils produced by biomass fast pyrolysis in a cyclone reactor*. Fuel, 2007. **86**(12-13): p. 1800-1810.
24. Ciftci, A., D.A.J.M. Ligthart, A.O. Sen, A.J.F. Van Hoof, H. Friedrich, and E.J.M. Hensen, *Pt-Re synergy in aqueous-phase reforming of glycerol and the water-gas shift reaction*. Journal of Catalysis, 2014. **311**: p. 88-101.
25. Shabaker, J.W., R.R. Davda, G.W. Huber, R.D. Cortright, and J.A. Dumesic, *Aqueous-phase reforming of methanol and ethylene glycol over alumina-supported platinum catalysts*. Journal of Catalysis, 2003. **215**(2): p. 344-352.
26. Shabaker, J.W., G.W. Huber, R.R. Davda, R.D. Cortright, and J.A. Dumesic, *Aqueous-phase reforming of ethylene glycol over supported platinum catalysts*. Catalysis Letters, 2003. **88**(1-2): p. 1-8.
27. Skoplyak, O., M.A. Barteau, and J.G. Chen, *Reforming of oxygenates for H₂ production: Correlating reactivity of ethylene glycol and ethanol on Pt(111) and Ni/Pt(111) with surface d-band center*. Journal of Physical Chemistry B, 2006. **110**(4): p. 1686-1694.
28. Ciftci, A., B. Peng, A. Jentys, J.A. Lercher, and E.J.M. Hensen, *Support effects in the aqueous phase reforming of glycerol over supported platinum catalysts*. Applied Catalysis A: General, 2012. **431-432**: p. 113-119.
29. Luo, N., X. Fu, F. Cao, T. Xiao, and P.P. Edwards, *Glycerol aqueous phase reforming for hydrogen generation over Pt catalyst - Effect of catalyst composition and reaction conditions*. Fuel, 2008. **87**(17-18): p. 3483-3489.
30. Mikkola, J.P., A.V. Kirilin, A.V. Tokarev, E.V. Murzina, L.M. Kustov, and D.Y. Murzin, *Reaction Products and Transformations of Intermediates in the Aqueous-Phase Reforming of Sorbitol*. Chemsuschem, 2010. **3**(6): p. 708-718.
31. Koichumanova, K., A.K.K. Vikla, D.J.M. de Vlieger, K. Seshan, B.L. Mojet, and L. Lefferts, *Towards Stable Catalysts for Aqueous Phase Conversion of Ethylene Glycol for Renewable Hydrogen*. Chemsuschem, 2013. **6**(9): p. 1717-1723.
32. Wawrzetz, A., B. Peng, A. Hrabar, A. Jentys, A.A. Lemonidou, and J.A. Lercher, *Towards understanding the bifunctional hydrodeoxygenation and aqueous phase reforming of glycerol*. Journal of Catalysis, 2010. **269**(2): p. 411-420.

33. Davda, R.R., J.W. Shabaker, G.W. Huber, R.D. Cortright, and J.A. Dumesic, *Aqueous-phase reforming of ethylene glycol on silica-supported metal catalysts*. Applied Catalysis B-Environmental, 2003. **43**(1): p. 13-26.
34. De Vlieger, D.J.M., L. Lefferts, and K. Seshan, *Ru decorated carbon nanotubes-a promising catalyst for reforming bio-based acetic acid in the aqueous phase*. Green Chemistry, 2014. **16**(2): p. 864-874.
35. El Doukkali, M., A. Iriondo, J.F. Cambra, I. Gandarias, L. Jalowiecki-Duhamel, F. Dumeignil, and P.L. Arias, *Deactivation study of the Pt and/or Ni-based γ -Al₂O₃ catalysts used in the aqueous phase reforming of glycerol for H₂ production*. Applied Catalysis A: General, 2014. **472**(0): p. 80-91.
36. Kim, H.D., H.J. Park, T.W. Kim, K.E. Jeong, H.J. Chae, S.Y. Jeong, C.H. Lee, and C.U. Kim, *Hydrogen production through the aqueous phase reforming of ethylene glycol over supported Pt-based bimetallic catalysts*. International Journal of Hydrogen Energy, 2012. **37**(10): p. 8310-8317.
37. Huber, G.W., J.W. Shabaker, and J.A. Dumesic, *Raney Ni-Sn catalyst for H-2 production from biomass-derived hydrocarbons*. Science, 2003. **300**(5628): p. 2075-2077.
38. Shabaker, J.W., G.W. Huber, and J.A. Dumesic, *Aqueous-phase reforming of oxygenated hydrocarbons over Sn-modified Ni catalysts*. Journal of Catalysis, 2004. **222**(1): p. 180-191.
39. Zhang, L., A.M. Karim, M.H. Engelhard, Z. Wei, D.L. King, and Y. Wang, *Correlation of Pt-Re surface properties with reaction pathways for the aqueous-phase reforming of glycerol*. Journal of Catalysis, 2012. **287**(0): p. 37-43.
40. Hesenov, A., B. Meryemoglu, S. Irmak, O.M. Atanur, and O. Erbatur, *Aqueous-phase reforming of biomass using various types of supported precious metal and raney-nickel catalysts for hydrogen production*. International Journal of Hydrogen Energy, 2010. **35**(22): p. 12580-12587.
41. Lehnert, K. and P. Claus, *Influence of Pt particle size and support type on the aqueous-phase reforming of glycerol*. Catalysis Communications, 2008. **9**(15): p. 2543-2546.
42. Manfro, R.L., A.F. Da Costa, N.F.P. Ribeiro, and M.M.V.M. Souza, *Hydrogen production by aqueous-phase reforming of glycerol over nickel catalysts supported on CeO₂*. Fuel Processing Technology, 2011. **92**(3): p. 330-335.
43. Jongerius, A.L., J.R. Copeland, G.S. Foo, J.P. Hofmann, P.C.A. Bruijninx, C. Sievers, and B.M. Weckhuysen, *Stability of Pt/ γ -Al₂O₃ catalysts in lignin and lignin model compound solutions under liquid phase reforming reaction conditions*. ACS Catalysis, 2013. **3**(3): p. 464-473.
44. Ravenelle, R.M., J.R. Copeland, W.G. Kim, J.C. Crittenden, and C. Sievers, *Structural Changes of γ -Al₂O₃-Supported Catalysts in Hot Liquid Water*. ACS Catalysis, 2011. **1**(5): p. 552-561.
45. Matas Güell, B., I.M.T.d. Silva, K. Seshan, and L. Lefferts, *Sustainable route to hydrogen - Design of stable catalysts for the steam gasification of biomass related oxygenates*. Applied Catalysis B: Environmental, 2009. **88**(1-2): p. 59-65.
46. Shi, H., J.A. Lercher, and X.Y. Yu, *Sailing into uncharted waters: Recent advances in the in situ monitoring of catalytic processes in aqueous environments*. Catalysis Science and Technology, 2015. **5**(6): p. 3035-3060.

47. Bürgi, T. and A. Baiker, *Attenuated Total Reflection Infrared Spectroscopy of Solid Catalysts Functioning in the Presence of Liquid-Phase Reactants*, in *Advances in Catalysis*, C.G. Bruce and K. Helmut, Editors. 2006, Academic Press. p. 227-283.
48. Zaera, F., *New advances in the use of infrared absorption spectroscopy for the characterization of heterogeneous catalytic reactions*. Chemical Society Reviews, 2014. **43**(22): p. 7624-7663.
49. Grunwaldt, J.D. and A. Baiker, *In situ spectroscopic investigation of heterogeneous catalysts and reaction media at high pressure*. Physical Chemistry Chemical Physics, 2005. **7**(20): p. 3526-3539.
50. Lefèvre, G., *In situ Fourier-transform infrared spectroscopy studies of inorganic ions adsorption on metal oxides and hydroxides*. Advances in Colloid and Interface Science, 2004. **107**(2-3): p. 109-123.
51. Ebbesen, S.D., B.L. Mojet, and L. Lefferts, *In situ ATR-IR study of nitrite hydrogenation over Pd/Al₂O₃*. Journal of Catalysis, 2008. **256**(1): p. 15-23.
52. Hind, A.R., S.K. Bhargava, and A. McKinnon, *At the solid/liquid interface: FTIR/ATR - the tool of choice*. Advances in Colloid and Interface Science, 2001. **93**(1-3): p. 91-114.

Chapter 2

ATR-IR spectroscopic cell for *in situ* studies at solid-liquid interface at elevated temperatures and pressures

The design and operation of an *in situ* ATR-IR cell applicable in aqueous conditions at elevated temperatures and pressures is described. Important aspects of the cell geometry and the sample immobilization method are discussed. The fluid flow pattern in the cell was simulated based on the incompressible Navier-Stokes equation. Concentration profiles were assessed using convection-diffusion model showing significant deviation from ideal plug flow. Experimental residence times of glycerol at different flow rates and temperatures agree well with simulations, demonstrating that the hydrodynamics of the reactor is accurately described despite the deviation from plug flow. Aqueous phase reforming of hydroxyacetone was used to validate the applicability of the cell at 230 °C, 30 bar for *in situ* catalytic studies in the presence of a Pt/ZrO₂ catalyst layer.

1. Introduction

1.1 *In situ* studies of chemical reactions

Investigations of chemical reactions and catalysts under the actual reaction conditions, *i.e. in situ* or *operando*, contribute largely to the understanding of the state of the catalyst and reaction pathways and help in the design of efficient catalysts [1-3]. Consequently, a growing number of publications are seen on fundamental studies of different chemical processes of commercial relevance. In this context, reactions in liquid phase utilizing homogenous or heterogeneous catalysts are important in various fields such as fine chemicals, pharmaceuticals, production of organic chemicals and biomass processing. The majority of such reactions use water as the reaction medium. Aqueous Phase Reforming (APR) is one such example, producing hydrogen and alkanes from waste biomass aqueous streams using noble metal catalysts supported on different metal oxides [4-6]. Typical conditions for APR include temperatures between 150 and 350 °C and pressures between 20 and 250 bar. Development of an analytical/spectroscopic tool that can be operated under such conditions would be extremely beneficial for catalyst development.

A number of analytical tools are available and can be used for *in situ* catalyst studies. However, the choice depends on (i) the type of information that is needed and (ii) applicability/limitations of the technique at the reaction conditions of interest, *e.g.*, need for high vacuum, reaction medium, *i.e.*, presence/absence of solvents, temperature and pressure. A number of techniques have been developed to be used *in situ*, for example, X-Ray Photoelectron Spectroscopy (XPS, Auger) [7-9], X-Ray Absorption Spectroscopy (XAS) [2, 10, 11], X-Ray Diffraction (XRD) [12, 13], Transmission/Scanning Electron Microscopy (TEM/SEM) [14], NMR [15, 16], Raman [11, 17] and Infrared Spectroscopy (IR) [3, 10, 18, 19]. Excellent reviews cited, discuss details of possibilities/limitations of these techniques.

IR spectroscopy is one of the most frequently used techniques for *in situ* investigations of heterogeneously catalyzed reactions. This is due to its broad applicability for studying sorption, surface intermediates, reaction sequences as well as surface characterization, *e.g.* acidity/basicity, bulk properties of catalysts. Many studies have used IR spectroscopy at the gas/solid interface, using transmission IR Spectroscopy or Diffuse Reflectance Infrared Fourier Transform Spectroscopy (DRIFTS) [20]. However, liquid/solid interface, especially aqueous phase/solid interface, requires a modified approach in IR spectroscopy in order to minimize absorption interference of IR light with water. Attenuated Total Reflection Infrared Spectroscopy (ATR-IR) allows to overcome this and is an ideal tool to study reactions in aqueous phase, *e.g.* APR, over solid catalysts, *in situ*, and provide better understanding of the catalyst development. Details of ATR-IR spectroscopy are discussed next.

1.2 Total Internal Reflection

Total internal reflection (**Figure 1**) occurs when light, *e.g.*, IR, approaches the boundary between two media of differing refractive indices, $n_1 > n_2$, from the side of the higher refractive index medium n_1 at an angle greater than the critical angle (θ_c). Then, light does not cross the boundary, but is reflected back and thus is kept within the original medium (n_1).

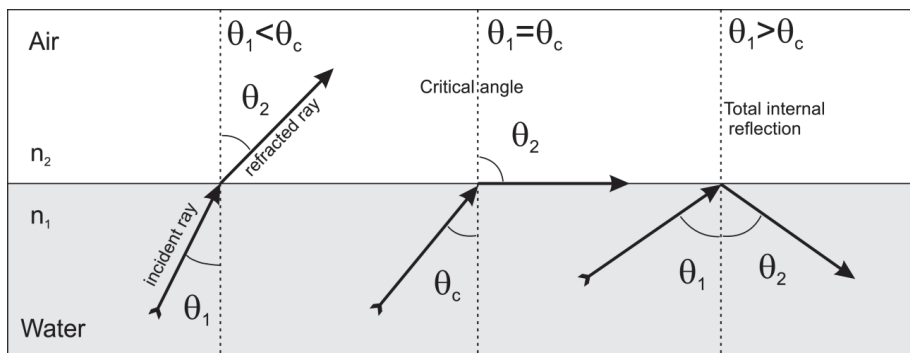


Figure 1. Different pathways of light at various incident angles for $n_1 > n_2$.

The relationship between the angles of incidence (θ_1) and refraction (θ_2) is described according to Snell's law (**Equation 1**):

$$n_1 \sin \theta_1 = n_2 \sin \theta_2 \quad (\text{Eq. 1})$$

Thus, the critical angle can be calculated according to (**Equation 2**) when $\theta_2 = 90^\circ$:

$$\theta_c = \theta_1 = \arcsin (n_2/n_1) \quad (\text{Eq. 2})$$

However, even when the light is totally reflected back, an electromagnetic wave called "evanescent wave" penetrates beyond the boundary surface [21, 22]. This wave propagates in the direction parallel to the boundary and decays (attenuates, hence the name ATR) exponentially in the perpendicular direction. In the case of an *in situ* ATR-IR experiment where a layer of heterogeneous catalyst is coated on an Internal Reflection Element (IRE), the boundary is between these two solids. In this case the evanescent wave can only exist when refractive index of the IRE is higher than that of the catalyst sample being studied; otherwise, the light is completely absorbed by the sample. Depth of penetration of the evanescent wave is given by **Equation 3**, below

$$d_p = \frac{\lambda}{2\pi n_1 \sqrt{(\sin^2 \theta - (\frac{n_2}{n_1})^2)}} \quad (\text{Eq. 3})$$

where n_1 - refractive index of IRE, n_2 is calculated based on **Equation 4**, below

$$n_{eff} = \sqrt{(1 - \varphi)n_i^2 + \varphi n_j^2} \quad (\text{Eq. 4})$$

where n_i - refractive index of solid (dense solid catalyst), n_j - refractive index of medium filling the pores, *e.g.* air or water, θ - angle of incidence, φ - porosity of the catalyst layer.

The total reflection spectroscopy was developed in 1967 by Harrick [22] and Fahrenfort [23]. Various studies have been reported over the years using ZnSe, Ge, Silicon, or Diamond as IRE for ATR-IR spectroscopy.

1.3 ATR-IR Cells

A number of ATR-IR cell designs are available and include both commercial and home-built designs (**Figure 2**). Typically, cell geometry has to be selected based on the type of investigation that it is made for, for instance adsorption/desorption phenomena on thin films or porous layers can be studied in a horizontal cell with or without flow of reactants (**Figure 2a**) [19, 21, 24-28]. In this design the catalyst is deposited on top of the IRE. Information is collected from the catalyst/IRE interface, thus allowing to record spectra of adsorbates. Such cell geometry also allows to study when reactants flow above the catalyst layer. Cell designs with cylindrical IRE are available and can also be used (**Figure 2b**). In this case complete surface of the IRE is utilized whereas in the flat cell geometry only the top part of the IRE is used [5, 29-31]. Immersion probe ATR designs have also been developed [18] to monitor dissolved concentration in the liquid phase in a batch type reactor. In this design, the IR light is tunneled in an immersion tube and the total reflection phenomenon takes place at the tip of the probe (**Figure 2c**). Another design for a batch reactor includes the ATR-IR crystal mounted in the bottom of the reactor/autoclave (**Figure 2d**), and therefore composition of the liquid phase can be probed together with, in some cases, spectra of the suspended catalyst particles [32-34].

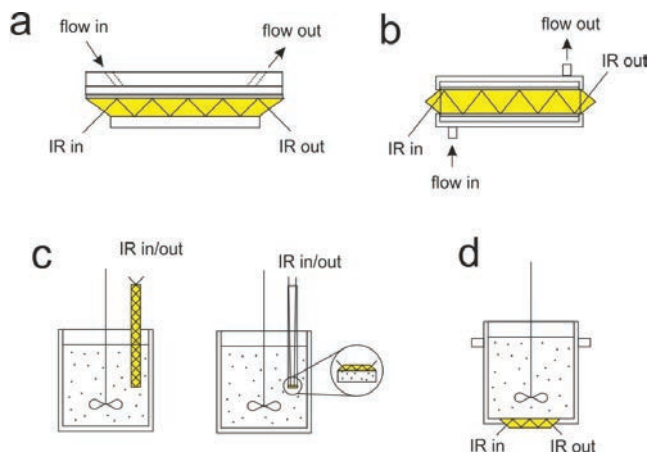


Figure 2. Schematic designs of various ATR-IR cells (a) flow cell with flat IRE, (b) circular flow cell with cylindrical IRE, (c) stirred batch reactors with IR fiber optics or immerse probes cylindrical or flat, and (d) stirred batch reactor with bottom mounted flat IRE.

As seen from the different cell designs, not only the shape of the IRE varies, but also how the IR beam is directed to the IRE and how the contact between IRE and solid/liquid interface is arranged. The flat or cylindrical cells require immobilization of

the catalyst layer on IRE. Thus, a sample coating method, resulting in a mechanically stable layer, that provides good contact with the surface of the IRE, is essential. In the case of batch cells (**Figure 2c, d**), the contact between catalyst and IRE is significantly poor compared to flat or circular flow cells because the catalyst is suspended. When the cells are used in flow mode, hydrodynamics of flow and concentration gradients have to be considered. Further, when the cell is installed in the sample chamber of IR spectrometer, mirror setting within the chamber needs optimization to allow focusing of the light on the edge of the IRE. This is less complicated when using fiber optics or immersion probes, since the cell can be located outside of the IR chamber.

Both flat and circular cells can be used at higher pressures and temperatures, however, use of flat cells limit the pressures that can be applied. This is due to the spacers used for sealing as well as the susceptibility of the flat IRE crystal to cracking. Thermal stability of the sealing materials is also a limiting factor. The circular cell with the cylindrical IRE (**Figure 2b**) has the advantage that the pressure is evenly distributed on all sides of IRE and hence higher operating pressures are possible.

Goals of this study are (i) description of the aspects that are critical while designing an *in situ* ATR-IR cell with cylindrical IRE for high temperature, high pressure applications, (ii) incorporation of a catalytic layer on the IRE thus making the cell suitable for *in situ* catalytic studies, (iii) determine the hydrodynamics of the flow and mass transfer and (iv) description of a working cell and demonstration using APR of a model oxygenate (hydroxyacetone) as a case study.

2. Design of the ATR-IR cell with a cylindrical IRE for high temperature/pressure applications

The following aspects have been taken into account in the design of the ATR IR cell keeping in mind that it would be applied mainly for *in situ* catalytic studies under APR conditions. It should, therefore, incorporate a flow system for continuous reaction study and be applicable at higher temperatures (up to 300 °C) and pressures (up to 100 bar). Minimal dead volume, reasonably short switching times between reactants/solvents and reasonably fast heating rates were additional requirements. Mechanical stability of the catalyst layer against washout was another design consideration. **Figure 3** shows a photo and the details of a standard commercial ATR-Tunnel cell (Axiom, USA) which was further modified in cooperation with Axiom (adjustments in O-rings and heating cartridge) for high temperature/pressure conditions.

The cell consists of the stainless steel block with a cylindrical channel (**Figure 3c, 7**), inlet (8) and outlet (10) perpendicular to the main channel and a thermocouple (9) installed in a pocket hole at the middle point of the reactor. The Internal reflection element (rod, length 3.25 inch, diameter 0.25 inch) coated with a sample (6) was placed coaxially inside the channel and held in the proper place using Kalrez O-rings (5). Kalrez

Spectrum (7075, Du Pont) O-rings made of carbon-filled elastomers were used due to their thermal stability (up to 327 °C) as well as their chemical resistance to hot water, steam, various organic media, especially acidic solutions. Finally, two metal bushings with threading were screwed inside the metal body from both ends to pressurize the O-rings. The two metal O-rings (4) were used to regulate the extent of deformation of the elastomer O-rings. The two conical mirrors (3) were placed inside the metal bushings in such way that the IR beam is focused on the tip of the IRE. A mask (2) was placed in the metal bushing blocking the central part of the beam. The inlet and outlet of the reactor have Swagelok fittings which allow connection with 1/16 inch SS tubing.

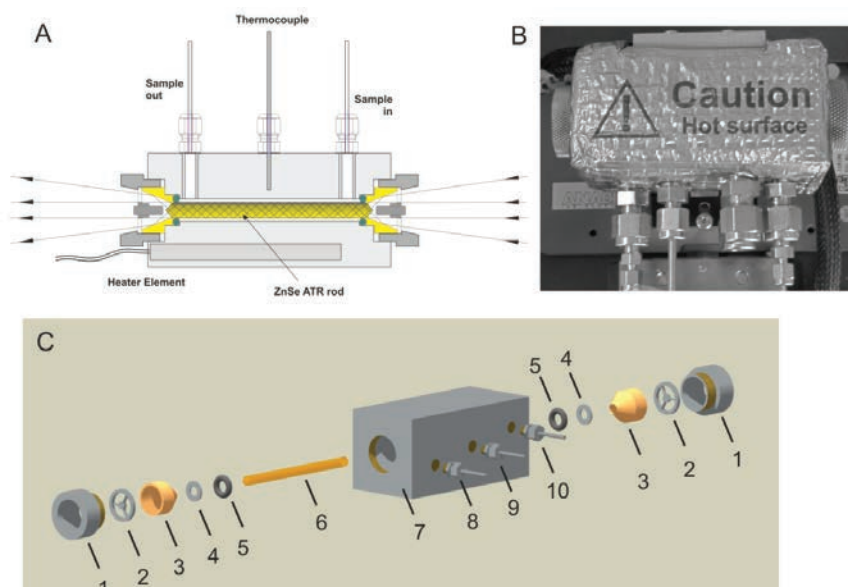


Figure 3. (a) Schematic drawing of the ATR-IR Tunnel cell, (b) photo of the Tunnel cell (top view), (c) 3D drawing of the ATR-IR cell with major components: 1 - metal bushing with threading, 2 - mask, 3 - conical mirror, 4 - metal O-ring (2 pieces), 5 - Kalrez O-ring, 6 - ZnSe internal reflection element, 7 - metal body of the cell, 8 - inlet, 9 - thermocouple connection, 10 - outlet.

It is important to note that a mechanical damage of the O-rings was observed after few consecutive experiments, due to local overheating, resulting in a leakage of moisture inside the IR chamber. The shape of the O-ring has to be inspected frequently with timely replacement. Temperature measured at both ends of the cell showed the existence of the gradient of typically around ± 30 °C at the set point of 230 °C. This is a limitation of the current cell and due to the fact that the tips of the IRE are exposed to ambient surroundings.

2.1 Peripheral (reactor) setup

The scheme of the reactor setup is given in a **Figure 4**. ATR-IR cell was installed in the chamber of an FTIR spectrometer (Bruker, Tensor 27) with an mercury-cadmium-

telluride detector (MCT D316/6-L). Liquid reactants (oxygenate solution, hydrogen-, oxygen-, or carbon monoxide-saturated water) were fed from stirred glass bubble tanks using an HPLC pump (Dionex P680). Pressure in the system was kept at the required level by a back-pressure regulator. The cell was heated to the desired reaction temperature by a rod-shaped heating cartridge (diameter 5 mm, length 6 cm) inserted into the body of the cell and the resulting temperature was measured at the outer wall of the reaction zone (**Figure 3**). For a better heating efficiency, liquid flow was preheated in a coil-shaped preheater (1/16 inch tubing wrapped around an aluminium cylinder with a heating cartridge). The temperature of the pre-heater was set to the same temperature as in the reaction zone. The flow leaving the cell was cooled in a counter-flow heat exchanger with water as a cooling agent.

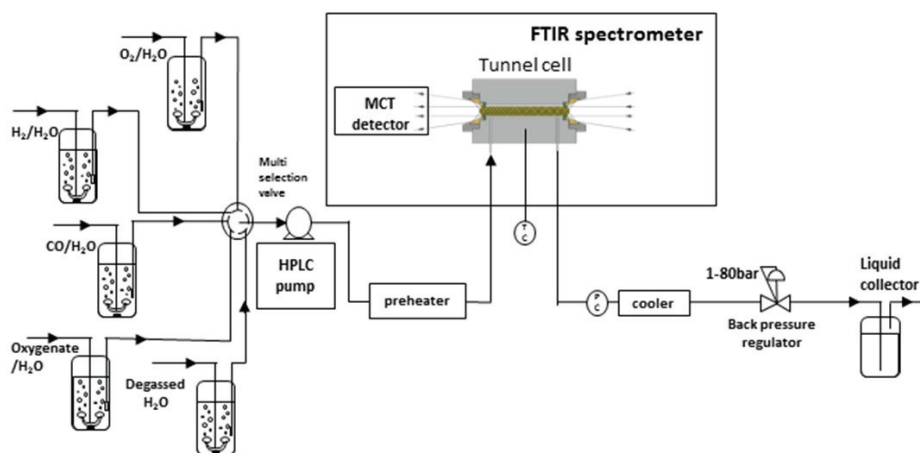


Figure 4. Scheme of the setup with ATR-IR cell installed in the measuring chamber of FTIR spectrometer.

2.2 Optical settings

Position of the IRE/tunnel cell in the Bruker spectrometer is shown in **Figure 5**. A ZnSe rod was used as the IRE in the current study (details in the next section). The path of the IR beam is also shown in the figure. Light beam from the IR source passes through an aperture wheel and is reflected by a series of flat/parabolic mirrors to focus the beam at the center of the sample compartment. The cell is mounted on a quick-lock baseplate (Bruker) and is adjustable in height and angle, so that the cross section of the beam matches the diameter of the IRE around the axial middle point of the ZnSe rod.

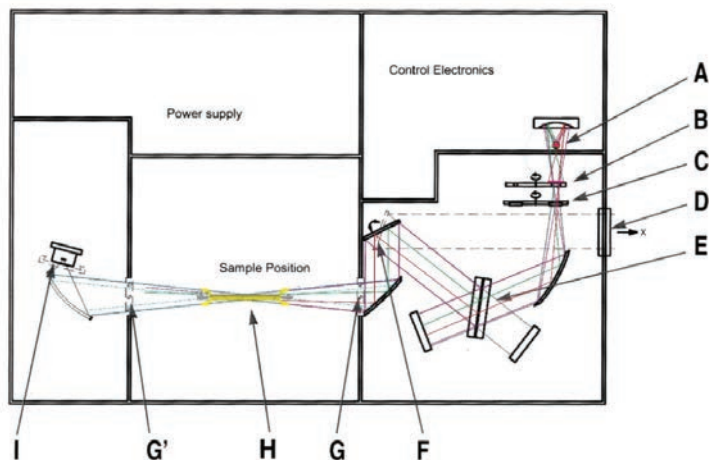


Figure 5. Schematic drawing of the optical alignment of the cell in the IR chamber. A – IR source, B – aperture wheel, C – Filter wheel, D – IR light outlet port, E – beam splitter, F – switch mirror, G, G' – sample compartment window, H – IRE with catalyst layer (cell not shown), I – detector.

The ATR-IR cell used by us is equipped with conical mirrors having thin gold coating (inner diameter 6 mm, outer diameter 15 mm, length 10 mm, **Figure 6**), located at both the conical ends of the IRE [35]. The mirrors are kept at an angle of 22.5° to the central axis (axial direction) allowing reflection of the incoming beam to hit the tip of the rod at almost perpendicular angle (see **Figure 6a**). The central part of the IR beam is blocked by a mask (**Figure 6b**), preventing the light going through the rod without being bent. The pathways of the innermost and the outermost ray in the IR beam that are not blocked by the mask are shown in **Figures 6b and c**, respectively. The small difference in the incident angles of the two rays (21.2° and 17°) leads only to a small variation in the incident angle at the ZnSe/sample contact point (45.5° till 47.3°). This is important since the angle of incidence determines the penetration depth (**Equation 3**) and thus should be kept constant for the whole IR beam to allow uniform sampling depth.

The IR beam undergoes multiple bounces through the length of the rod, before exiting, in a pathway that can be described by a circular movement with a forward displacement (screw type movement) according to Harrick [22]. In order to visualize this, **Figure 7** below, accordingly, shows a photo indicating the pathway of a green laser beam incident on the conical tip of the ZnSe IRE. However, if this screw type pathway has an influence on the incident angle and subsequent penetration depth has not been described clearly yet.

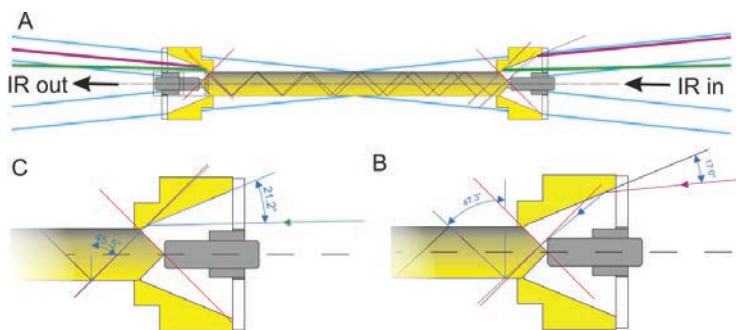


Figure 6. Optical paths of two limiting rays (purple and green). (a) Both rays at the inlet and outlet conical mirrors, (b) reflection of the most parallel ray at the inlet conical mirror, (c) reflection of the most tilted ray at the inlet conical mirror.

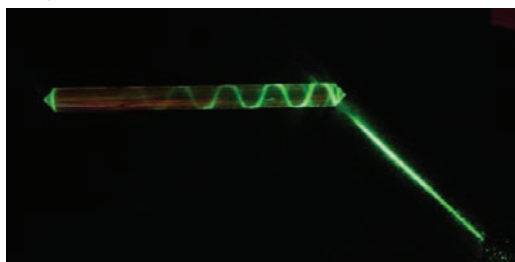


Figure 7. The pathway of a green laser beam incident on the conical tip of the cylindrical ZnSe IRE.

2.3 IRE materials

Internal reflection element in the Tunnel cell has the shape of a rod with conical ends of 45° . Normally, the material for the IRE has to be selected according to the application desired, based on optical, chemical and thermal properties. In our study the IRE should be transparent for radiation in the mid-IR region ($2 - 20 \mu\text{m}$ or $4000 - 500 \text{cm}^{-1}$), be chemically resistant to aqueous medium containing dissolved acids, aldehydes or alcohols and have relatively high refractive indices (approximately >2.1 , since most of metal oxides, used as catalyst supports have refractive index around $1.4-2.0$). Thermal resistance is also a key parameter, since the studied reaction (APR) requires temperatures up to 250°C . Optical and chemical properties of common IRE materials are summarized in **Table 1**.

It can be seen that diamond would be an ideal choice; however, the size and shape of the IRE would make it economically not viable. Germanium has the highest refractive index which is beneficial for the analysis of high absorbing materials, such as carbon, however it loses its optical properties above 125°C . Silicon also has high refractive index and good chemical resistance, but has a high cut-off edge (1500cm^{-1}), thus it is not suitable for studies in the fingerprint region for most of the organic molecules ($1500 - 500 \text{cm}^{-1}$). Zinc sulfide has optimal, chemical and thermal stability, as does zinc selenide,

however, ZnSe has a higher refractive index and wider spectral range. Therefore, ZnSe was selected as IRE material in the current study.

Table 1. Optical and chemical properties of IRE materials [36]. (+) and (-) represent advantages and drawbacks in using the material in water or diluted organic solutions at 230 °C/30bar.

Material	Spectral working range, cm^{-1}	Refractive index [37] at 2000 cm^{-1}	Maximum working temperature, °C	Chemical properties
Zinc selenide (ZnSe)	20000 - 700	2.43	300	(+) insoluble in water and organic solvents; (-) incompatible with acids and strong alkalis; non-hygroscopic, (+) hard, (-) brittle
Germanium (Ge)	5000 - 900	4.02	125 (becomes opaque)	(+) Insoluble in water; (-) soluble in hot H_2SO_4 , nitric acid and molten alkalis; resists hot conc. HCl and HF acids, and hot conc. NaOH solution; (-) slow oxidation in air; (+) hard and (-) brittle
Silicon (Si)	9400 - 1500	3.43	300	(+) insoluble in water, (+) insoluble in most acids and bases; insoluble in HF; (-) soluble in HF and HNO_3 mixture; (+) hard.
Zinc sulphide (ZnS)	14200 - 1000	2.25	300	(+) Insoluble in water and normal bases; (-) soluble in some acids; (-) reacts to strong oxidizing agents; slightly soluble in nitric acid and sulfuric acid; (+) slightly harder and more chemically resistant than ZnSe, (-) brittle
Diamond	45000 - 10	2.40		(+) Hard scratch resistant, (+) insoluble in acids and bases, stable in strong oxidizing agents.

2.4 Catalyst immobilization method

Normally, the shape of the internal reflection element (flat plate or cylindrical rod) determines the catalyst immobilization method. Eventually, the resulting sample layer has to meet the same requirements independent of the method used, which are: (i) homogeneous distribution (at almost 100% coverage) of the sample (catalyst) on the surface of the IRE preventing exposure of bare ZnSe, (ii) constant layer thickness, (iii) thickness of the layer must be between $1 \mu\text{m}$ (greater than the depth of penetration) and tens of microns (to minimize diffusion limitations), and (iv) the layer should be mechanically stable against shear forces caused by liquid flow.

Methods used for coating of an IRE with solid materials include (i) deposition of a solid (catalyst) slurry with subsequent drying, (ii) dip coating, and (iii) vapor phase deposition, and are described well in literature [10, 24, 26, 38-43]. **Table 2** summarizes the advantages and drawbacks of different immobilization methods.

Slurry deposition method is typically used for flat trapezoidal plate IREs [24, 26, 38, 39, 41]. In this method catalyst particles are suspended in an aqueous slurry, and the

slurry is then wet coated on the surface of the crystal and dried (these steps carried out repeatedly to achieve required thickness) at room temperature for 24 h. Additional thermal treatment can be done in order to densify the layer and remove excess water from the pores. Layer thicknesses of 3.5 μm for Pt/Al₂O₃ [38] and 5 μm for Pd/Al₂O₃ [39] have been reported earlier by us.

In contrast to slurry deposition method, dip coating method is generally used for immobilizing the sample on a cylindrical IRE [29, 43]. According to this method, the cylindrical rod is dipped vertically into the slurry of the sample, withdrawn slowly (1 cm/min) and left for drying. It is to be noted that the conical ends of the rod have to be protected during dip coating. A Teflon holder was constructed in order to prevent coating of the end cones [43].

Table 2. Comparison of different sample immobilization methods. (+) and (-) represent advantages and drawbacks

Parameter/ Method	Slurry deposition by solvent evaporation	Vapor deposition	Dip coating	Spray coating
Shape of the IRE	(-) Applicable only for flat IRE	(-) Applicable only for flat IRE	(+) applicable for cylindrical IRE	(+) applicable for both flat and cylindrical IRE
Solvent	(+) Water can be used as a solvent	(+) No solvent	(-) Solvent with viscosity higher than water is needed	(-) Solvent with low boiling point
Total deposition time including drying time	(-) 24 h	-	(-) 24 h	(+) 1 h
Resulting layer homogeneity	(+) Homogeneous layer thickness	(+) Homogeneous layer thickness on flat IRE	(+) Homogeneous layer thickness	(-) Low control over layer homogeneity
Layer mechanical stability	(+) Stable	(+) Susceptible to peel off	(+) Stable	(+) Stable

Poston *et al.* [29] deposited a thin silica layer by withdrawing a cylindrical ZnSe rod from a suspension of a silica sol followed by gelling. Isopropanol was used as the solvent and total of 15 dips were performed to achieve a thickness of 700 nm. Bremer *et al.* [43] reported dip coating of ZnSe IREs with poly-amideimide polymer with subsequent thermal curing at 250 °C. Thickness of the layer reported was between 99 – 254 μm . In general, the important parameters controlling the layer thickness in dip coating are viscosity of the solvent used and withdrawal speed [44].

Vapor deposition method is mainly used for coating flat IREs with thin metal layers, *e.g.* Pt or Pd [21, 28]. Aguirre *et al.* [28] reported formation 20 nm layer of Pt by

this method. However, Ferri *et al.* [42] showed possibility to create Pt layers with thicknesses of a few nm by varying experimental parameters. Physical vapor deposition has also been used for coating Al_2O_3 on IRE [42], resulting in a layer of amorphous alumina of about 100 nm thick. It is important to note, that metal layers can peel-off when contacted with water. If the substrate is a flat plate, even distribution of sample over the entire IRE can be achieved using vapor deposition method, since the deposition is preferred in a specific direction. In case of a cylindrical IRE the resulting layer may be uneven, thus an alternative method has to be developed.

A spray coating method has been successfully developed in our group and reported earlier [5]. In this method sample particles (ultra-sonicated or ball-milled to breakdown particles) were suspended in isopropanol (150 mg of sample in 20 mL isopropanol), and sprayed on a heated substrate (40 °C) using commercially available single-action air-brush (Badger model 200, nozzle diameter 0,7 mm, Badger Air-Brush Co.) with 1,5 bar N_2 pressure. The spraying was then repeated with intermediate drying until the desired amount of sample was deposited. As in dip coating method, the choice of solvent is important, especially because the boiling point of a solvent is critical (isopropanol b.p. is 82.6 °C) for easier evaporation. While the slurry deposition and vapor deposition methods cannot be used for coating of non-flat, *i.e.* cylindrical surfaces, dip coating and spray coating are both suitable. In dip coating, multiple dipping steps with drying in between each dipping (up to 24 h) are required, which is time-consuming. In spray coating, however, solvent evaporates simultaneously with particles deposition, shortening total deposition time down to 1 h. Therefore, spray coating was used in the current study and results are discussed in the next section.

2.5 Results of spray coating of catalysts on ZnSe IRE

In **Figure 8** typical SEM images of Pt/ZrO₂ (a and c) and AlO(OH) (b and d) catalyst layers spray-coated on a ZnSe rod are presented. The loading of the catalysts was kept similar (~ 10 mg). The images at low magnification (**Figure 8a, b**, scale bar 100 μm) show uniform distribution of the catalyst on the ZnSe substrate. Bare ZnSe crystal surface can be seen in **Figure 8a** after part of the catalyst layer was scratched off. The images at higher magnification (**Figure 8c, d**, scale bar 10 μm) show that the two materials have different morphology and layer porosity. Pt/ZrO₂ has smaller grain size with voids at the sample-crystal interface, whereas the AlO(OH) layer seems better attached to the crystal, creating less porosity. In both cases variations in layer thickness caused by inhomogeneity of spraying was observed. The averaged thickness of the layer was estimated from multiple SEM images; Pt/ZrO₂ layer has an average thickness of 27±17 μm, whereas AlO(OH) has an average thickness of 8±6 μm. In both cases the thickness of the layer is much greater than penetration depth (< 1μm, see **Table 3**) calculated according to **Equation 3**, but at the same time small enough to minimize diffusion limitations. The void fraction of the layer was estimated based on amount of

the catalyst, thickness of the layer and surface area of the crystal, resulting in 0.95 and 0.66 for Pt/ZrO₂ and Pt/AlO(OH), respectively. This void fraction of the layer is significantly higher than the porosity of the original catalyst (0.62 for Pt/ZrO₂ and 0.48 for Pt/AlO(OH)) and especially the zirconia layer contains a large volume fraction of inter-particle space. Visual image of the rod after coating can also be seen in **Figure 8e**.

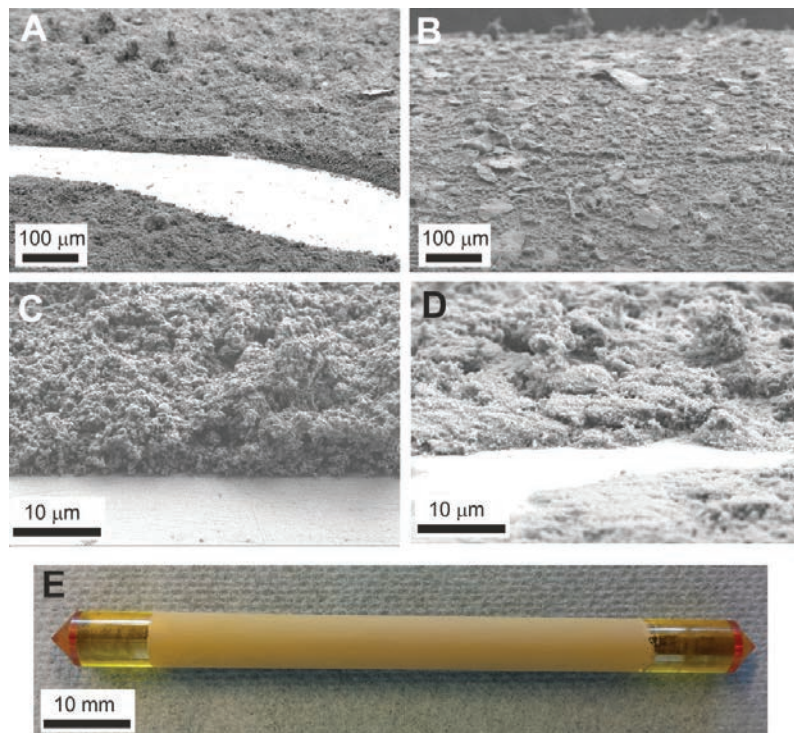


Figure 8. SEM image of Pt/ZrO₂ (a and c) and AlO(OH) (b and d) layers spray-coated on ZnSe rod, (e) typical photo of a coated rod.

Catalyst layers were also tested for mechanical stability in water flow (2 mL/min) at 25 °C and at 230 °C/30 bar for 12 h, showing only around 10 % of the weight loss based on the difference in catalyst loading before and after the exposure to water.

As was mentioned in the introduction section, the depth of penetration of IR light defines the probed thickness of the layer. For materials with different refractive indices depth of penetration will be different as well. This has to be taken into account when comparing the peak intensities in IR spectra for different samples. **Table 3** shows calculated depths of penetration for typical catalysts (Pt/ZrO₂, Pt/AlO(OH)) and respective supports used in APR studies based **Equations 3 and 4**. The penetration depth was also calculated for cases when no catalyst was present and ZnSe in contact with air or water. Optical constants for materials used were taken from literature [37, 45-49]. Effective refractive index of Pt/ZrO₂ was calculated using **Equation 4** to account for the effect of Pt, assuming a mixture of 99.7 vol. % ZrO₂ and 0.33 vol.% Pt (calculated

from 1.2 wt.% Pt/ZrO₂ and the densities of ZrO₂ and Pt). Similarly, in case of Pt/AlO(OH), a mixture of 99.8 vol.% AlO(OH) and 0.17 vol.% Pt was assumed based on calculation of 1.2 wt.%Pt/AlO(OH) and densities of AlO(OH) and Pt. The results showed that the effect of Pt on depth of penetration for porous catalyst layer is minimal due to low Pt content.

Table 3. Calculated depth of penetration for different catalysts and supports in water and air. Porosity of the layer consisted of porosity of the material and porosity due to coating.

Sample	Depth of penetration, μm		
	4000 cm^{-1}	2000 cm^{-1}	650 cm^{-1}
ZnSe/air	0.28	0.57	1.83
ZnSe/H ₂ O	0.34	0.73	2.31
AlO(OH)/air	-	0.75	-
AlO(OH)/H ₂ O	-	0.89±0.07	-
ZrO ₂ /H ₂ O	-	0.76±0.05	-
1.5 wt. % Pt/AlO(OH)/H ₂ O	-	0.89±0.07	-
1.5 wt. % Pt/ZrO ₂ /H ₂ O	-	0.77±0.05	-

In general, the depth of penetration is greater in water than in air for both in absence and presence of a catalyst layer. Depth of penetration is higher when the catalyst/support is present on ZnSe (ZnSe/H₂O and AlO(OH)/H₂O). The penetration depth also varies with the wavelength as seen from the results of ZnSe/air and ZnSe/H₂O. At lower wavenumbers it is almost three times higher than in the fingerprint region, causing higher IR intensities.

3. Hydrodynamics of the flow in the Tunnel cell

Aim of the *in situ* experiments in the ATR-IR cell is to mimic the processes that occur on the surface of the catalyst and together with kinetic experiments, come to a description of the reaction pathways, intermediates (active vs. spectator) and chemistry at the catalyst surface.

In order to do this, a clear understanding of transport phenomena in the ATR-IR cell, which functions as a catalytic reactor, is necessary. Experiments with ATR-IR in this study are carried out using step changes in the concentration of the reactant. In addition, it is important to keep in mind that the experimental IR spectra as presented are an average 139 single spectra collected during 1 min. Each spectrum is an average over all points of total reflection along the length of the IRE. Due to the high length/diameter ratio of the Tunnel cell, concentration gradients along the length in the longitudinal direction may exist giving rise to non-uniform reaction rates in the axial direction. Thus, a clear description of the liquid flow pattern through the cell (plug flow vs mixed),

including residence time distributions, and concentration gradients is essential for judging transient ATR-IR data. The following sections describe the results of simulations of the transport phenomena in the bare ATR-IR cell used. Additionally, internal diffusion issues in the catalyst layer should also be evaluated, however this is beyond the scope of the current simulations.

3.1 Modelling and simulation of the fluid dynamics in the ATR-IR cell

The velocity field, u and pressure, p are governed by the Navier-Stokes equations which describe conservation of mass and momentum.

$$\nabla u = 0 \quad (\text{Eq. 5})$$

$$u \cdot \nabla u = -\frac{1}{\rho} \nabla p + \mu \nabla^2 u \quad (\text{Eq. 6})$$

where ρ is density and μ is the dynamic viscosity of fluid, water in the case of aqueous media, at the corresponding temperature and pressure.

The following conditions have been applied for the steady state flow simulations: (i) "no slip" boundary conditions at the walls (*i.e.*, outermost layer/molecules of fluid are considered as stuck to the surfaces past which it flows), (ii) the superficial velocity corresponds to the flow flowrate at the inlet of the cell, (iii) open boundary condition at the outlet. Mass transfer is governed by diffusion and convection:

$$\frac{\partial c}{\partial t} + u \cdot \nabla c = \nabla \cdot D \nabla c \quad (\text{Eq. 7})$$

where c is the molar concentration, D is the solute aqueous diffusion coefficient at the corresponding temperature T and pressure computed using Stokes-Einstein equation:

$$\frac{D_{T_1}}{D_{T_2}} = \frac{T_1}{T_2} \frac{\mu_{T_2, p_2}}{\mu_{T_1, p_1}} \quad (\text{Eq. 8})$$

Further, for the simulation of mass transfer in the cell, the following was applicable, (i) No flux boundary conditions were set for the walls, (ii) the velocity field obtained from the steady state flow simulation was used to simulate the transient solute transport, (iii) a step residence time distribution was obtained by setting the initial concentration at zero and the inlet at a constant concentration c_0 .

The equations were solved numerically using Finite Element Analysis in Comsol Multiphysics software, version 4.3. The simulations were performed for (i) acetone solution at three different temperatures and autogenic pressures and (ii) for glycerol solution at room temperature and atmospheric pressure (**Table 4**).

Table 4. Physical properties of acetone and glycerol solutions used in the simulations.

Solution	Temperature (°C)	Pressure (bar)	Density of water (kg/m ³)	Dynamic viscosity of water (Pa*s)	Diffusion coefficient (m ² /s)
2.5 wt. % acetone / water	25	1	997	8.91 E-4	1.28 E-9
	100	20	959	2.83 E-4	5.04 E-8
	230	30	827	1.23 E-4	1.56 E-8
9.2 wt. % glycerol / water	25	1	997	8.91 E-4	1.06 E-9

The cell geometry in **Figure 3a** was reproduced for simulations. The length of the outlet tube was kept small in the simulations to reduce computational time. The simulations were performed using an unstructured grid with tetrahedral elements as this allows the best description of a cylindrical rod. The element size was varied according to the dimension of the channel with smaller elements for the annular reactor domain than for the inlet and outlet tubes. In the annular region, the maximum element size was $1.5 \cdot 10^{-4}$ m for the radial faces and $2 \cdot 10^{-4}$ m for the axial faces. For the inlet and outlet tubes, the maximum element size was increased to $4 \cdot 10^{-4}$ m and $5 \cdot 10^{-4}$ m, respectively. The volume of the tetrahedral elements were set for the entire mesh to a maximum size of $1.93 \cdot 10^{-3}$ m. Mesh independency was evaluated based on the symmetry and smoothness of the parabolic velocity profile. The concentration was averaged across the whole reactor length within $1 \mu\text{m}$ from the surface of the ZnSe rod (further called “mean surface concentration”) for comparison with experimental spectra. It is important to recall here that the penetration depth of IR light in the ATR-IR is also around $1 \mu\text{m}$. The outlet concentration was calculated using the mixed-cup average according to **Equation 9**, where A is the surface area of the IRE:

$$\bar{c} = \frac{\int c \cdot u \cdot dA}{\int u \cdot dA} \quad (\text{Eq. 9})$$

3.2 Flow simulations

Figure 9a shows a color trace of local velocities for 27 equally distributed cross section planes along the length of the IRE. Laminar regime was found to be present everywhere along the length of the IRE, except for two turbulent zones at the inlet and outlet (**Figure 9a, b**). A parabolic profile for the local velocities was observed (**Figure 9c and d**). Velocity was maximum in the middle of the annular ring reaction zone around ZnSe (**Figure 9d**) and was $1.6 \cdot 10^{-3}$ m/s. Local velocity at the inlet and outlet reached values of $4.85 \cdot 10^{-3}$ m/s which is three times higher than the maximum

velocity along the length. Local turbulences at inlet and outlet are caused by change in geometry which narrows the width of the channel.

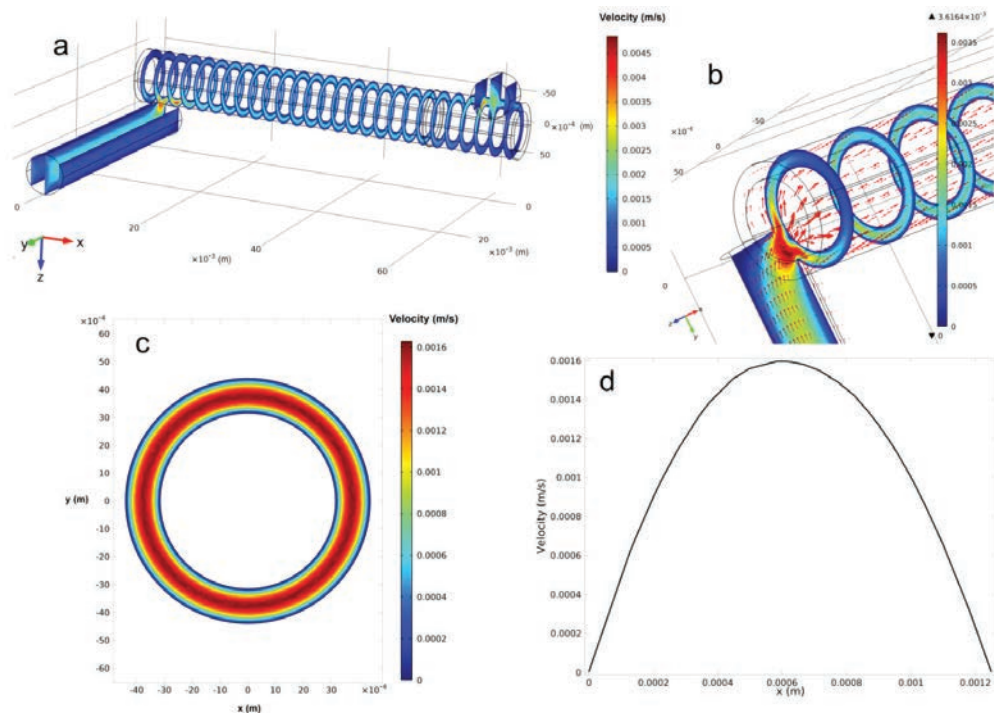


Figure 9. (a) 3D color map of the velocity field in flow-through ATR-IR cell filled with water, (b) zoomed in inlet tube with red arrows representing streamlines; (c) 2D velocity magnitude at the cross section plane located at the half length of the cell; (d) parabolic profile at half length of the cell.

Importance of the inlet position and shape has been discussed by Aguirre *et al.* [28] for a flow-through flat ATR-IR cell. It was concluded that circular-shape entrance/exit causes significant distortions in the concentration profile at the end points of the cell. Optimized position and shape of the entrance and exit ports was suggested, *i.e.* line-shaped entrance located as close as possible to the ends for flat cells. Urakawa *et al.* [27] further showed that for experiments with two different feeds separate inlets help to minimize mixing (avoid interference) in the volume before the IRE.

In our case, the entrance/exit geometries were circular in shape. From **Figure 9 b** it can be seen that the flow is distributed uniformly in the annual ring along the axial direction justifying the choice of the geometry of the inlet and outlet. It was, however, difficult to have multiple inlets, as suggested by Urakawa *et al.* [27], because our experiments at the higher temperatures required pre-heating of the feeds. Incorporating separate preheating zones for different feeds was not possible in the current set up. If the system will be modified in the future this has to be taken into consideration.

Residence time distributions for acetone at 25 °C, 1 bar and 230 °C, 30 bar were simulated. The cell was first filled with water and then the flow was switched to a solution of 2.5 wt. % acetone in water. For the simulations the injection point was selected close to inlet orifice of the cell to reduce calculation time, thus any effect of the pre-heater volume of the experimental set up was neglected.

Figure 10 shows the results of simulation indicating the development of the concentration profile in time for acetone at 25 °C, 1 bar. The 3D images of the cross section planes along the IRE are shown in **Figure 10 a**. Corresponding 2D images of the cross section plane located at the half length of the cell are shown in **Figure 10 b**. In both figures variations in concentrations are marked by changing color traces. From the figures it is to be noted that there is a delay in the buildup of acetone after the switch has been made from water to 2.5 wt. % acetone in water. Even after 90 s, the concentration of acetone has not reached its maximum value even in the zones close to the inlet. Simulations were also carried out for acetone in water at 100 °C, 20 bar and 230 °C, 30 bar.

In order to compare results of simulations at three temperatures, mean surface concentrations are plotted against time in **Figure 11**. There are no differences observed as can be expected from the relatively minor changes in the dynamic viscosity of water and diffusion coefficient of acetone (see **Table 4**). Using the cell volume (1,97 mL) and flow rate (2 mL/min) time required to fill the cell in a typical ATR-IR experiment was calculated to be about 59 s. The simulations show that it takes ~200 s to fill the cell with acetone solution and reach the maximum concentration of 2.5 wt. % acetone. This also includes the time for filling the additional volume of the inlet tube (~20 s, as can be seen from the delay time in concentration increase, **Figure 11**). Thus, the type of flow in the ATR-IR cell is different from ideal plug-flow. This has to be considered when ATR-IR experiments are carried out under steady state or transient conditions. ATR-IR experiments reported were carried out typically for 3600 s from the moment of the switch from water to reactant feed.

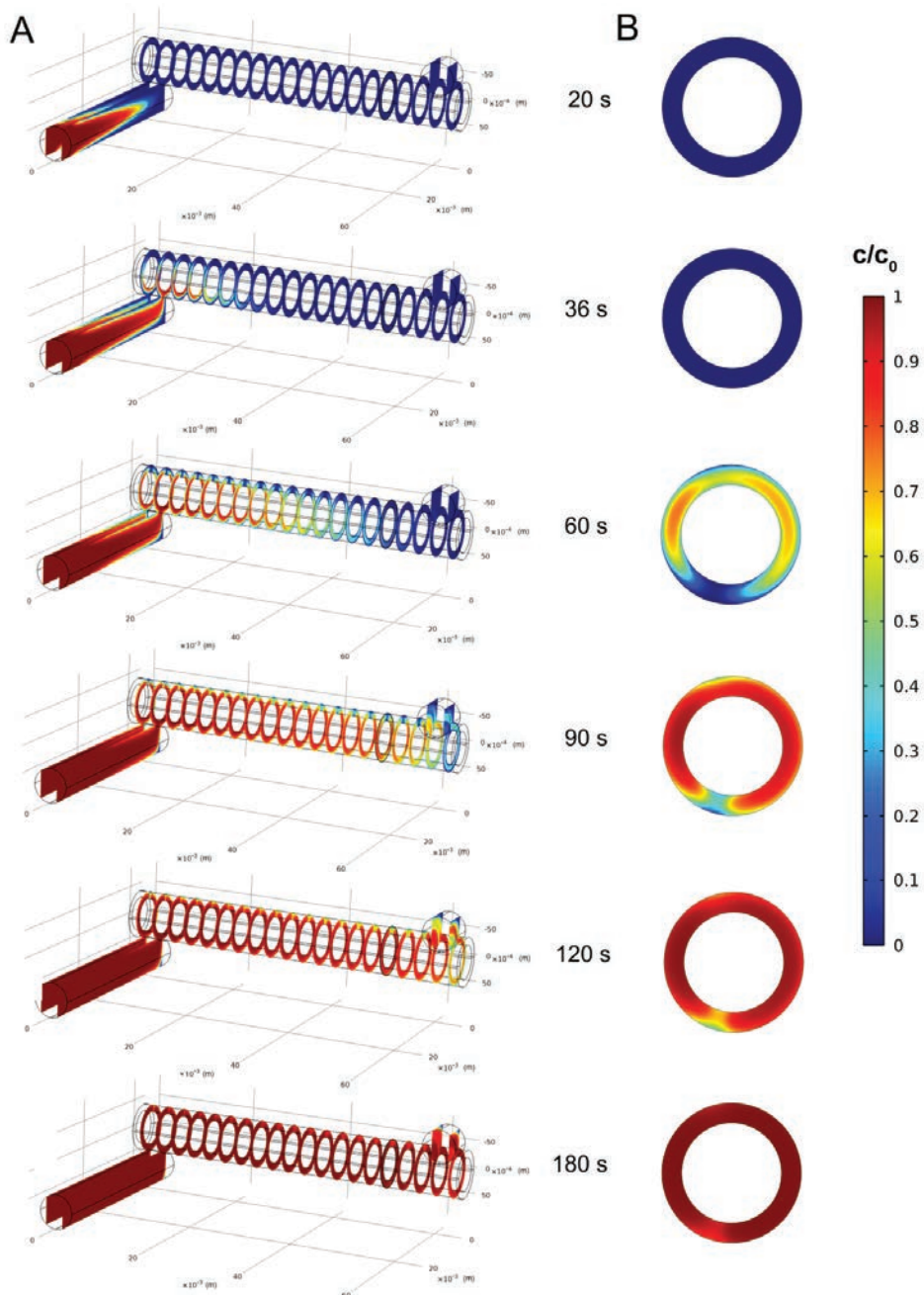


Figure 10. (A) 3D and (B) 2D color traces of acetone relative concentration at 20, 36, 60, 90, 120 and 180 s after switching the flow from water to 2.5 % wt. acetone solution at 25 °C/1 bar. 2D images represent the cross section from the mid-length of the cell. Flow rate of the liquid 2 mL/min. Initial acetone concentration is 25 g/L. Dark blue: $c/c_0 = 0$, dark red: $c/c_0 = 1$.

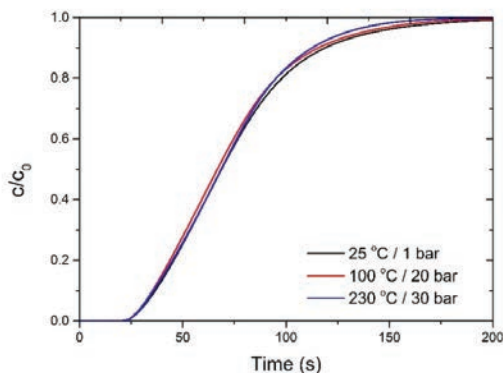


Figure 11. Mean surface concentrations of 2.5 wt. % acetone at 25 °C/1 bar, 100 °C/20 bar and 230 °C/30 bar. Time zero is defined as the time when the flow was switched from pure water to 2.5 wt. % acetone solution.

Figure 12 shows the changes in mean surface concentration as a function of time obtained by simulation for two different solutions, viz. 2.5 wt. % acetone or 9.2 wt. % glycerol solutions in water at 25 °C, 1 bar. Again, the concentration profiles are very similar which can be expected from the similar diffusion coefficients for glycerol and acetone (**Table 4**).

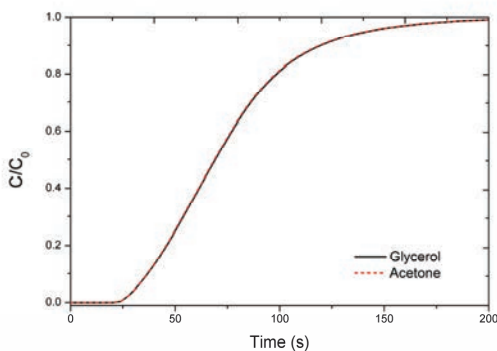


Figure 12. Mean surface concentrations of 2.5 wt. % acetone solution and 9.2 wt. % glycerol solution at 25 °C after the switch from water.

Further, simulations were also carried out to compare mean surface concentration with “concentrations at the outlet” of the ATR-IR cell. **Figure 13** shows that variation of mean surface concentration and the outlet concentration as a function of time. From the figure it can be seen that the mean surface concentration is higher than outlet concentration at initial times and ~200 s are required to get similar values. ATR-IR experiments reported were carried out at much longer time scales, up to 3600 s, *i.e.* at steady state conditions according to simulations. Transient experiments can take into

account the development of concentration with shorter times (e.g., < 100 s) as obtained from the simulations reported here.

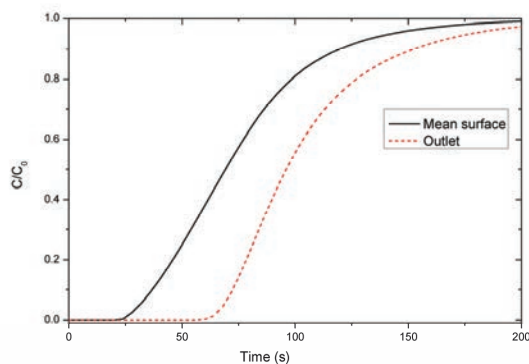


Figure 13. Mean surface concentration of glycerol against the concentration at the outlet for glycerol at 25 °C, 1 bar.

The transport phenomena in ATR-IR cells have also been reported in literature using experimental methods. Urakawa *et al.* [27] used colored and transparent solutions to correlate concentration changes with time. They found that for a flow-through, flat cell with a volume of 0.077 mL and the flow rate of 1.9 mL/min, it would take ~3 s to achieve steady state at 25 °C. They also reported that a compound with higher diffusion coefficient (acetonitrile) filled the reactor faster compared to a compound with lower diffusion coefficient (hemoglobin). From this they suggested that a convection-diffusion model describes this behavior better than a diffusion layer model. To recall, our simulations are based on a convection-diffusion model.

Aguirre *et al.* [28] also studied the hydrodynamics in an ATR-IR flow cell with flat ZnSe crystal using a switch between two immiscible liquids (carbon tetrachloride and water) and two miscible liquids (triton-X-100 and isopropyl alcohol). They concluded that the time needed to exchange was faster for miscible solutions. In this study ATR-IR experiments are carried out using a single liquid phase exclusively.

So far, flow and concentration patterns in the ATR-IR cell without a catalyst have been discussed. Incorporation of a porous catalyst layer will cause additional effects. For example, the porous catalyst layer may cause internal diffusion resistances which would affect concentrations across the catalyst layer in axial direction. In the current study the catalyst layers used are extremely thin as described before; therefore it is reasonable to assume that internal diffusion in the catalyst layer is not limiting. Thorough description of the catalyst layer including porosity, tortuosity *etc.*, are essential to carry out simulations and this is beyond the scope of the current study.

3.3 Experimental validation of ATR-IR cell with ZnSe IRE with and without catalyst layer

Experimental feasibility of the designed *in situ* ATR-IR cell was tested at 25 °C, 1 bar and at conditions typical for aqueous phase reforming reaction (200 °C, 20bar), both in the absence and in the presence of the catalyst. In the following section examples of spectra collected with and without catalyst are reported.

3.3.1 *In situ* ATR-IR spectra of water at elevated temperatures

Typical ATR-IR spectra recorded at higher temperatures and pressures (up to 225 °C, 40 bar) are shown in **Figure 14 a** in the presence of water only. The IR light throughput was 30% when the cell was operated at 225 °C, 40 bar in water flow, which is similar to the observations in literature [43]. Good quality spectra were obtained.

ATR-IR spectra of water at elevated temperatures and pressures contain not only peaks of water hydroxyl stretching and deformation vibrations (3200 – 3600 and 1640 cm^{-1} , respectively), but also complex bands between 1250 and 1000 cm^{-1} derived from the IRE (**Figure 14 a**).

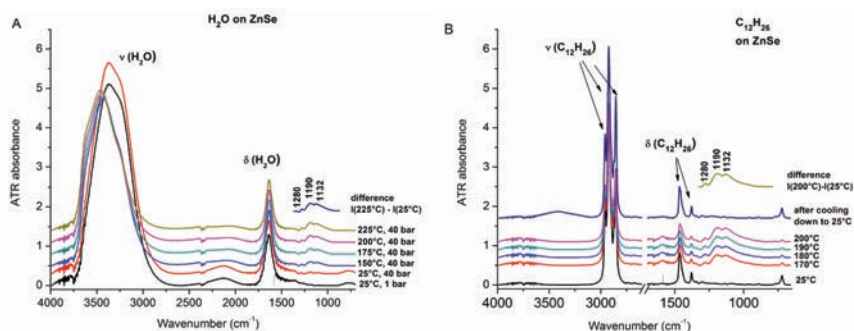


Figure 14. (a) *In situ* ATR-IR spectra of H_2O on bare ZnSe at 25 °C, 40 bar and at every 25 °C between 150 and 225 °C, 40 bar; (b) *In situ* ATR-IR spectra of *n*-dodecane ($n\text{-C}_{12}\text{H}_{26}$) on bare ZnSe at 25 °C, 1 bar and at every 10 °C between 170 and 200 °C, 1 bar.

This complex signal increases with temperature and disappears completely when the IRE is cooled down to room temperature after the experiment. The appearance of this signal can be related to the presence of either water, catalyst or the ZnSe crystal. It was shown in literature that phonon vibrational modes of ZnSe usually appear at frequencies well below 1000 cm^{-1} [50]. Thus, phonon vibrations cannot be responsible for the appearance of this complex signal. Moreover, the same phenomenon was observed when the IRE was heated to similar temperatures in *n*-dodecane (**Figure 14 b**). *N*-dodecane has a high boiling point (214 °C), thus no pressure is needed to keep it in liquid state, unlike water. Similarity of the “difference spectra” in **Figure 14 a, b** allows to conclude that these complex bands are not related to vibrational bands of the liquid covering the IRE. We attribute these bands to an effect of temperature on ZnSe, since

temperature generally affects the refractive index of the optical material [51], which can cause distortions in total reflection phenomenon. Interestingly, the influence of these bands on the spectra of adsorbates collected during catalytic experiment can be minimized by subtracting the spectrum of water collected at the temperature of the experiment.

3.3.2 *In situ* ATR-IR spectra of glycerol solutions at elevated temperatures without catalyst

Figure 15 shows the experimental spectra of 9.2 wt. % glycerol at 25 °C/1bar and at 230 °C/30 bar in the absence of the catalyst at flow rates of 1.9 mL/min and 2 mL/min, respectively. Spectra have three main regions with peaks assigned to glycerol (i) C-H stretching (3000 - 2800 cm^{-1}), (ii) C-H deformation (1500 - 1150 cm^{-1}) and (iii) C-OH stretching (1150 - 950 cm^{-1}). Negative peaks at around 1650 cm^{-1} are the residual peaks after subtraction of spectrum of water and peaks at around 2350 cm^{-1} are assigned to atmospheric carbon dioxide. From the spectra it is clear that intensities of glycerol peaks increased gradually as the concentration of glycerol in the cell increased.

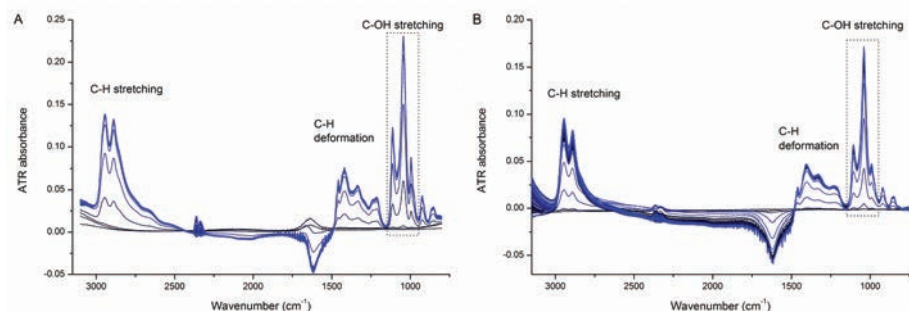


Figure 15. Water subtracted *in situ* ATR-IR spectra of 9.2 wt.% glycerol solution in water over bare IRE at (a) 25 °C/1 bar (1.9 mL/min), (b) 230 °C/30bar (2 mL/min). Time difference between each spectrum is 0.5 min.

To compare the transient intensity increase observed in the ATR-IR experiments with the simulations, the IR intensities between 1150 and 950 cm^{-1} were integrated, then normalized to the maximum value and plotted against time (**Figure 16**). At 25 °C and 230 °C, the IR intensity reached its maximum intensity after 240 s and 480 s, respectively. The baseline fluctuations at 230 °C cause delays in the stabilization of the signal compared to 25 °C. Indicated times in the figure exclude initial delays needed to fill the pre-heater tube volume.

Experimental residence times are in good agreement with simulations. The concentration stabilized after 180 s and 420 s at 2 mL/min, according to both simulations and experiments, respectively.

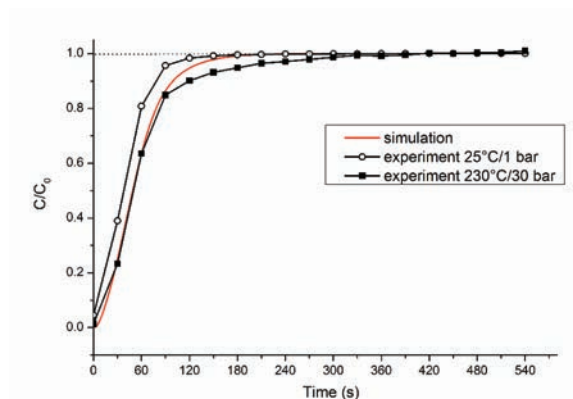


Figure 16. Comparison between simulated mean surface concentrations for glycerol at 25 °C, 1 bar at 2 mL/min (solid line) and experimental normalized peak areas (1150 - 950 cm^{-1}) during glycerol introduction into ATR-IR cell filled with water at 25 °C/1bar (open circles, flow rate 1.9 mL/min) and 230 °C/30bar (black squares, flow rate 2 mL/min).

3.3.3 *In situ* ATR-IR spectra of hydroxyacetone at RT and at elevated temperatures with catalyst

Further, experiments were carried out in the ATR-IR cell in the presence of the catalyst layer. APR of 2.5 wt. % hydroxyacetone solution on Pt/ZrO₂ catalyst was studied at 230 °C/ 30bar. In **Figure 17** *in situ* ATR-IR spectra of hydroxyacetone at 25 °C on the bare ZnSe are compared with those at higher temperature on Pt/ZrO₂. Peaks in the spectrum at 25 °C were assigned to main functional groups of hydroxyacetone (i) C=O stretching (1718 cm^{-1}), (ii) CH₃ deformations (1419 and 1363 cm^{-1}), (iii) C-O stretching (1083 cm^{-1}) according to the literature [52]. Spectra at 230 °C also show peaks assigned to hydroxyacetone, however, additional peaks at 1691, 1544 and 1118 cm^{-1} were observed when catalyst was present.

These peaks correspond to adsorbed species on the surface of the catalyst. We have proposed that these adsorbates arise from aldol condensation of hydroxyacetone that typically happens with aldehydes and ketones, especially in the presence of metal oxides such as zirconia. More details of the condensation and peak assignments can be found in **Chapter 5**.

The results presented above allow us to conclude that ATR-IR spectroscopy can be used to study adsorbates during the reaction at elevated temperatures and pressures. Thus, we have validated the performance of the *in situ* cell for use at higher temperatures and pressures in aqueous phase catalyzed reactions for *e.g.*, APR.

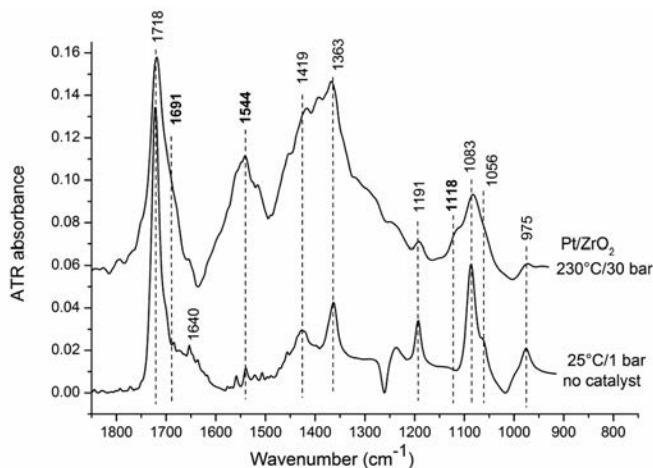


Figure 17. ATR-IR spectra of hydroxyacetone at 25 °C, 1 bar on a bare IRE and at 230 °C/30 bar on a Pt/ZrO₂ catalyst.

4. Conclusions

Design of an *in situ* ATR-IR Tunnel cell with cylindrical IRE coated with mechanically stable catalyst layer is suitable for experiments at high temperatures and pressures. Hydrodynamic flow simulations showed deviation from plug flow behavior in the cell. This allows to follow concentration with time both in transient and steady state regimes. Residence time distributions obtained from simulations were compared to the experimental results obtained with acetone and glycerol solutions, showing good agreement. Results, obtained during aqueous phase reforming of hydroxyacetone in the presence of a Pt/ZrO₂ catalyst layer, suggested formation of adsorbates on the surface of the catalyst, which were assigned to aldol condensation products of hydroxyacetone, demonstrating the ability of the designed cell to perform *in situ* ATR-IR studies at temperatures up to 230 °C and pressures up to 30 bar.

5. Acknowledgements

This research has been performed within the framework of the CatchBio program (project number 053.70.002). The authors gratefully acknowledge the support of the Smart Mix Program of the Netherlands Ministry of Economic Affairs and the Netherlands Ministry of Education, Culture and Science. Mark Smithers is acknowledged for collecting SEM images of the coated layers.

6. References

1. Andanson, J.M. and A. Baiker, *Exploring catalytic solid/liquid interfaces by in situ attenuated total reflection infrared spectroscopy*. Chem Soc Rev, 2010. **39**(12): p. 4571-84.
2. Foster, A.J. and R.F. Lobo, *Identifying reaction intermediates and catalytic active sites through in situ characterization techniques*. Chem Soc Rev, 2010. **39**(12): p. 4783-93.
3. Hind, A.R., S.K. Bhargava, and A. McKinnon, *At the solid/liquid interface: FTIR/ATR - the tool of choice*. Advances in Colloid and Interface Science, 2001. **93**(1-3): p. 91-114.
4. Davda, R.R., J.W. Shabaker, G.W. Huber, R.D. Cortright, and J.A. Dumesic, *A review of catalytic issues and process conditions for renewable hydrogen and alkanes by aqueous-phase reforming of oxygenated hydrocarbons over supported metal catalysts*. Applied Catalysis B-Environmental, 2005. **56**(1-2): p. 171-186.
5. Koichumanova, K., A.K.K. Vikla, D.J.M. de Vlieger, K. Seshan, B.L. Mojet, and L. Lefferts, *Towards Stable Catalysts for Aqueous Phase Conversion of Ethylene Glycol for Renewable Hydrogen*. Chemsuschem, 2013. **6**(9): p. 1717-1723.
6. Cortright, R.D., R.R. Davda, and J.A. Dumesic, *Hydrogen from catalytic reforming of biomass-derived hydrocarbons in liquid water*. Nature, 2002. **418**(6901): p. 964-967.
7. Shi, H., J.A. Lercher, and X.Y. Yu, *Sailing into uncharted waters: Recent advances in the in situ monitoring of catalytic processes in aqueous environments*. Catalysis Science and Technology, 2015. **5**(6): p. 3035-3060.
8. Brown, M.A., I. Jordan, A. Belouqui Redondo, A. Kleibert, H.J. Wörner, and J.A. Van Bokhoven, *In situ photoelectron spectroscopy at the liquid/nanoparticle interface*. Surface Science, 2013. **610**: p. 1-6.
9. Brown, M.A., A.B. Redondo, I. Jordan, N. Duyckaerts, M.T. Lee, M. Ammann, F. Nolting, A. Kleibert, T. Huthwelker, J.P. Mächler, M. Birrer, J. Honegger, R. Wetter, H.J. Wörner, and J.A. Van Bokhoven, *A new endstation at the Swiss Light Source for ultraviolet photoelectron spectroscopy, X-ray photoelectron spectroscopy, and X-ray absorption spectroscopy measurements of liquid solutions*. Review of Scientific Instruments, 2013. **84**(7).
10. Grunwaldt, J.D. and A. Baiker, *In situ spectroscopic investigation of heterogeneous catalysts and reaction media at high pressure*. Physical Chemistry Chemical Physics, 2005. **7**(20): p. 3526-3539.
11. Meunier, F.C., *The design and testing of kinetically-appropriate operando spectroscopic cells for investigating heterogeneous catalytic reactions*. Chemical Society Reviews, 2010. **39**(12): p. 4602-4614.
12. Rehan, M., X. Lai, and G.M. Kale, *Hydrothermal synthesis of titanium dioxide nanoparticles studied employing in situ energy dispersive X-ray diffraction*. CrystEngComm, 2011. **13**(11): p. 3725-3732.
13. Jensen, H., M. Bremholm, R.P. Nielsen, K.D. Joensen, J.S. Pedersen, H. Birkedal, Y.S. Chen, J. Almer, E.G. Søggaard, S.B. Iversen, and B.B. Iversen, *In situ high-energy synchrotron radiation study of sol-gel nanoparticle formation in supercritical fluids*. Angewandte Chemie - International Edition, 2007. **46**(7): p. 1113-1116.
14. Buurmans, I.L.C. and B.M. Weckhuysen, *Heterogeneities of individual catalyst particles in space and time as monitored by spectroscopy*. Nature Chemistry, 2012. **4**(11): p. 873-886.

15. Ashbrook, S.E., D.M. Dawson, and V.R. Seymour, *Recent developments in solid-state NMR spectroscopy of crystalline microporous materials*. Physical Chemistry Chemical Physics, 2014. **16**(18): p. 8223-8242.
16. Zhang, W., S. Xu, X. Han, and X. Bao, *In situ solid-state NMR for heterogeneous catalysis: a joint experimental and theoretical approach*. Chemical Society Reviews, 2012. **41**(1): p. 192-210.
17. Tinnemans, S.J., J.G. Mesu, K. Kervinen, T. Visser, T.A. Nijhuis, A.M. Beale, D.E. Keller, A.M.J. Van Der Eerden, and B.M. Weckhuysen, *Combining operando techniques in one spectroscopic-reaction cell: New opportunities for elucidating the active site and related reaction mechanism in catalysis*. Catalysis Today, 2006. **113**(1-2): p. 3-15.
18. Mul, G., G.M. Hamminga, and J.A. Moulijn, *Operando ATR-FTIR analysis of liquid-phase catalytic reactions: can heterogeneous catalysts be observed?* Vibrational Spectroscopy, 2004. **34**(1): p. 109-121.
19. Bürgi, T. and A. Baiker, *Attenuated Total Reflection Infrared Spectroscopy of Solid Catalysts Functioning in the Presence of Liquid-Phase Reactants*, in *Advances in Catalysis*, C.G. Bruce and K. Helmut, Editors. 2006, Academic Press. p. 227-283.
20. Armaroli, T., T. Bécue, and S. Gautier, *Spectroscopie infrarouge en réflexion diffuse (DRIFTS) : application à l'analyse in situ de catalyseurs*. Oil & Gas Science and Technology - Rev. IFP, 2004. **59**(2): p. 215-237.
21. Mojet, B.L., S.D. Ebbesen, and L. Lefferts, *Light at the interface: the potential of attenuated total reflection infrared spectroscopy for understanding heterogeneous catalysis in water*. Chem Soc Rev, 2010. **39**(12): p. 4643-55.
22. Harrick, N.J., *Internal Reflection Spectroscopy*. 1967, New York: Interscience Publishers.
23. Fahrenfort, J., *Attenuated total reflection. A new principle for the production of useful infra-red reflection spectra of organic compounds*. Spectrochimica Acta, 1961. **17**(7): p. 698-709.
24. Dobson, K.D. and A.J. McQuillan, *In situ infrared spectroscopic analysis of the adsorption of aliphatic carboxylic acids to TiO₂, ZrO₂, Al₂O₃, and Ta₂O₅ from aqueous solutions*. Spectrochimica Acta - Part A: Molecular and Biomolecular Spectroscopy, 1999. **55**(7-8): p. 1395-1405.
25. Meemken, F., P. Müller, K. Hungerbühler, and A. Baiker, *Simultaneous probing of bulk liquid phase and catalytic gas-liquid-solid interface under working conditions using attenuated total reflection infrared spectroscopy*. Review of Scientific Instruments, 2014. **85**(8).
26. Copeland, J.R., G.S. Foo, L.A. Harrison, and C. Sievers, *In situ ATR-IR study on aqueous phase reforming reactions of glycerol over a Pt/ γ -Al₂O₃ catalyst*. Catalysis Today, 2013. **205**(0): p. 49-59.
27. Urakawa, A., R. Wirz, T. Bürgi, and A. Baiker, *ATR-IR Flow-Through Cell for Concentration Modulation Excitation Spectroscopy: Diffusion Experiments and Simulations*. Journal of Physical Chemistry B, 2003. **107**(47): p. 13061-13068.
28. Aguirre, A., P.A. Kler, C.L.A. Berli, and S.E. Collins, *Design and operational limits of an ATR-FTIR spectroscopic microreactor for investigating reactions at liquid–solid interface*. Chemical Engineering Journal, 2014. **243**(0): p. 197-206.
29. Poston, P.E., D. Rivera, R. Uibel, and J.M. Harris, *In situ detection of adsorbates at silica/solution interfaces by fourier transform infrared attenuated total reflection*

- spectroscopy using a silica-coated internal reflection element*. Applied Spectroscopy, 1998. **52**(11): p. 1391-1398.
30. Koichumanova, K., K.B. Sai Sankar Gupta, L. Lefferts, B.L. Mojet, and K. Seshan, *In situ ATR-IR spectroscopy study of aluminas under aqueous phase reforming conditions*. Physical Chemistry Chemical Physics, 2015.
 31. Guzman, M., J. Ruzicka, G.D. Christian, and P. Shelley, *Enhancement of Fourier transform infrared spectrometry by the flow-injection technique: Transmittance and internal total reflectance cell in a single-line system*. Vibrational Spectroscopy, 1991. **2**(1): p. 1-14.
 32. Zakzeski, J., R.J.H. Grisel, A.T. Smit, and B.M. Weckhuysen, *Solid acid-catalyzed cellulose hydrolysis monitored by in situ Atr-Ir spectroscopy*. ChemSusChem, 2012. **5**(2): p. 430-437.
 33. Zakzeski, J., P.C.A. Bruijninx, and B.M. Weckhuysen, *In situ spectroscopic investigation of the cobalt-catalyzed oxidation of lignin model compounds in ionic liquids*. Green Chemistry, 2011. **13**(3): p. 671-680.
 34. Tejedor-Tejedor, M.I. and M.A. Anderson, "In situ" attenuated total reflection fourier transform infrared studies of the goethite (α -FeOOH)-aqueous solution interface. Langmuir, 1986. **2**(2): p. 203-210.
 35. Doyle, W.M., *Absorbance linearity and repeatability in cylindrical internal reflectance FT-IR spectroscopy of liquids*. Applied Spectroscopy, 1990. **44**(1): p. 50-59.
 36. www.harricksci.com. UV-Vis-IR Optical materials.
 37. <http://refractiveindex.info/>, Refractive index database.
 38. Ebbesen, S.D., B.L. Mojet, and L. Lefferts, *In situ ATR-IR study of CO adsorption and oxidation over Pt/Al₂O₃ in gas and aqueous phase: Promotion effects by water and pH*. Journal of Catalysis, 2007. **246**(1): p. 66-73.
 39. Ebbesen, S.D., B.L. Mojet, and L. Lefferts, *In situ ATR-IR study of nitrite hydrogenation over Pd/Al₂O₃*. Journal of Catalysis, 2008. **256**(1): p. 15-23.
 40. Mondelli, C., J.D. Grunwaldt, D. Ferri, and A. Baiker, *Role of Bi promotion and solvent in platinum-catalyzed alcohol oxidation probed by in situ X-ray absorption and ATR-IR spectroscopy*. Physical Chemistry Chemical Physics, 2010. **12**(20): p. 5307-5316.
 41. Mondelli, C., D. Ferri, J.D. Grunwaldt, F. Krumeich, S. Mangold, R. Psaro, and A. Baiker, *Combined liquid-phase ATR-IR and XAS study of the Bi-promotion in the aerobic oxidation of benzyl alcohol over Pd/Al₂O₃*. Journal of Catalysis, 2007. **252**(1): p. 77-87.
 42. Ferri, D., T. Biirgi, and A. Baiker, *Pt and Pt/Al₂O₃ thin films for investigation of catalytic solid-liquid interfaces by ATR-IR spectroscopy: CO adsorption, ha-induced reconstruction and surface-enhanced absorption*. Journal of Physical Chemistry B, 2001. **105**(16): p. 3187-3195.
 43. Bremer, P.J. and G. Geesey, *Determination of the feasibility of using attenuated total reflectance Fourier transform-infrared spectroscopy to evaluate thermal ageing of enamel-coated magnet wire*. Journal of Materials Science, 1997. **32**(1): p. 141-146.
 44. Puetz, J. and M.A. Aegerter, *Dip Coating Technique*, in *Sol-Gel Technologies for Glass Producers and Users*, M. Aegerter and M. Mennig, Editors. 2004, Springer US. p. 37-48.
 45. *Handbook of Optical Constants of Solids*, ed. E.D. Palik. 1985, Boston: Academic Press.

46. *Handbook of Chemistry and Physics*, ed. D.R. Lide. 1999-2000: CRC Press.
47. *Handbook of Optics, 3rd Ed., Vol. 4*. 2009, McGraw-Hill.
48. <http://www.spectra.com/sopra.html>. SOPRA N&K Database.
49. *Handbook of Optical Materials*, ed. M.J. Weber. 2003: CRC Press.
50. Mitra, S.S., *Phonon assignments in ZnSe and GaSb and some regularities in the phonon frequencies of zincblende-type semiconductors*. *Physical Review*, 1963. **132**(3): p. 986-991.
51. Tsay, Y.F., B. Bendow, and S.S. Mitra, *Theory of the temperature derivative of the refractive index in transparent crystals*. *Physical Review B*, 1973. **8**(6): p. 2688-2696.
52. Mohaček-Grošev, V., *Vibrational analysis of hydroxyacetone*. *Spectrochimica Acta Part A: Molecular and Biomolecular Spectroscopy*, 2005. **61**(3): p. 477-484.

Chapter 3

Towards stable catalysts for the aqueous phase conversion of ethylene glycol for renewable hydrogen

Aqueous phase reforming of ethylene glycol over alumina supported Pt based catalysts is reported. Performance of the catalysts was investigated using kinetics and *in situ* ATR-IR spectroscopy. Pt/ γ -Al₂O₃ is unstable under APR conditions, 270 °C/90 bar, and undergoes a phase transformation to boehmite (AlO(OH)). This conversion of alumina was studied *in situ* with ATR-IR spectroscopy and transition into boehmite even proceeds at milder conditions (210 °C/40 bar). Pt/ γ -Al₂O₃ deactivates irreversibly because the Pt surface area decreases owing to an increasing metal particle size and coverage with boehmite. However, Pt supported on boehmite itself shows stable activity. Surprisingly, the rate of formation of hydrogen per Pt surface atom is significantly higher on boehmite as compared to alumina supported catalyst. This observation seems correlated to both increased concentration of surface OH groups as well as to enhanced oxidation of Pt, when comparing Pt/ γ -Al₂O₃ to Pt/AlO(OH).

This chapter has been published as

K. Koichumanova, A. K. K. Vikla, D. J. M. de Vlieger, K. Seshan, B. L. Mojet, L. Lefferts
Towards Stable Catalysts for Aqueous Phase Conversion of Ethylene Glycol for Renewable Hydrogen, ChemSusChem **2013**, 6, 1717 – 1723

1. Introduction

Environmental concerns and energy shortage have driven modern society to search for alternative, sustainable energy sources to replace fossil fuels. Waste biomass streams are renewable feed stocks for the valorization to fuels [1, 2]. In the case of hydrogen or syngas as the targeted fuel or fuel precursor, respectively, steam reforming (SR) is the preferred route [1-4]. SR is usually performed at high temperatures (>750 °C) as the reaction is strongly endothermic and requires activation of water.

Biobased feed stocks consist typically of organic components dissolved in water. For example, aqueous phase of pyrolysis oil contains up to 20 wt. % of oxygenated components [2]. The primary difficulty in gasification via steam reforming of such feedstocks is the energy efficiency of the conversion due to the necessity of vaporizing high amounts of water. Dumesic and co-workers [1] introduced Aqueous Phase Reforming (APR) for production of hydrogen rich gas from dilute aqueous oxygenated feed stocks. In APR water is kept in a liquid state by applying pressure at moderate temperatures (*e.g.* T = 225 - 450 °C, p = 29 - 250 bar) [1, 5]. Thermodynamics favor formation of hydrogen under these conditions [6], however formation of alkanes *e.g.*, methane, in parallel, lowers hydrogen selectivity. Studies with model oxygenate components typically found in biomass waste streams [1, 7], show that dehydration of the oxygenate leads to hydrocarbon formation. Formation of hydrogen requires, however, break down of the carbon chain to C₁, which undergoes oxidation via water to form CO₂ and hydrogen.

Thus, to achieve a high hydrogen yield, catalysts for APR should be active in C-C bond scission and in the water gas reaction (WGS) ($\text{CO} + \text{H}_2\text{O} \rightarrow \text{CO}_2 + \text{H}_2$). Pt based catalysts are often used as they are active for the C-C cleavage and at the same time efficient for SR/WGS reactions [8-11]. In the mechanistic sequence, activation of water is usually achieved through formation of hydroxyl groups on oxide supports. Hydroxyl groups then react with the "C" residue on the Pt metal to complete the SR/WGS reactions [2-4]. Therefore, the catalyst support plays a crucial role and catalysts are thus bifunctional. This bifunctional mechanism requires active metal sites, such as Pt, to be situated in close proximity to the OH-groups of the support [3].

Catalyst stability during APR is a challenging issue. Especially in the case of bio-based feedstocks, coke and char formation causes severe problems for both catalysts and reactors. Additionally, harsh hydrothermal conditions during APR shorten the lifetime of the catalyst as result of leaching, sintering of metals and/or the support [5, 12].

In general, development of efficient catalysts requires a thorough understanding of the reaction sequences that take place on the catalyst surface, this can often be achieved through *in situ* studies. FTIR spectroscopy is a tool for such studies, in particular Attenuated Total Reflection Infrared (ATR-IR) Spectroscopy allows such studies to be

performed in the liquid phase [13, 14]. However, it is challenging to use this technique at typical reaction conditions for APR [15, 16].

Pt/ γ -Al₂O₃ has been reported as a promising catalyst for the APR conversion of bio-wastes to hydrogen [1, 5, 12]. It was shown earlier by *ex situ* studies [7, 17] that γ -Al₂O₃ undergoes phase change to boehmite (aluminium oxo-hydroxide (AlO(OH))), when exposed to hot compressed water. Boehmite is the thermodynamically stable form of alumina in aqueous environment at temperatures higher than 150 °C [18], including typical APR conditions. This phase transformation results in a decreased surface area [5, 19], and can have detrimental effects on the catalyst performance due to facilitating growth of metal particles [5] and possible blockage of the metal surface by a newly formed layer of boehmite [7].

In this study, activity and stability of Pt/ γ -Al₂O₃ catalyst for APR of ethylene glycol (EG) is investigated. The conversion of γ -Al₂O₃ to boehmite is studied with *in situ* ATR-IR spectroscopy in hot compressed water. This phase transformation is accompanied by catalyst deactivation. However, using boehmite as catalyst support results in a catalyst with phase stability and remarkably stable activity with high H₂ yield. This is probably due to the high concentration of surface-OH-groups [20], which can be beneficial for both SR and WGS reactions since OH-groups are essential for water activation.

2. Experimental Section

2.1 Catalyst preparation

Pt/ γ -Al₂O₃ and Pt/AlO(OH) catalysts were prepared through wet impregnation of the γ -Al₂O₃ support (BASF AL-3992) and AlO(OH) supports, respectively. The supports were crushed and sieved to a particle size of 300 – 600 μ m. AlO(OH) was prepared by subjecting γ -Al₂O₃ to a heat treatment in the presence of water (270 °C, 90 bar, 45 min). H₂PtCl₆·6H₂O (Alfa Aesar) was used as platinum precursor. The alumina support was added to the solution of the precursor in water (weight ratio H₂O/alumina = 1.8) and the water was removed under vacuum at 100 °C. Catalysts were subjected to a H₂ treatment (H₂ 100 mL/min, N₂ 100 mL/min, 5 h, 100 °C) to minimize the amount of chlorine remaining from the Pt precursor. Finally, the Pt/ γ -Al₂O₃ catalyst was calcined at 500 °C and the Pt/AlO(OH) catalyst was calcined at 350 °C for 15 h under air flow (200 mL/min).

2.2 Catalyst characterization

Platinum loadings on catalysts were measured by means of X-ray fluorescence (XRF) (Philips, PW 1480). The surface areas of the catalysts were analyzed by applying the BET-method (Micromeritics, ASAP 2400). TEM imaging (Philips CM300ST-FEG 300 kV microscope equipped with energy-dispersive X-ray spectroscopy) was performed to

obtain information about the Pt particle size on the supports by calculating the weighted average of about 100 particles. The Pt dispersion for the fresh Pt/ γ -Al₂O₃ was also measured by using CO pulse chemisorption (Micromeritics Chemisorb 2750). Before CO chemisorption the catalyst was reduced in H₂ at 200 °C for 1 h. XRD patterns were collected for the boehmite support as well as for the fresh and spent catalysts to determine the phase of the support between $2\theta=10-70^\circ$ by using a Bruker 2D Powder diffractometer equipped with a Cu K α 1 radiation source.

2.3 Kinetic experiments

APR experiments were performed in a continuous flow fixed bed reactor using 5 wt. % EG (Sigma-Aldrich) in water as a feed. The scheme of the setup was presented elsewhere [5]. Typical reaction conditions were 270 °C, 90 bar and a catalyst loading of 1 g. The liquid feed (2 mL/min) was pumped through a preheater to the stainless steel reactor by using HPLC pump. Gases and liquids were separated and the composition of the gas products was analyzed with micro-gas-chromatography (GC, Varian CP4900) equipped with a MS5 and PPQ columns. The carbon content in the liquid feed was analyzed by using a total-organic-carbon analyzer (TOC-VCSH Analyser), and the composition of the liquid products was analyzed by performing HPLC (RID-10A detector, Aminex HPX-87H column, 300×7.8 mm) in 0.005M H₂SO₄ effluent, (flow of 0.6 mL/min). The H₂ selectivity was calculated based on the amount of converted EG to carbon-containing compound in the gaseous product stream, defining 100% selectivity as complete conversion of EG to exclusively CO₂ and H₂ (**Equation 1**). The selectivity to carbon-containing gaseous products was calculated according to **Equation 2**, where a maximal reforming ratio (RR) [1, 7] for EG into H₂/CO₂ is 5/2. The calculation of the carbon to gas conversion was achieved by using **Equation 3**.

$$\%H_2 \text{ selectivity} = \frac{H_2 \text{ moles produced}}{C \text{ atoms in gas phase}} \cdot \frac{1}{RR} \cdot 100 \quad (\text{Eq.1})$$

$$\% \text{ Selectivity of } i = \frac{C \text{ atoms in species } i}{C \text{ atoms in gas phase}} \cdot \frac{1}{RR} \cdot 100 \quad (\text{Eq.2})$$

in which species $i = CO, CO_2, CH_4, C_{2+}$

$$\% \text{ Carbon to gas conversion} = \frac{C \text{ atoms in gas phase}}{\text{total } C \text{ atoms in feedstock}} * 100 \quad (\text{Eq.3})$$

The hydrogen formation rate was calculated based on the initial H₂ production rates (mol/s) per Pt surface atom. The number of Pt surface atoms was calculated from TEM images, assuming hemispherical particles.

2.4 ATR-IR experiments

ATR-IR spectra were collected by using FTIR spectrometer (Bruker, Tensor 27) equipped with liquid nitrogen cooled mercury-cadmium-telluride detector and an ATR-

IR Tunnel cell (Axiom) mounted in a sample chamber. Every spectrum was recorded with a 4 cm^{-1} resolution averaging 256 scans for a background spectra and 128 scans for liquid and gas phase spectra.

An internal reflection element (ZnSe rod, diameter 6.4 mm, length 70 mm) was spray-coated with catalyst and carefully placed inside the tunnel cell using O-rings (Kalrez 7075). The cell was connected to the inlet of the gas or liquid. Pretreatment of the catalyst layer was performed in He (20 mL/min) at $150\text{ }^{\circ}\text{C}$ to remove any solvent traces used during catalyst immobilization. The sample was oxidized in a 40 vol. % O_2/He mixture (50 mL/min) at the same temperature and cooled down to room temperature in a 50 vol. % H_2/He flow (50 mL/min). CO gas phase adsorption was performed at room temperature during 1 h in a 20 vol. % CO/He mixture (25 mL/min).

For liquid phase experiments, degassed water was pumped (1 mL/min) into the system by HPLC pump (Dionex P680) until 40 bar was reached and heated to APR temperatures ($150\text{--}210\text{ }^{\circ}\text{C}$). The catalyst was first heated to $150\text{ }^{\circ}\text{C}$, followed by further stepwise heating at $10\text{ }^{\circ}\text{C}$ steps, keeping the sample for 30 min at each step. Spectra were recorded at the end of each step.

3. Results and Discussion

$\text{Pt}/\gamma\text{-Al}_2\text{O}_3$ and $\text{Pt}/\text{AlO}(\text{OH})$ were prepared for the APR of EG by using the wet impregnation method. **Figure 1** shows typical TEM micrographs of the two catalysts as typical examples of the particle size distribution. The Pt particle size was estimated from a weighted average based on approximately 100 particles.

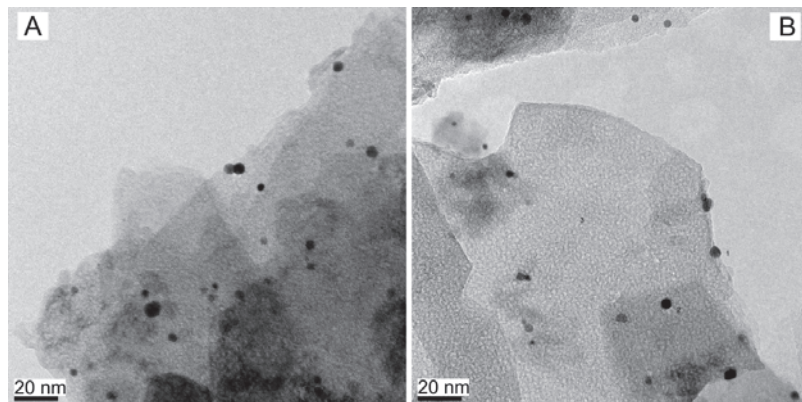


Figure 1. TEM images of used $\text{Pt}/\gamma\text{-Al}_2\text{O}_3$ (a) and fresh $\text{Pt}/\text{AlO}(\text{OH})$ (b).

Table 1 shows the characteristics of the catalysts. Fresh $\text{Pt}/\gamma\text{-Al}_2\text{O}_3$ has a surface area of $182\text{ m}^2/\text{g}$ and contains about 1.7 wt. % Pt with an average particle size 2.4 nm and a standard deviation of 1.3. The Pt particle size of 2.4 nm of this catalyst was confirmed by performing CO chemisorption experiments. This size corresponds to 43% dispersion.

Fresh Pt/AlO(OH) has a lower surface area (36 m²/g), and relatively larger Pt particles 5.7 nm.

Table 1. Catalyst characterization results

Catalyst	Pt loading, wt. %	BET surface area, m ² /g	Average Pt particle size, nm ^[a]
Pt/ γ -Al ₂ O ₃ fresh	1.7	182	2.4±1.3
Pt/ γ -Al ₂ O ₃ used (5 hours)	1.6	33	6.3±1.7
Pt/AlO(OH) fresh	1.4	36	5.7±1.2
Pt/AlO(OH) used (5 hours)	1.4	20	5.7±1.2

[a] weighted average and standard deviation based on ~ 100 particles from TEM micrographs.

Both catalysts were tested in APR with 5 wt. % of EG at 270 °C and 90 bar for 5 h. Details of the kinetics and ATR-IR measurements are provided in the experimental section. As shown in **Figure 2**, Pt/ γ -Al₂O₃ showed an appreciable loss of activity after 5 h (up to 20%), whereas Pt/AlO(OH) maintained a stable activity (the small increase in activity during the experiment is within the margin of experimental error).

To determine the reasons for the deactivation, spent Pt/ γ -Al₂O₃ catalyst was characterized after used. As indicated earlier, because the catalysis for APR is bifunctional, changes with respect to both Pt and γ -Al₂O₃ may be responsible for deactivation.

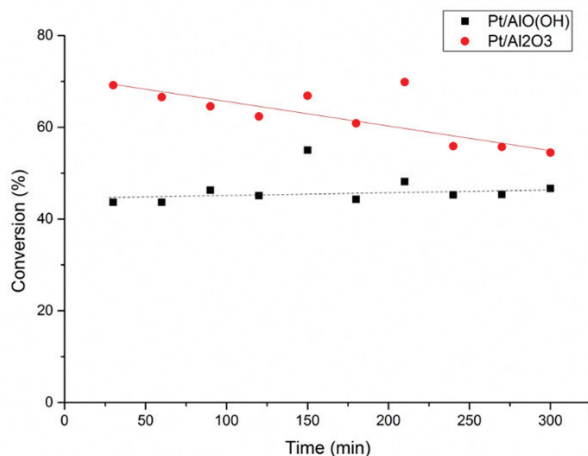


Figure 2. Conversion of 5 wt. % of ethylene glycol over Pt/ γ -Al₂O₃ and Pt/AlO(OH) catalysts at 270 °C and 90 bar; the purpose of the lines is to guide the eye.

Results shown in **Table 1** indicate that the Pt content in the catalysts did not change on use, indicating that no leaching and loss of Pt occurred during the reaction

under APR conditions. In the case of Pt/ γ -Al₂O₃, the average Pt particles sizes increased from 2.4 to 6.3 nm as determined from the TEM images, indicating sintering of the metal particles. For this catalyst, parallel to the loss of activity, also the support surface area was reduced drastically after usage at APR conditions (**Table 1**).

Figure 3 shows the XRD patterns for the catalysts. The XRD spectrum of fresh Pt/ γ -Al₂O₃ is characteristic for γ -Al₂O₃. The patterns of used Pt/ γ -Al₂O₃ and both fresh and used Pt/AlO(OH) resembles the structure of boehmite. Based on the fact that under hydrothermal conditions γ -Al₂O₃ undergoes a phase change to AlO(OH) [7, 17], it is not surprising that the surface area of Pt/ γ -Al₂O₃ reaches that of Pt/AlO(OH) (**Table 1**).

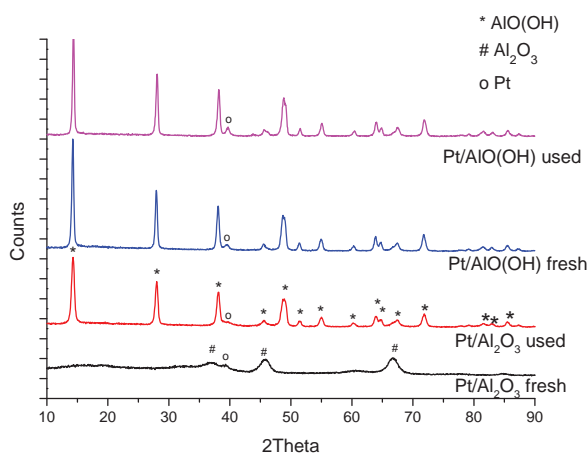


Figure 3. XRD patterns for the catalysts used in the study (* AlO(OH), # Al₂O₃, * Pt).

Moreover, AlO(OH) was prepared through hydrothermal treatment of γ -Al₂O₃ at conditions similar to APR reaction conditions (see the experimental section). Thus, during the APR experiment, γ -Al₂O₃ is unstable and susceptible to phase change, whereas boehmite is stable.

To study the details of the *in situ* transition of γ -Al₂O₃ into boehmite during APR, we have developed an *in situ* ATR-IR cell that enables catalyst studies under elevated temperature and pressure up to 210 °C and 40 bar in water. A commercially available ATR-IR tunnel cell (Axiom, **Figure 4**) was modified to meet the high temperature and pressure conditions. This cell was used for the *in situ* study of support stability under conditions approaching practical conditions for APR. Additional information on catalyst coating and experimental conditions can be found in the experimental section. Details on the principles of ATR-IR spectroscopy in liquid phase heterogeneous catalysis can be found in the literature [13] and references therein.

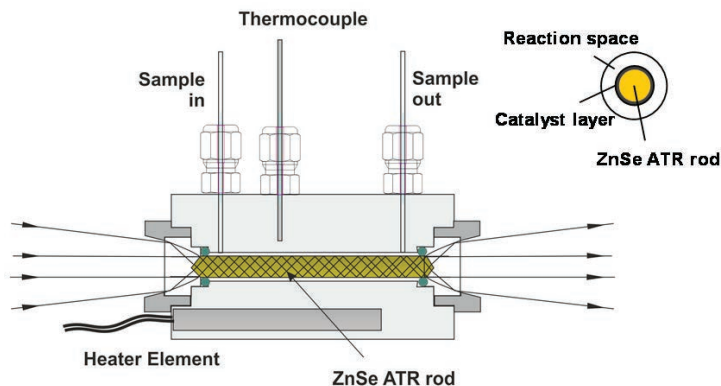


Figure 4. Schematic drawing of ATR-IR tunnel cell and cross section of the catalyst layer coated on the internal reflection element.

Figure 5a shows the ATR-IR absorbance spectrum of boehmite in water at 40 bar and 210 °C. Hydroxyl stretching/ bending vibrations (3305 , 3125 cm^{-1} / 1060 cm^{-1}) corresponding to boehmite can be clearly seen in addition to the typical water bending vibration at 1635 cm^{-1} and hydroxyl stretching between $3200 - 3600$ cm^{-1} .

ATR-IR spectra were collected in a 5 hour experiment during which temperature was increased stepwise from 150 to 210 °C at 40 bar (**Figure 5b**). The sharp peak at 1060 cm^{-1} was integrated to quantify the amount of boehmite present during the experiment (**Figure 5b**, red circles).

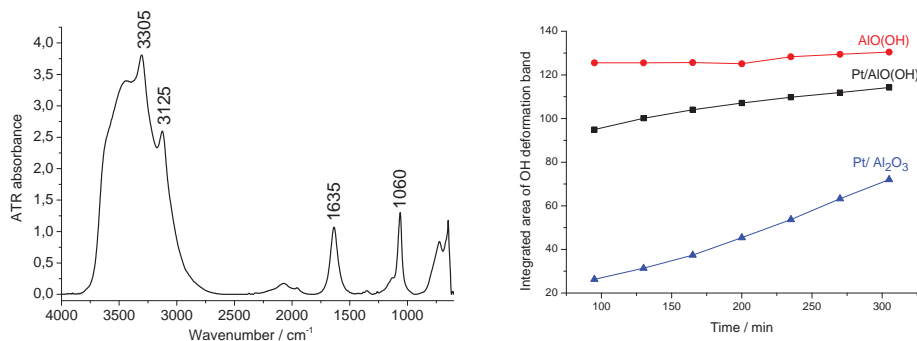


Figure 5. (a) Typical ATR-IR absorbance spectrum of pure boehmite in water at 40 bar and 210 °C; (b) Integrated area of OH deformation peak (1060 cm^{-1}) with time and temperature during catalyst hydrothermal exposure.

It should be noted that the absolute intensities for the three different catalysts cannot be compared quantitatively because of uncertainty about the penetration depth of the evanescent wave in the three samples. Clearly, boehmite is stable in time and at all temperatures. The same experiments were performed for Pt/ γ - Al_2O_3 (blue triangles) and Pt/ $\text{AlO}(\text{OH})$ (black squares). The Pt/ γ - Al_2O_3 catalyst shows a threefold increase in boehmite formation with time and temperature. It is important to note that phase transformation of γ - Al_2O_3 takes place with significant rate even at conditions milder than

practical APR conditions. A full analysis of the kinetics of boehmite formation under these conditions is outside the scope of the present paper, and will be given in a follow-up study [14]. The Pt/AlO(OH) sample shows obviously a much higher intensity than Pt/ γ -Al₂O₃ at the end of stepwise experiment. The boehmite intensity for Pt/AlO(OH) increases slightly with time and temperature, indicative of the presence of some γ -Al₂O₃, which was probably formed by calcining at 350 °C as part of the preparation procedure.

The ATR-IR experiments were also performed on Pt/ γ -Al₂O₃ in the presence of with 0.2 mol/L EG in water (See the Supporting information). This experiment revealed that boehmite formation slowed down in the presence of EG, which is in agreement with earlier studies [19].

Before and after the ATR-IR experiment in water, the Pt particles in both catalysts were characterized by performing CO adsorption experiments on the immobilized layer. The freshly deposited catalyst layer was calcined and reduced as described in the experimental section. After the hydrothermal experiment, the catalyst layer was dried at 150 °C and cooled in He to room temperature. In both situations, CO gas was subsequently introduced into the ATR-IR cell at room temperature. The resulting spectra for Pt/ γ -Al₂O₃ and Pt/AlO(OH) are shown in **Figure 6a and b**, respectively.

CO adsorbed on Pt/ γ -Al₂O₃ shows a broad peak with a maximum at 2072 cm⁻¹ and a shoulder at 2112 cm⁻¹ (**Figure 6a**). The peak at 2072 cm⁻¹ can be ascribed to CO linearly bound on Pt [13, 16, 21]. The peak at 2112 cm⁻¹, is assigned to partially oxidized Pt [21, 22]. After hydrothermal treatment, the 2072 cm⁻¹ band strongly decreased in intensity and shifted slightly to 2069 cm⁻¹, and the band at 2112 cm⁻¹ became more prominent. The clear decrease of accessible Pt surface area as observed in **Figure 6a** is in good agreement with the increase in the particle size of the metal as reported in **Table 1**.

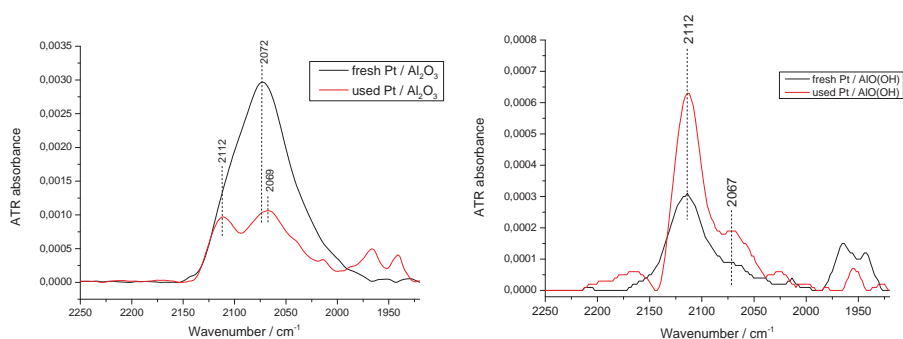


Figure 6. ATR-IR spectra of gas phase room temperature CO adsorbed on (a) fresh and used Pt/ γ -Al₂O₃, (b) fresh and used Pt/AlO(OH). Peaks related to gas phase CO molecule were subtracted.

Figure 6b shows CO adsorbed on fresh and used Pt/AlO(OH) catalyst. Again, the fresh Pt/AlO(OH) shows a broad peak, but this time at 2112 cm⁻¹, this is indicative of

partially oxidized Pt. After hydrothermal exposure this band almost doubled in intensity and a shoulder at 2067 cm^{-1} appeared. Clearly, Pt supported on boehmite is mainly partially oxidized both after reduction of the fresh catalyst as well as after exposure to hydrothermal conditions. The increased intensity of the 2112 cm^{-1} band might point to a redistribution of the Pt particles during the high pressure, high temperature treatment. However, this is speculative at the moment.

We have also shown earlier that during APR of EG [7], phase transformation of $\gamma\text{-Al}_2\text{O}_3$ caused by hydrolysis leads to dissolution and subsequent reprecipitation of boehmite on Pt metal particles. This was attributed to the formation of acetic acid during APR of EG, which was confirmed by separate acetic acid APR experiments [7]. This leads to encapsulation of Pt (**Figure 7**) making the Pt particles not accessible for reactants. Lower amounts of CO adsorbed on the spent Pt/ $\gamma\text{-Al}_2\text{O}_3$ catalyst in our studies (**Figure 6a**) is also in line with this observation.

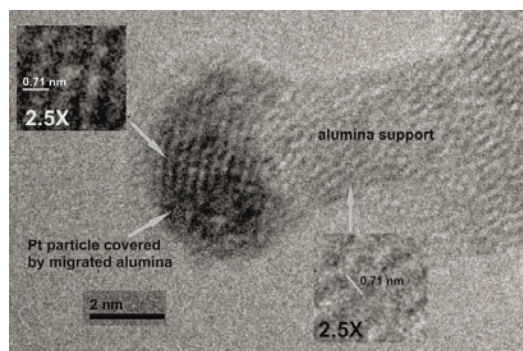


Figure 7. TEM image of Pt particle covered with boehmite phase after acetic acid APR experiment. [Reference 7, D.J.M. de Vlieger, et al.]

Thus, the deactivation of the Pt/ $\gamma\text{-Al}_2\text{O}_3$ catalyst during APR of EG can be attributed to contributions from both metal sintering and coverage of the metal surface caused by the phase change of the support. Loss of surface area as well as the hydroxylation of the surface may both be responsible for the observed Pt particle growth. In contrast, Pt/ $\text{AlO}(\text{OH})$ remains active despite a small decrease in the BET surface area (**Table 1**); apparently this does not cause any metal sintering and metal coverage.

The stability of Pt/ $\text{AlO}(\text{OH})$ under APR conditions makes it an interesting support. **Table 2** shows details of the performance of the two catalysts. The hydrogen formation rate expressed in mole H_2 per sec per mole surface Pt was calculated for the first 30 min on stream. The number of Pt atoms on the surface was calculated based on the metal-particle-size data determined by means of TEM.

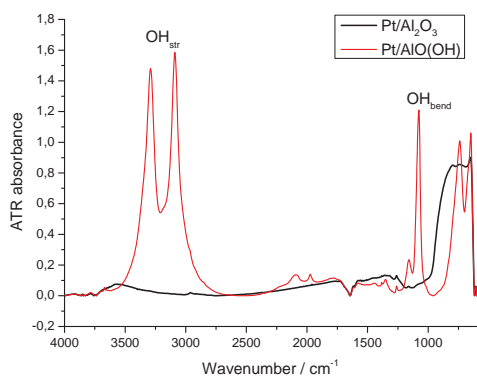
Table 2. Comparison of initial rate of formation of H₂, and selectivities to gas phase carbon containing products, APR, EG, 270 °C, 90 bar

Catalyst	Rate of H ₂ formation (mole/sec·mol Pt _s)	Selectivity (mol. %)		
		CO	CO ₂	C _x H _y ^[a]
Pt/γ-Al ₂ O ₃	1	11	81	9
Pt/AlO(OH)	5	6	92	2
^[a] C ₁ -C ₃ alkanes				

Remarkably, in addition to being stable, Pt/AlO(OH) shows tremendous improvement in the rate of formation of H₂ (**Table 2**) during steam reforming of EG. In contrast, the activity data in **Figure 2** suggest that Pt/AlO(OH) is less active than Pt/Al₂O₃; it should be noted that the Pt loading of the γ-alumina supported catalyst is higher (1.7 versus 1.4 wt. %) and that the initial metal particle size is considerably smaller on γ-Al₂O₃. Even more important is the fact that the selectivity to alkanes is much considerably lower for Pt/AlO(OH), resulting in significantly higher H₂ yield.

Further, the selectivity to CO₂ increased as well, with a corresponding decrease in CO formation, which is indicative for an improved WGS activity. Clearly, all this contributes to an improved H₂ production rate for Pt/AlO(OH).

Figure 8 shows the ATR-IR spectra of the two catalysts in the gas phase. The concentration of hydroxyl groups is significantly higher for Pt/AlO(OH). In bifunctional catalysis involving water (*e.g.*, steam reforming and WGS reactions) activation of water can be the critical step. Water activation on oxidic supports is proposed to occur through the formation of hydroxyl groups depending on the redox properties of the oxide [23, 24].

**Figure 8.** Gas phase room temperature ATR-IR spectra of hydroxyl groups on fresh Pt/γ-Al₂O₃ and Pt/AlO(OH) catalysts.

For our experiments we noticed that the AlO(OH) support enhances the rate of hydrogen formation. We also observed an increased hydroxyl concentration on boehmite in comparison to γ-Al₂O₃. Furthermore, the IR data of adsorbed CO (**Figure 6**)

clearly indicate that Pt is more easily oxidized when supported on AlO(OH). We suggest that these three phenomena are correlated, although we are at this time not in a position to decide on causal relationships. OH groups may be directly relevant by providing a path for water activation. On the other hand, OH groups might be responsible for inducing charge on Pt, whereas charged Pt may enhance the reaction pathway to H₂. Alternatively, it may be suggested that water is able to oxidize Pt under these conditions, which would be in agreement with suggestions by Zhang *et al.* [25] that were based on an XPS study.

In general, based on stability it is suggested that the boehmite phase is suitable for the low temperature APR, whereas γ -Al₂O₃ is more suitable for high temperature SR catalysis. Designing an active, stable, and selective catalyst based on boehmite is promising.

4. Conclusions

ATR-IR experiments revealed a real-time conversion of γ -Al₂O₃ to boehmite under conditions (210 °C and 40 bar) that are even milder than practical conditions for the APR of EG (typically 270 °C). This is in agreement with catalyst deactivation cause by Pt sintering as well as blocking of the Pt surface with boehmite.

The boehmite phase, once formed, is stable at APR conditions. Boehmite is an efficient support for Pt based catalysts for the APR of EG, exhibiting excellent activity for H₂ formation. This may be caused by both the extensively hydroxylated boehmite surface, possibly favoring the bifunctional reforming mechanism involving adsorbed carbonaceous species on Pt and water activation through hydroxyl groups on the support, as well as by enhancing the oxidation of Pt.

5. Acknowledgements

This research has been performed within the framework of the CatchBio program (project nr. 053.70.002). The authors gratefully acknowledge the support of the Smart Mix Program of the Netherlands Ministry of Economic Affairs, Agriculture and Innovation and the Netherlands Ministry of Education, Culture and Science. Authors thank Ing. B. Geerdink for technical support carrying out kinetic and spectroscopic measurements, K. Altena- Schildkamp and Ing. L. Vrielink for help with catalyst characterization, M.A. Smithers and Dr. E.G. Keim, MESA+, for TEM measurements. D.J.M. de Vlieger and A.K.K. Vikla, thank the ACTS hydrogen program (project nr. 053.61.023) for financial support. A.K.K. Vikla is grateful for financial support of TEKES project: BIO-H₂ – Hydrogen from Biomass using Thermo-chemical Methods.

6. References

1. Cortright, R.D., R.R. Davda, and J.A. Dumesic, *Hydrogen from catalytic reforming of biomass-derived hydrocarbons in liquid water*. *Nature*, 2002. **418**(6901): p. 964-967.
2. Kersten, S.R.A., W.P.M. van Swaaij, L. Lefferts, and K. Seshan, *Options for Catalysis in the Thermochemical Conversion of Biomass into Fuels*, in *Catalysis for Renewables*. 2007, Wiley-VCH Verlag GmbH & Co. KGaA. p. 119-145.
3. Takanabe, K., K.I. Aika, K. Seshan, and L. Lefferts, *Sustainable hydrogen from bio-oil - Steam reforming of acetic acid as a model oxygenate*. *Journal of Catalysis*, 2004. **227**(1): p. 101-108.
4. Matas Güell, B., I.V. Babich, L. Lefferts, and K. Seshan, *Steam reforming of phenol over Ni-based catalysts - A comparative study*. *Applied Catalysis B: Environmental*, 2011. **106**(3-4): p. 280-286.
5. de Vlieger, D.J.M., A.G. Chakinala, L. Lefferts, S.R.A. Kersten, K. Seshan, and D.W.F. Brillman, *Hydrogen from ethylene glycol by supercritical water reforming using noble and base metal catalysts*. *Applied Catalysis B: Environmental*, 2012. **111-112**: p. 536-544.
6. Davda, R.R. and J.A. Dumesic, *Catalytic reforming of oxygenated hydrocarbons for hydrogen with low levels of carbon monoxide*. *Angewandte Chemie-International Edition*, 2003. **42**(34): p. 4068-4071.
7. De Vlieger, D.J.M., B.L. Mojet, L. Lefferts, and K. Seshan, *Aqueous Phase Reforming of ethylene glycol - Role of intermediates in catalyst performance*. *Journal of Catalysis*, 2012. **292**: p. 239-245.
8. Manfro, R.L., A.F. Da Costa, N.F.P. Ribeiro, and M.M.V.M. Souza, *Hydrogen production by aqueous-phase reforming of glycerol over nickel catalysts supported on CeO₂*. *Fuel Processing Technology*, 2011. **92**(3): p. 330-335.
9. DeVlieger, D.J.M., D.B. Thakur, L. Lefferts, and K. Seshan, *Carbon Nanotubes: A Promising Catalyst Support Material for Supercritical Water Gasification of Biomass Waste*. *ChemCatChem*, 2012. **4**(12): p. 2068-2074.
10. King, D.L., L. Zhang, G. Xia, A.M. Karim, D.J. Heldebrant, X. Wang, T. Peterson, and Y. Wang, *Aqueous phase reforming of glycerol for hydrogen production over Pt-Re supported on carbon*. *Applied Catalysis B: Environmental*, 2010. **99**(1-2): p. 206-213.
11. Davda, R.R., J.W. Shabaker, G.W. Huber, R.D. Cortright, and J.A. Dumesic, *A review of catalytic issues and process conditions for renewable hydrogen and alkanes by aqueous-phase reforming of oxygenated hydrocarbons over supported metal catalysts*. *Applied Catalysis B-Environmental*, 2005. **56**(1-2): p. 171-186.
12. Antal, M.J., S.G. Allen, D. Schulman, X. Xu, and R.J. Divilio, *Biomass Gasification in Supercritical Water[†]*. *Industrial & Engineering Chemistry Research*, 2000. **39**(11): p. 4040-4053.
13. Mojet, B.L., S.D. Ebbesen, and L. Lefferts, *Light at the interface: the potential of attenuated total reflection infrared spectroscopy for understanding heterogeneous catalysis in water*. *Chem Soc Rev*, 2010. **39**(12): p. 4643-55.
14. Koichumanova, K., K. Seshan, L. Lefferts, and B.L. Mojet, *ATR-IR spectroscopic cell for in situ studies at solid-liquid interface at elevated temperatures and pressures*, to be published, 2015.

15. Wawrzetz, A., B. Peng, A. Hrabar, A. Jentys, A.A. Lemonidou, and J.A. Lercher, *Towards understanding the bifunctional hydrodeoxygenation and aqueous phase reforming of glycerol*. Journal of Catalysis, 2010. **269**(2): p. 411-420.
16. He, R., R.R. Davda, and J.A. Dumesic, *In situ ATR-IR spectroscopic and reaction kinetics studies of water-gas shift and methanol reforming on Pt/Al₂O₃ catalysts in vapor and liquid phases*. J Phys Chem B, 2005. **109**(7): p. 2810-20.
17. Ravenelle, R.M., J.R. Copeland, W.G. Kim, J.C. Crittenden, and C. Sievers, *Structural Changes of γ -Al₂O₃-Supported Catalysts in Hot Liquid Water*. ACS Catalysis, 2011. **1**(5): p. 552-561.
18. MacDonald, D.D. and P. Butler, *The thermodynamics of the aluminium-water system at elevated temperatures*. Corrosion Science, 1973. **13**(4): p. 259-274.
19. Ravenelle, R.M., J.R. Copeland, A.H. Van Pelt, J.C. Crittenden, and C. Sievers, *Stability of Pt/ γ -Al₂O₃ catalysts in model biomass solutions*. Topics in Catalysis, 2012. **55**(3-4): p. 162-174.
20. Tsukada, T., H. Segawa, A. Yasumori, and K. Okada, *Crystallinity of boehmite and its effect on the phase transition temperature of alumina*. Journal of Materials Chemistry, 1999. **9**(2): p. 549-553.
21. Busca, G., E. Finocchio, and V.S. Escribano, *Infrared studies of CO oxidation by oxygen and by water over Pt/Al₂O₃ and Pd/Al₂O₃ catalysts*. Applied Catalysis B: Environmental, 2012. **113-114**: p. 172-179.
22. Primet, M., *Electronic transfer and ligand effects in the infrared spectra of adsorbed carbon monoxide*. Journal of Catalysis, 1984. **88**(2): p. 273-282.
23. Azzam, K.G., I.V. Babich, K. Seshan, and L. Lefferts, *Bifunctional catalysts for single-stage water-gas shift reaction in fuel cell applications. Part 1. Effect of the support on the reaction sequence*. Journal of Catalysis, 2007. **251**(1): p. 153-162.
24. Azzam, K.G., I.V. Babich, K. Seshan, and L. Lefferts, *A bifunctional catalyst for the single-stage water-gas shift reaction in fuel cell applications. Part 2. Roles of the support and promoter on catalyst activity and stability*. Journal of Catalysis, 2007. **251**(1): p. 163-171.
25. Zhang, L., A.M. Karim, M.H. Engelhard, Z. Wei, D.L. King, and Y. Wang, *Correlation of Pt-Re surface properties with reaction pathways for the aqueous-phase reforming of glycerol*. Journal of Catalysis, 2012. **287**(0): p. 37-43.

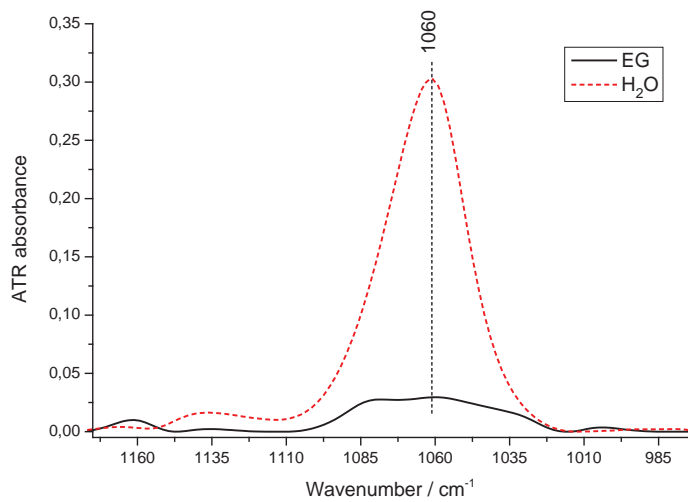


Figure S1. ATR-IR spectra of Pt/ γ -Al₂O₃ in pure water (red dashed line) and in 0.2 mol L⁻¹ EG in water (solid black line) at 200°C 40 bar.

Chapter 4

An in situ ATR-IR spectroscopy study of aluminas under aqueous phase reforming conditions

High temperature/pressure *in situ* Attenuated Total Reflection Infrared (ATR-IR) spectroscopy was used to investigate the phase transformation of support γ -Al₂O₃ into boehmite (AlO(OH)) under the hydrothermal conditions of Aqueous Phase Reforming (APR). Activation energy barriers of boehmite formation in hot compressed water at temperatures between 150 and 180 °C were calculated to be 15.9 ± 4.8 kJ/mol for γ -Al₂O₃ and 43.2 ± 4.3 kJ/mol for Pt/ γ -Al₂O₃. Influence of Pt particles is suggested to slow down the phase transformation by selective blockage of the surface nucleation sites. Presence of ethylene glycol has also an inhibiting effect on the transformation due to the carbon deposits formed on the oxide surface. *Post mortem* analysis using Raman spectroscopy, ¹H and ²⁷Al MAS NMR confirm formation of boehmite.

This chapter has been published as

K. Koichumanova, K.B. Sai Sankar Gupta, L. Lefferts, B. L. Mojet, K. Seshan
An in situ ATR-IR spectroscopy study of aluminas under aqueous phase reforming conditions,
Physical Chemistry Chemical Physics, **2015**
DOI 10.1039/C5CP02168E

1. Introduction

Oxides are widely used as supports in heterogeneously catalyzed reactions. γ - Al_2O_3 is one of the most versatile supports because of its high surface area, meso-porosity, tunable acid base properties and characteristics suitable for commercial applications such as cheapness, thermal / mechanical stability. Many of the heterogeneously catalyzed reactions utilizing γ -alumina as a support are carried out in gas phase (*e.g.* reforming and dehydration), where stability at higher temperatures is usually a benefit. The high surface area of γ -alumina allows preparation of catalysts with small metal particles. Surface acidity of alumina is widely utilized in reactions where both metal and support influence reaction sequence, termed bi-functional catalysis (*e.g.*, Platforming [1], WGS [2, 3] *etc.*). High surface area and meso-porosity of γ -alumina is generally achieved by careful dehydration *via* calcination of hydroxide / oxyhydroxide precursors such as, boehmite, bayerite or gibbsite. The type of precursor and temperature of calcination influences the morphology of the resulting γ -alumina [4]. A number of gas phase FT-IR studies together with DFT calculations are available [4-6] describing changes that take place to surface hydroxyls and also Al-O-Al lattice vibrations during formation of γ - Al_2O_3 from boehmite *via* calcination / dehydration.

Typically, dehydration of boehmite ($\text{AlO}(\text{OH})$) around 500 °C leads to its transformation into γ - Al_2O_3 [4]. Structure of boehmite (**Figure 1a**) can be described as containing corrugated layers of Al-O-Al chains with hydrogen bonding holding the layers together. In this structure Al^{3+} ions are present in exclusively octahedral (Oh) coordination with O^{2-} ions. During calcination these interlayer hydrogen bonds are broken with simultaneous dehydration, creating new Al-O-Al bonds between the layers and resulting in the formation of γ - Al_2O_3 . γ - Al_2O_3 has a defect spinel structure (**Figure 1b**), where Al^{3+} ions are present in both Oh and Tetrahedral (Td) coordination with oxygen ions. Thus, dehydration of boehmite changes coordination of Al^{3+} ions from octahedral to a mixture of Oh and Td sites.

Further, depending on the structure, part of the Al^{3+} ions are coordinated to hydroxyl groups. In the case of boehmite these hydroxyl groups can be present as both surface terminating groups and bulk (interlayer) hydroxyls connected by hydrogen bonding. In case of γ - Al_2O_3 , hydroxyl groups are present as surface terminating groups. Transformations between γ - Al_2O_3 and boehmite are accompanied by changes in the concentration and types of hydroxyl groups. Different spectroscopic techniques can be used to study these different hydroxyls, *e.g.*, IR spectroscopy, ^1H MAS NMR and Raman spectroscopy. ^{27}Al MAS NMR is useful to characterize Al^{3+} coordination, *viz* Oh or Td.

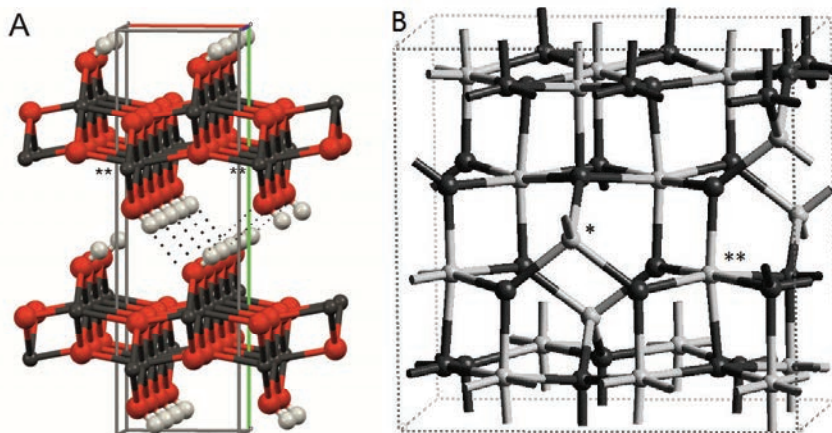


Figure 1. Structures of (a) boehmite (dark grey balls- Al³⁺, red balls – O²⁻, light grey balls -H) and (b) γ -Al₂O₃ (from ref. [7]; light grey balls- Al³⁺, dark grey balls – O²⁻). * - Td, ** - Oh coordination, dotted lines - inter layer hydrogen bonding (only shown in one place as an example).

An increasing number of studies on biomass processing reactions in the last few years have shown that reactions taking place in aqueous phase at elevated temperatures are of great importance. Thus, usage of supports suitable for gas phase reactions in such new environments has become an issue. Morphological stability of the support, leaching and sintering of support as well as metal particles are problems often reported [8-11]. Aqueous phase reforming (APR) is currently of great interest to convert waste biomass derived streams to hydrogen. It is typically performed under severe conditions, *e.g.*, 250 °C, 300 bar. Over the last decade several studies have been carried out to investigate catalyst deactivation caused by hydrothermal instability of the supports used [10, 12-16]. It was shown by de Vlieger *et al.* that transformation of the support into boehmite phase in a Pt/ γ -Al₂O₃ catalyst during aqueous phase reforming of ethylene glycol at supercritical conditions resulted in catalyst deactivation [12]. The authors proposed that support surface area collapse as well as Pt encapsulation associated with the phase transformation as reasons, among others, for this deactivation. Ciftci *et al.* have observed boehmite formation on Pt catalysts supported on γ -Al₂O₃ and on amorphous silica-alumina (ASA) in aqueous phase reforming of glycerol [16]. The higher the Al concentration of ASA, the higher the amount of boehmite [16]. Boehmite, which is an oxy-hydroxide phase is the thermodynamically stable phase of alumina under APR conditions [17]. Earlier studies using long term experiments (up to 6 months) have shown that even at RT, hydration of γ -Al₂O₃ led to its transformation into β -Al(OH)₃, bayerite [18-20].

Boehmite phase is often proposed as an intermediate during transitions involving hydration of γ -Al₂O₃ or dehydration of Al(OH)₃ phases. For hydration in general, two mechanisms of phase change have been proposed, *i.e.*, (i) hydroxylation initiated at the surface Al-O bonds in γ -Al₂O₃ and migration to bulk, (ii) dissolution of γ -Al₂O₃ *via* a

hydrated species and re-precipitation, *e.g.*, as bayerite [18]. In the case of α - Al_2O_3 , Eng *et al.* [21] and Digne *et al.* [7] showed with the help of Surface X-Ray Diffraction (SXRD) that a layer of aluminum hydroxide forms on the surface. In the case of γ - Al_2O_3 , Carrier *et al.* [18] concluded that the increase of aluminum ion content in water with time indicates that dissolution-precipitation process takes place. They also showed formation of large particles (~ 500 nm) of hydroxide phase(s) using TEM and XRD. These experiments were carried out at ambient temperature. Hydration of γ - Al_2O_3 at elevated temperatures was studied in detail by Ravenelle *et al.* [22]. Boehmite formation was complete in hot liquid water at 200 °C and autogenic pressure (14 bar) after 10 h in an autoclave. Formation of isolated boehmite particles on the surface of γ - Al_2O_3 was suggested based on the increased surface area (BET) during the first 4 h. Presence of metal particles, *e.g.*, Pt, Ni, was shown to significantly retard the formation of boehmite by blocking specific surface hydroxyl groups that acted as the initial hydration sites [22]. Moreover, it was shown that the inhibiting effect in the presence of acetic acid on boehmite formation was due to acetylation which chemically blocked surface Al-O bonds. Experiments with glycerol and sorbitol also showed inhibition of boehmite formation. This was explained alternatively as due to the formation of a protective layer of carbonaceous deposit from the polyols [23]. Increasing carbon chain length of the oxygenate was found to enhance this stabilizing effect. Remarkably, the presence of multiple phenolic components from lignin completely blocked formation of boehmite on γ - Al_2O_3 [24]. Thus, chemisorption of functionalized molecules prevents water molecules from hydrating the surface. In the case of APR of such oxygenates, even though the reaction conditions are ideally favorable for the transition of γ - Al_2O_3 to boehmite, presence of functionalized oxygenated molecules may have a stabilizing effect.

Although boehmite formation has been studied extensively based on *post mortem* analysis, there are no *in situ* studies that look at the transformation. This is because performing liquid (aqueous) phase *in situ* experiments using spectroscopic techniques is still a challenge. In this respect, *in situ* ATR-IR spectroscopy technique [15] allows studying APR under realistic temperatures and pressures. This technique also allows studying changes on γ - Al_2O_3 in the presence of metals, *e.g.*, Pt, and functionalized molecules, *e.g.*, ethylene glycol, with respect to temperature and time, *in situ*. The conditions chosen in this study represent typical APR conditions used in kinetic experiments [15].

In this study γ - Al_2O_3 transformation into boehmite phase is studied *in situ* using ATR-IR spectroscopy during APR of ethylene glycol over Pt/ γ - Al_2O_3 catalyst at 230 °C, 40 bar. The influence of temperature, presence of metal particles, and composition of the reaction environment (pure water and reaction media) are discussed.

2. Experimental

2.1 Catalyst preparation

γ -Al₂O₃ (BASF AL-3992) was used as received, 1,5 % wt. Pt/ γ -Al₂O₃ catalyst was prepared by wet impregnation of γ -Al₂O₃. The support was crushed and sieved to a particle size range of 300-600 μ m. H₂PtCl₆.6H₂O (Alfa Aesar) was used as platinum precursor. Alumina support was added to the solution of precursor in water (weight ratio H₂O/ γ -Al₂O₃ = 1.8) and water was removed under vacuum at 100 °C. The catalyst was subjected to a hydrogen reduction treatment (H₂ 100 mL/min, N₂ 100 mL/min) for 5 hours at 100 °C to minimize chlorine content from Pt precursor. Finally, the Pt/ γ -Al₂O₃ catalyst was calcined at 500 °C for 15 hours under air flow (200 mL/min). A boehmite sample, AlO(OH), was prepared by hydrothermal treatment of γ -Al₂O₃ in water at 200 °C and autogenic pressure (14 bar) for 10 h using autoclave with glass liner. Material was then dried under vacuum at 60 °C for 12 hours.

2.2 Catalyst characterization

Platinum loading was measured by means of X-ray fluorescence (XRF; Philips, PW 1480). The surface area was analyzed by nitrogen physisorption using the BET method (Micromeritics, ASAP 2400). The Pt dispersion for the fresh Pt/ γ -Al₂O₃ was measured using CO pulse chemisorption (Micromeritics Chemisorb 2750). Before CO chemisorption, the catalyst was reduced in H₂ at 200 °C for 1 h.

2.3 Catalyst immobilization

The materials were immobilized on an infrared element (IRE) (ZnSe rod, diameter 6.4 mm, length 70 mm, 45° angle of incidence) according to the following procedure. A slurry was made by mixing of 0,150 g of crushed catalyst (fraction < 45 μ m) with 20 mL of isopropanol (spectroscopic grade) which was then spray-coated on a ZnSe rod using an air brush device. Sample loading was estimated to be around 6-15 mg with uniform distribution of material along the rod. The sample was left for drying in air with subsequent *in situ* thermal treatment in the ATR-IR cell to remove traces of solvent. Pre-treatment of the catalyst layer was done in He flow at 150 °C. The sample was then oxidized in O₂/He mixture (50 mL/min) at the same temperature and cooled down to room temperature in 50 vol.% H₂/He flow (50 mL/min).

It is important to note that the catalyst immobilization procedure described above has a number of uncertainties leading to variation in the quality of the layers. Parameters such as porosity, packing of the particles, thickness distribution of the layer along the length, size of the catalyst particles, may be different from layer to layer, which can lead to different IR intensities. Currently, efforts are being made to overcome this problem, however, this limitation can be relieved by comparing the changes in IR

spectra for one sample layer while changing experimental conditions. This approach was utilized in the current study by varying the temperature according to a stepwise heating scheme using one catalyst layer.

2.4 ATR-IR spectra acquisition

ATR-IR spectra were collected using a FT-IR spectrometer (Bruker, Tensor 27) equipped with a liquid nitrogen cooled MCT detector and an ATR-IR Tunnel cell (Axiom) mounted in the sample chamber. A scheme of the Tunnel cell can be found elsewhere [15]. Spectra were recorded with 4 cm^{-1} resolution, averaging 256 scans for background spectra and 128 scans for liquid phase spectra. Spectrum of the pretreated sample on ZnSe IRE was used as a background.

High temperature, high pressure conditions of the reaction were reached using a HPLC pump (Dionex, P680) and pressure in the cell was regulated by a back pressure regulator (**Figure 2**). Degassed water or 0.2 M solution of ethylene glycol was pumped (1 mL/min) into the system until 40 bar and heated to the required APR temperatures (150-230 °C). The sample was first heated to 150 °C, followed by stepwise heating to 230 °C with a 10 °C increment, keeping the sample for 30 minutes isothermally at each step. Spectra were recorded every minute in all cases.

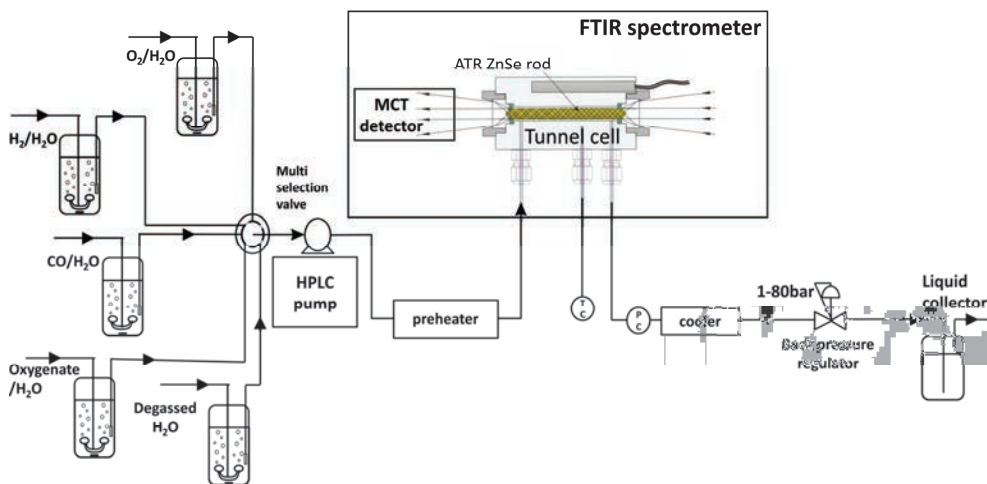


Figure 2. Scheme of the ATR-IR setup.

In a direct heating experiment, a sample was heated to 230 °C at 40 bar in a single step that took typically 30 min. Spectra were then collected during 310 min after the final temperature was reached.

In case of a stepwise heating experiment with 0.2 M ethylene glycol solution, sample was first heated to 150 °C, followed by stepwise heating to 225 °C with a 25 °C

increment, keeping the sample for 15 min isothermally at each step. Spectra were collected every minute.

2.5 Temperature Programmed Oxidation

TPO of fresh and spent samples was performed to detect carbonaceous deposits on the surface. Samples were scratched from the ZnSe substrate and loaded into a quartz tube with quartz wool. Pretreatment of the samples consisted of treatment in He (25 mL/min) at 150 °C for 30 min and cooling down to 25 °C. Samples were then oxidized in 5% O₂/He mixture flow (25 mL/min) during heating to 750 °C with a heating rate of 5 °C/min. CO or CO₂ formed was converted to methane in an online methanizer (Model 110 Chassis, SRI Instruments Europe GmbH) using Ni catalyst. An FID detector was used for quantifying methane. Al₂(CO₃)₃ was used for calibration of the FID detector.

2.6 Raman spectroscopy

Measurements were performed at ambient conditions using a Raman Spectrometer (Bruker, Senterra) with a cooled CCD detector. Samples scratched from the surface of ZnSe rod were used for the analysis. Spectra were recorded in the frequency range 120-1200 cm⁻¹ with a resolution of 9-15 cm⁻¹. Each spectrum was the sum of 200 scans. A laser with a wavelength of 785 nm and 5 mW power was used for all samples.

2.7 Solid state ¹H and ²⁷Al MAS NMR analysis

Experiments were performed in 9.4 T on a Bruker DMX-400 spectrometer equipped with a 4 mm triple channel MAS probe. At this magnetic field, ¹H and ²⁷Al nuclei resonate at 399.33 MHz and 104.05 MHz frequencies, respectively. Standard ZrO₂ rotors were used for spinning the sample up to 13 kHz. Due to the small amount of sample available from ATR-IR experiment for post-characterization with MAS NMR, hydrothermal conversion of γ -Al₂O₃ and Pt/ γ -Al₂O₃ samples was mimicked in a fix-bed reactor with H₂O at 230 °C, 40 bar (2 mL/min) for 30 min. All samples were dried overnight in an oven at 180 °C prior to the analysis.

For the acquisition of ²⁷Al MAS spectra, pulse duration of 0.25 μ s ($\pi/24$ pulse of liquid Al(NO₃)₃) was used with a recycle delay of 500 ms. 2048 scans were recorded for all of the samples. The chemical shifts of ²⁷Al were referenced externally with respect to Al(NO₃)₃ in aqueous solution, which is zero. Line broadening function of 50 Hz was used to process the data. For the necessary samples, experiments were performed with a spinning speed of 10 kHz to distinguish between isotropic chemical shift and spinning side bands. For the acquisition of ¹H MAS spectra, $\pi/2$ pulse of duration 3 μ s with a recycle delay of 1 s was used. The number of scans accumulated was 64. A line

broadening function of 10 Hz was used to process the data. The chemical shifts of ^1H were referenced externally with respect to TMS.

3. Results

$\gamma\text{-Al}_2\text{O}_3$ used in the current study had a surface area of 174 m^2/g . The prepared Pt/ $\gamma\text{-Al}_2\text{O}_3$ catalyst contained 1.5% wt. Pt according to XRF analysis, 66% metal dispersion (corresponding to 1.7 nm Pt particles) as measured by CO chemisorption and a BET surface area of 180 m^2/g .

To be able to compare intensities of the infrared peaks between different samples in ATR-IR spectra, it is necessary to determine whether the depth of penetration of infrared light is similar for all samples. It is also important to know whether the probed depth is smaller than the thickness of the layer. Calculations of penetration depths and layer thicknesses are summarized in **Table S1** in the Supporting Information section. Results show that depths of penetration for both $\gamma\text{-Al}_2\text{O}_3$ and Pt/ $\gamma\text{-Al}_2\text{O}_3$ are similar and are around 0.82 μm , whereas estimations for $\text{AlO}(\text{OH})$ result in 0.98 μm . It is clear that in all cases the penetration depth of the evanescent wave is smaller than the layer thicknesses ($>2 \mu\text{m}$), thus catalyst particles as well as liquid in the interparticle space and pores are probed during the experiment.

3.1 *In situ* ATR-IR spectra and peak assignments

Figure 3 shows the ATR-IR spectra of the samples at the end of the stepwise heating procedure, *i.e.* at 230 $^\circ\text{C}$, 40 bar. Spectra of $\gamma\text{-Al}_2\text{O}_3$ (**Figure 3b**) and Pt/ $\gamma\text{-Al}_2\text{O}_3$ (**Figure 3c**) show similar spectral features, namely a broad peak at 3200-3600 cm^{-1} , a sharp peak at 1640 cm^{-1} ($\text{OH}_{\text{H}_2\text{O}}^{1640}$) and a weak broad band at 2050 cm^{-1} , all assigned to stretching- and rotational-vibrations and a combination band of water, respectively. The sharp peak at 1064 cm^{-1} ($\text{OH}_{\text{AlO}(\text{OH})}^{1064}$) and shoulder bands at 3304 and 3124 cm^{-1} were assigned to OH deformation and stretching vibrational modes of boehmite phase, respectively [11, 25-28]. They are also similar for both materials. Comparison with the spectrum of boehmite [$\text{AlO}(\text{OH})$], at the same hydrothermal conditions (230 $^\circ\text{C}$, 40 bar) (**Figure 3d**), confirms the peak assignments given above. There are also several broad bands under the $\text{OH}_{\text{AlO}(\text{OH})}^{1064}$ peak, which are temperature dependent (**Figure S1**, Supplementary Information). Interestingly, these bands also appeared when the cell was filled with a high boiling point liquid, *n*-dodecane ($n\text{-C}_{12}\text{H}_{26}$), and was heated to 200 $^\circ\text{C}$ (**Figure S2**, Supplementary Information). These broad peaks are therefore probably artifacts caused by cell at high temperature.

It is reasonable to correlate the intensity of the $\text{OH}_{\text{AlO}(\text{OH})}^{1064}$ peak to the extent of boehmite formation since it does not overlap with any strong peaks caused by water vibrations and spectra that are in comparison were recorded at the same

temperature/pressure. In the inset of **Figure 3** the intensity of $\text{OH}_{\text{AlO}(\text{OH})}^{1064}$ is similar for (b) and (c) cases. Considering that the amounts of alumina were similar and depths of penetration were the same for both alumina samples (**Table S1**) this may indicate that both $\gamma\text{-Al}_2\text{O}_3$ and Pt/ $\gamma\text{-Al}_2\text{O}_3$ have a similar amount of alumina converted into boehmite. Determination of exact conversion levels is more complex, since depth of penetration for $\text{AlO}(\text{OH})$ is 20% higher than for $\gamma\text{-Al}_2\text{O}_3$ (**Table S1**). However, it is clear from the inset in **Figure 3** that the intensity of $\text{OH}_{\text{AlO}(\text{OH})}^{1064}$ peak for $\text{AlO}(\text{OH})$ (d) is much higher than one for other two samples (b and c). Even after taking into account the difference in depth of penetration for the two samples (higher for boehmite), it is clear that in both $\gamma\text{-Al}_2\text{O}_3$ and Pt/ $\gamma\text{-Al}_2\text{O}_3$ only partial transformation to boehmite occurred.

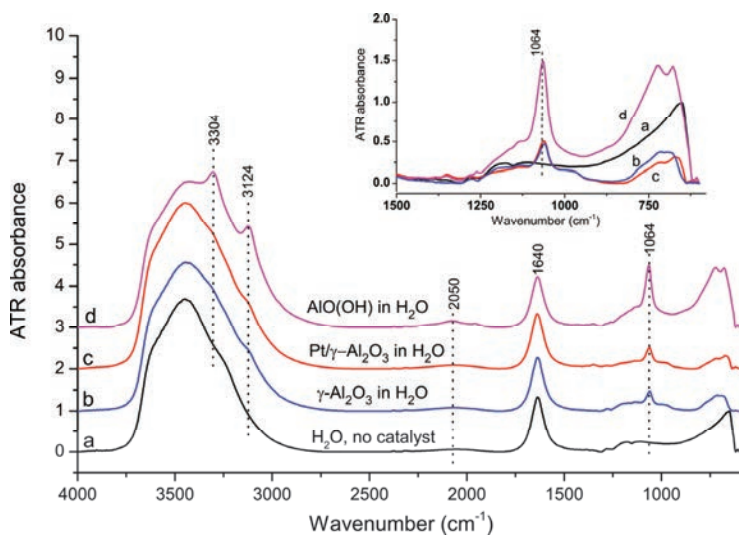


Figure 3. *In situ* ATR-IR spectra at 230 °C and 40 bar of (a) H_2O on a bare IRE, (b) $\gamma\text{-Al}_2\text{O}_3$ in H_2O , (c) Pt/ $\gamma\text{-Al}_2\text{O}_3$ in H_2O and (d) $\text{AlO}(\text{OH})$ in H_2O . Spectra were taken at the end of all heating steps, at 230 °C and 40 bar. Inset: 1064 cm^{-1} peak for all samples.

3.2 Influence of temperature - stepwise heating

The changes in the spectra during the stepwise heat treatment from 150 to 230 °C were studied next. **Figure 4** shows *in situ* ATR-IR spectra of $\gamma\text{-Al}_2\text{O}_3$ in H_2O for the $\text{OH}_{\text{AlO}(\text{OH})}^{1064}$ region as a function of temperature. Spectra presented here were collected after 30 min at each isothermal step. The characteristic $\text{OH}_{\text{AlO}(\text{OH})}^{1064}$ peak is seen to grow with increasing temperature, suggesting an influence of temperature on boehmite formation from $\gamma\text{-Al}_2\text{O}_3$.

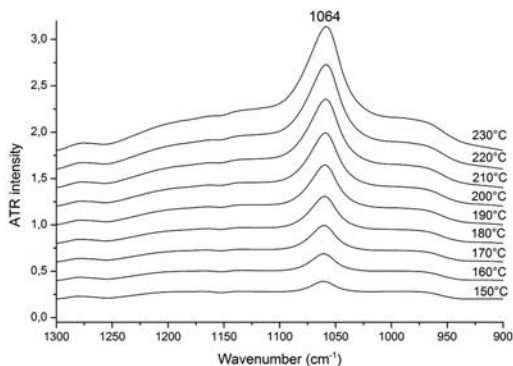


Figure 4. ATR-IR spectra of γ -Al₂O₃ in 1 mL/min H₂O during stepwise heating from 150 to 230 °C and 40 bar after 30 min at each temperature.

3.3 ATR-IR spectra in presence of ethylene glycol

Further, influence of the presence of ethylene glycol in water on boehmite formation was also studied for both γ -Al₂O₃ and Pt/ γ -Al₂O₃. For this, samples were heated in 0.2 M solution of ethylene glycol at 150-225 °C and 40 bar. Stepwise heating scheme was also used in these experiments. **Figure 5** shows *in situ* ATR-IR spectra that demonstrate the changes that occur to different samples after treatment at 225 °C and 40 bar, in relation to fresh sample (initial spectra at RT, 40 bar). Spectra were normalized by the OH_{H₂O}¹⁶⁴⁰ peak, assigned to water rotational band, to allow comparison of the intensities of OH_{AlO(OH)}¹⁰⁶⁴ peak for samples exposed to H₂O and ethylene glycol solution. Intensities of the OH_{AlO(OH)}¹⁰⁶⁴ peak are significantly higher for samples treated in H₂O (**Figure 5a and b**) as compared to samples treated in ethylene glycol (**Figure 5c and d**).

To describe the influence of temperature on the formation of boehmite, the OH_{AlO(OH)}¹⁰⁶⁴ peak (**Figure 4**) was integrated in the wavenumber range between 1110-1013 cm⁻¹ using integration method available in the OPUS software. Straight line was drawn between these limits representing the baseline for peak integration. Example of the baseline position is given in **Figure 7**. Integrated areas were then plotted against time (**Figure 6**) and apparent rates of boehmite formation were derived. It is important to note that the Y-axis is not calibrated to quantitative boehmite concentrations, but intensity of the OH_{AlO(OH)}¹⁰⁶⁴ peak is proportional to level of alumina conversion and the slopes of the trend lines can be compared in terms of the rate of boehmite formation. The apparent rate of boehmite formation for both γ -Al₂O₃ (**Figure 6**, upward triangles) and Pt/ γ -Al₂O₃ (**Figure 6**, circles) gradually increases with increasing temperature and does not further change during 30 minutes once the temperature is stabilized. Differences between effect of temperature on rates for γ -Al₂O₃ and Pt/ γ -Al₂O₃ samples will be discussed further.

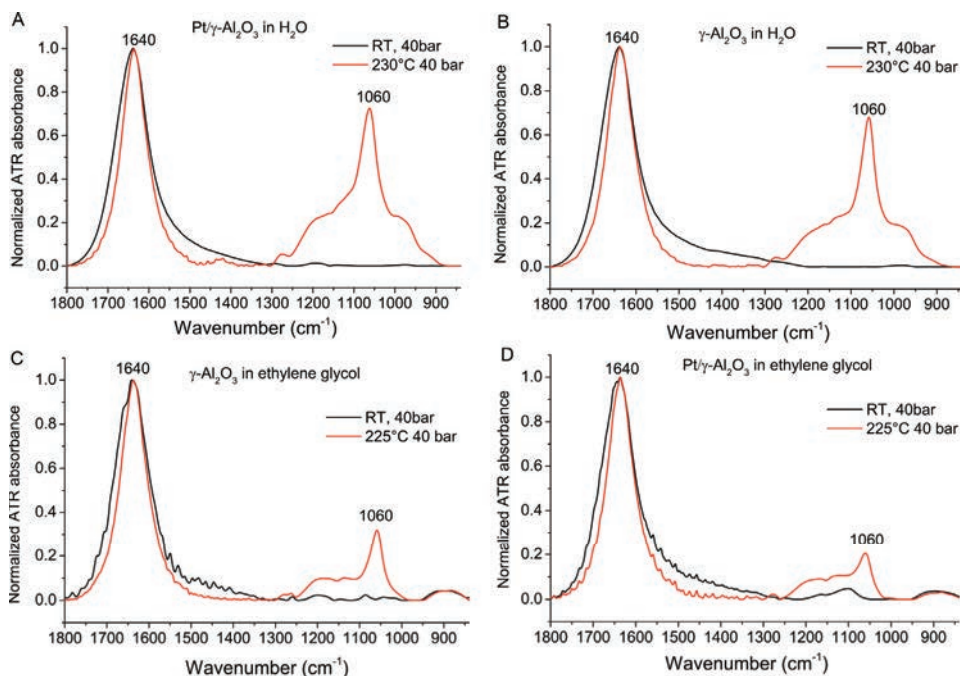


Figure 5. In situ ATR-IR spectra of at RT (black) and 230 °C, 40 bar (or 225 °C, 40 bar for EG) (red) after stepwise heating of Pt/ γ -Al₂O₃ in H₂O (a), in ethylene glycol (d), and γ -Al₂O₃ in H₂O (b), in ethylene glycol (c). All spectra were normalized by 1640 cm⁻¹ peak for better comparison.

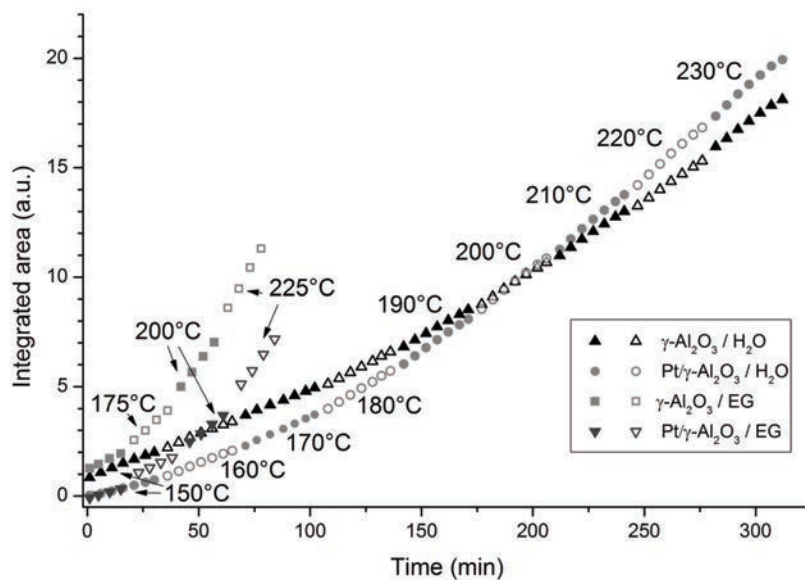


Figure 6. Integrated areas of OH_{AlO(OH)}¹⁰⁶⁴ for γ -Al₂O₃ and Pt/ γ -Al₂O₃ in H₂O and in 0.2 M ethylene glycol solution at different temperatures between 150-230 °C, 40 bar. Linear fit for 230 °C: $y=0,0729x-5,4$.

3.4 Direct heating scheme

A direct heating scheme was also used in addition to stepwise heating experiments. In this case the sample was heated from RT to 230 °C in 30 min and left at 230 °C for 310 min. **Figure 7** shows two spectra of Pt/ γ -Al₂O₃ in H₂O after direct heating to 230 °C - immediately after reaching 230 °C (black) and after 310 min at the same temperature (red). It is obvious that some amount of boehmite has been formed already during heating to 230 °C (black) and the amount of boehmite increased significantly during isothermal heating.

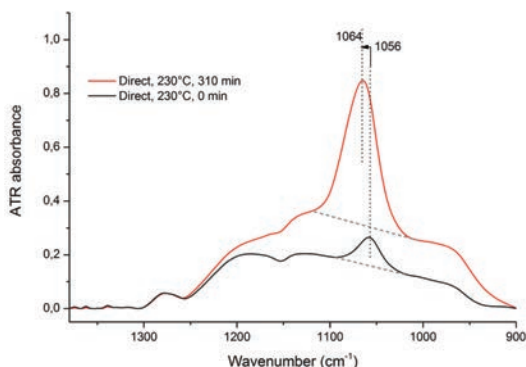


Figure 7. ATR-IR spectra of Pt/ γ -Al₂O₃ in H₂O at 230 °C and 40 bar immediately after direct heating from RT to 230 °C (black line) and after 310 min at 230 °C (red line). Dashed lines represent the baseline used in peak integration.

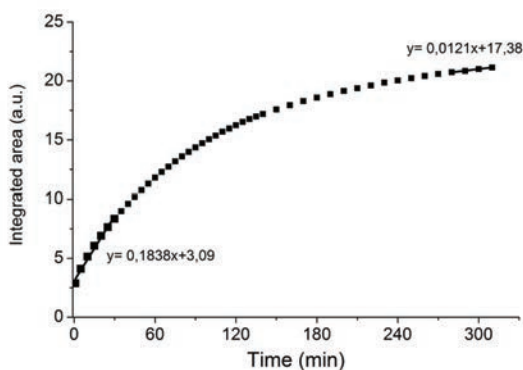


Figure 8. Integrated area of OH_{AlO(OH)}¹⁰⁶⁴ peak during 310 min experiment with direct heating of Pt/ γ -Al₂O₃ to 230 °C, 40 bar in H₂O.

Figure 8 shows integrated areas of OH_{AlO(OH)}¹⁰⁶⁴ peak during the isothermal experiment at 230 °C. The rate of boehmite formation calculated during first 30 minutes at 230 °C is much higher as compared to the last 30 minutes and the formation of boehmite clearly slows down with time.

3.5 Raman spectroscopy

Raman spectra of the samples were taken before and after the ATR-IR experiment to investigate the presence of different alumina phases along with boehmite. Raman spectra of samples after exposure to hot compressed water presented in **Figure 9** show multiple overlapping peaks. Based on literature, peaks at 491, 360 and 672 cm^{-1} are assigned to boehmite [28, 29]. Peaks at 443 and 305 cm^{-1} are assigned to bayerite or gibbsite [20]. Since these peaks appear as shoulders to boehmite peaks we conclude that other alumina phases are also present in our samples, but in smaller amounts.

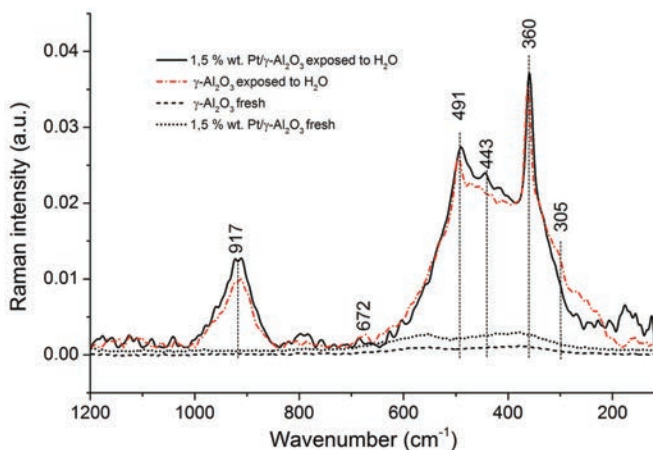


Figure 9. Raman spectra of $\gamma\text{-Al}_2\text{O}_3$ and 1.5% wt. Pt/ $\gamma\text{-Al}_2\text{O}_3$ before and after exposure to hot compressed water.

3.6 ^{27}Al MAS NMR spectroscopy

The chemical environment of aluminium ions vary in (hydroxylated) aluminas and this can be probed with MAS NMR. ^{27}Al MAS NMR analysis was performed to study the changes in aluminium coordination during transformation of $\gamma\text{-Al}_2\text{O}_3$ into boehmite. **Figure 10a** shows the spectra of Pt/ $\gamma\text{-Al}_2\text{O}_3$ and $\gamma\text{-Al}_2\text{O}_3$ exposed to H_2O at 230 $^\circ\text{C}$, 40 bar for 30 min as described in Experimental Section (NMR), a spectrum of fresh $\gamma\text{-Al}_2\text{O}_3$ and a spectrum of a boehmite sample. The two peaks at 70 and 8 ppm are typically assigned to tetrahedral (Td) and octahedral (Oh) Al^{3+} coordination, respectively. $\gamma\text{-Al}_2\text{O}_3$ shows Al in both Oh and Td positions while boehmite exhibits only octahedral coordination at 8 ppm [30, 31]. Exposed $\gamma\text{-Al}_2\text{O}_3$ and Pt/ $\gamma\text{-Al}_2\text{O}_3$ have higher intensity of octahedral coordinated alumina indicating higher amount of boehmite present in these samples compared to fresh $\gamma\text{-Al}_2\text{O}_3$. In the case of Pt/ $\gamma\text{-Al}_2\text{O}_3$, Td coordinated Al^{3+} can still be seen (**Figure 10b**) indicating presence of $\gamma\text{-Al}_2\text{O}_3$. $\gamma\text{-Al}_2\text{O}_3$ exposed to water shows no Td coordinated Al^{3+} .

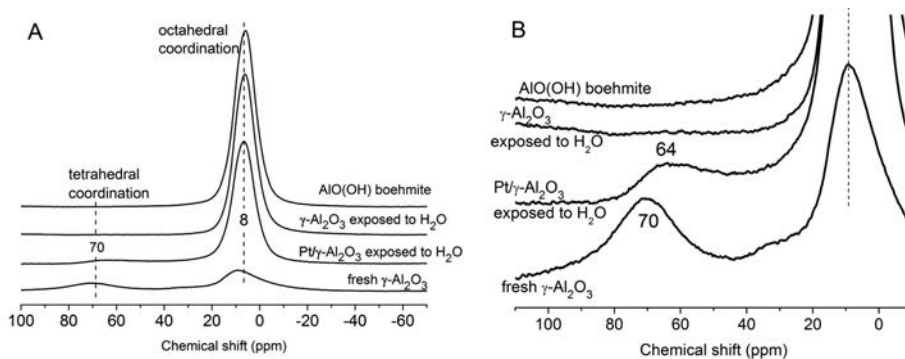


Figure 10. (a) ^{27}Al MAS NMR spectra of Pt/ $\gamma\text{-Al}_2\text{O}_3$ and $\gamma\text{-Al}_2\text{O}_3$ exposed to hot compressed water H_2O at 230 °C, 40 bar, a spectrum of fresh $\gamma\text{-Al}_2\text{O}_3$ and a spectrum of AlO(OH) sample; (b) Zoomed spectra in 100-10 ppm region.

3.7 ^1H MAS NMR spectroscopy

^1H MAS NMR spectroscopy was used to study different hydroxyl groups on the surface of fresh $\gamma\text{-Al}_2\text{O}_3$ and Pt/ $\gamma\text{-Al}_2\text{O}_3$. In the **Figure 11** four peaks with chemical shifts of -0.1, 1.3, 4, 5.7 ppm were observed in the case of fresh $\gamma\text{-Al}_2\text{O}_3$ sample (**Figure 8**, spectra as observed without deconvolution). Pt/ $\gamma\text{-Al}_2\text{O}_3$ sample, however, has only three hydroxyl groups corresponding to peaks at 1.3, 4 and 5.7 ppm.

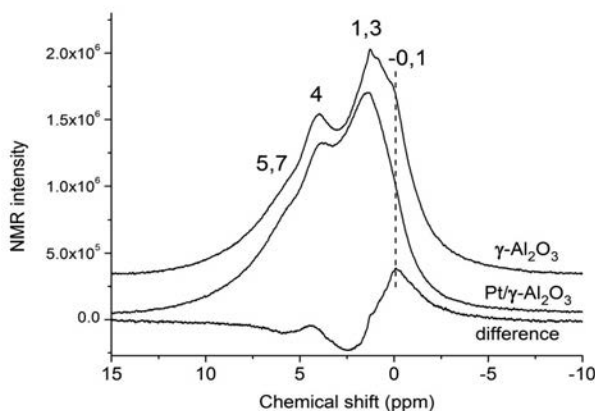


Figure 11. ^1H MAS NMR spectra of fresh Pt/ $\gamma\text{-Al}_2\text{O}_3$, $\gamma\text{-Al}_2\text{O}_3$ samples and a difference spectrum.

Knozinger and Ratnasamy [32] suggested the presence of five types of hydroxyl groups on $\gamma\text{-Al}_2\text{O}_3$. Ravenelle *et al.* [22] showed, in agreement, that deconvolution of the broad MAS NMR bands can reveal presence of all these hydroxyls. From the literature [30] it is known that 5.7 and 4 ppm peaks correspond to a hydroxyl group, derived from adsorbed water, whereas 1.3 and -0.1 ppm belong to surface hydroxyl groups of $\gamma\text{-Al}_2\text{O}_3$. A difference spectrum between two spectra shows a peak at -0.1 ppm, which is only

present in γ -Al₂O₃ sample. Thus, this indicates that Pt/ γ -Al₂O₃ sample lacks one type of hydroxyl group.

3.8 Temperature programmed oxidation

Figure 12 shows TPO profiles of Pt/ γ -Al₂O₃ before and after treatment in 0.8 M EG at 230 °C, 40 bar. TPO profile of Pt/ γ -Al₂O₃ after treatment has peaks at 320 °C and 450 °C whereas profile of fresh Pt/ γ -Al₂O₃ has low intensity peak at 300 °C. Presence of peaks on fresh sample can be explained by remains of the precursor from catalyst preparation step. Peaks on spent catalyst indicate formation of carbonaceous deposits. Coke content was calculated to be 0.8 wt. % for sample treated in 0.8 M EG solution.

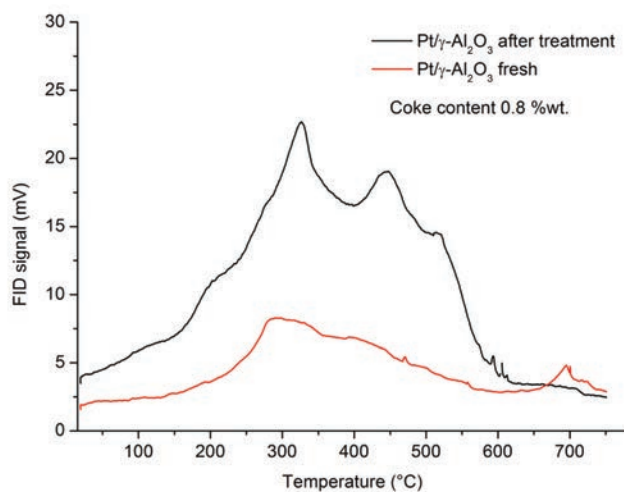


Figure 12. Temperature programmed oxidation profiles for fresh Pt/ γ -Al₂O₃ (red) and Pt/ γ -Al₂O₃ after treatment in 0.8 M EG solution (black).

4. Discussion

4.1 Influence of temperature on boehmite formation

Hydration of γ -alumina and formation of boehmite is the reverse of calcination of boehmite. Surface properties, morphology, surface area and aluminium coordination change during the phase transition. This transformation can be sped up at higher temperatures. In an aqueous phase reforming reaction boehmite formation on the surface of the catalyst can already happen during preheating of the reactor in the flow of reactant (temperatures below 230 °C). *In situ* ATR-IR spectra in the temperature region between 150 and 230 °C show that amount of formed boehmite increases with temperature (**Figure 4**). In addition, **Figure 6** shows that apparent rates of boehmite formation are increasing with temperature.

4.2 Direct vs. stepwise heating

Results for the stepwise heating and the alternate direct heating to the required temperature can be recalled in **Figures 6 and 8**, respectively. They indicate that the apparent rates of boehmite growth in both heating schemes are different. In direct heating, the apparent rate of boehmite formation during the first 30 min is much higher than during the last 30 min at 230 °C (**Figure 8**). This suggests that the rate depends on the concentration of available alumina and the order of the reaction in alumina is higher than zero. When these rates are compared to the rate observed in stepwise heating (**Figure 6**) at same temperature (230 °C) it becomes clear that the apparent rate measured in stepwise heating is not the initial rate. This is due to different conversion levels of alumina at the start of 230 °C step in both experiments. Thus, results obtained in stepwise heating experiment should be interpreted carefully and rates at different temperatures cannot be compared directly. However, the data in **Figure 6** obtained at low temperatures is obtained under differential conditions and therefore the rates measured in the lower temperature region can be compared quantitatively.

Therefore, **Figure 13** gives Arrhenius plots for both $\gamma\text{-Al}_2\text{O}_3$ and Pt/ $\gamma\text{-Al}_2\text{O}_3$ samples in H_2O in the temperature window 150 and 180 °C. **Figure 13** also includes Arrhenius plots for both samples in ethylene glycol solution in the temperature region between 150 and 200 °C. In this case shorter heating times were used to keep conversion levels low (see Experimental Section). Clear differences in slopes of the trend lines can be seen between Pt/ $\gamma\text{-Al}_2\text{O}_3$ and $\gamma\text{-Al}_2\text{O}_3$ samples in water (open squares and solid triangles, respectively). The difference in the slope implies that the activation barrier for boehmite formation is significantly higher when Pt is present. The role of Pt in this context will be discussed later.

Despite the fact that ATR absorbance was not calibrated for boehmite concentrations, it is possible to calculate activation energy barriers from the slopes of the trend lines for the range of temperatures where conversion level is low. This is because the ATR-IR intensities are proportional to the amount of boehmite in the layer. Thus, the activation energies (calculated from data in **Figure 6**) were 15.9 ± 4.8 kJ/mol for $\gamma\text{-Al}_2\text{O}_3$ in H_2O , and 43.2 ± 4.3 kJ/mol for Pt/ $\gamma\text{-Al}_2\text{O}_3$ in H_2O . However, when EG is present, the activation barriers for the two samples, *i.e.* $\gamma\text{-Al}_2\text{O}_3$ in EG and Pt/ $\gamma\text{-Al}_2\text{O}_3$ in EG, were similar and 37.3 ± 3.5 kJ/mol, respectively. The data points outside these temperature regions strongly deviate from straight line, since they were measured in non-differential conditions. The rates are therefore lower than what would be measured in a differential experiment.

Presence of boehmite was also confirmed by ^{27}Al MAS NMR analysis (**Figure 10**). Clear difference in Oh coordination of Al^{3+} for alumina and boehmite phases proves boehmite presence. Higher peak intensity at 70 ppm corresponding to Td coordination

of Al^{3+} in $\text{Pt}/\gamma\text{-Al}_2\text{O}_3$ compared to $\gamma\text{-Al}_2\text{O}_3$ (**Figure 10b**) suggests that transformation into boehmite is incomplete for $\text{Pt}/\gamma\text{-Al}_2\text{O}_3$.

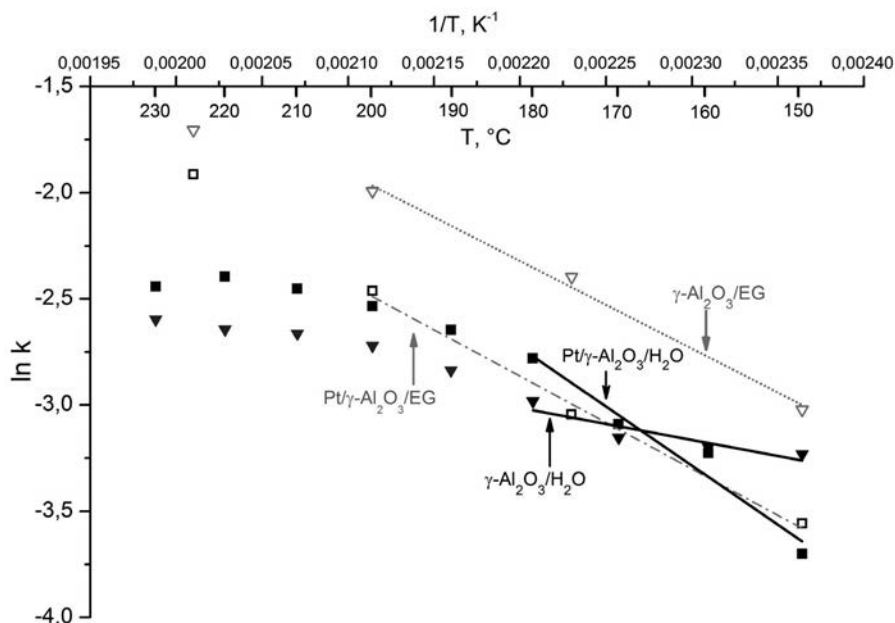


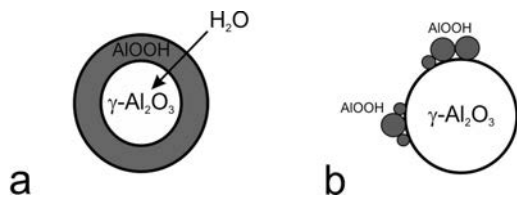
Figure 13. Arrhenius plot of boehmite formation in temperature range 150–200 °C for $\gamma\text{-Al}_2\text{O}_3/\text{H}_2\text{O}$ (solid triangles), $\gamma\text{-Al}_2\text{O}_3/\text{EG}$ (open triangles), $\text{Pt}/\gamma\text{-Al}_2\text{O}_3/\text{H}_2\text{O}$ (solid squares), $\text{Pt}/\gamma\text{-Al}_2\text{O}_3/\text{EG}$ (open squares).

Raman spectra of fresh and used samples (**Figure 9**) showed mainly the presence of boehmite, however shoulder peaks assigned to bayerite or gibbsite were also detected. As it was seen from literature, a variety of hydroxylated aluminas exist in nature in addition to boehmite and as a result hydration of $\gamma\text{-Al}_2\text{O}_3$ can lead to formation of any of these phases. Bayerite ($\beta\text{-Al}(\text{OH})_3$), gibbsite ($\gamma\text{-Al}(\text{OH})_3$) or diaspore ($\gamma\text{-AlO}(\text{OH})$) can be formed as a result of alumina hydration [18–21]. Previous Raman studies [29], confirm that it is difficult to separate different aluminium hydroxide phases as they can co-exist in metastable phases. We conclude here that the majority of the hydroxylated phase present is boehmite as seen from ATR-IR, Raman and ^{27}Al MAS NMR results.

4.3 Boehmite formation from $\gamma\text{-Al}_2\text{O}_3$

Transformation of γ -alumina into boehmite can follow two mechanisms as discussed by Carrier *et al.* [18], *i.e.* (i) surface hydration through hydrolysis of surface Al-O bonds or (ii) alumina dissolution and subsequent precipitation. In the first mechanism, a new phase will be formed in the surface layers and this process may be influenced by diffusion of water through these layers (**Scheme 1a**). In the second

mechanism, γ -alumina dissolution is followed by precipitation of particles of new phase on the surface resulting in a heterogeneous surface morphology (**Scheme 1b**). In the current study it is not possible to make a specific distinction between the two routes.



Scheme 1. Boehmite formation on γ - Al_2O_3 particle via (a) surface hydration mechanism, (b) dissolution-precipitation mechanism.

We have, however, shown that presence of Pt or ethylene glycol, both retard the transformation of γ - Al_2O_3 to boehmite. In the case of Pt, different activation energy barriers for Pt/ γ - Al_2O_3 catalyst and γ - Al_2O_3 support indicate an influence of Pt metal nanoparticles. Thus, boehmite formation is delayed in presence of Pt particles. It was suggested [22] that certain types of surface sites on the support, possibly specific OH functional groups are attacked by water and act as nucleation sites for boehmite growth. The influence of Pt is probably due to selective blockage of these sites. This suggestion [22] of the blockage of hydroxyl groups cannot be evaluated using ATR-IR spectroscopy, because of the presence of liquid water, but can be probed with ^1H MAS NMR.

Comparison of ^1H MAS NMR spectra of γ - Al_2O_3 and Pt/ γ - Al_2O_3 (**Figure 11**) shows that the latter does not exhibit a distinct shoulder at -0.1 ppm, which can be seen clearly in the difference spectrum. This peak corresponds to mono-coordinated OH group as reported by Knozinger and Ratnasamy [32]. It is possible that Pt binds preferentially to this type of mono-coordinated hydroxyl group and, thus in agreement with Ravenelle *et al.* [22] hinders the transformation to boehmite.

Another factor that influences is the presence ethylene glycol (**Figure 5**). It can be seen from the spectra that γ - Al_2O_3 transforms to boehmite in water easily (**Figure 5a**) and presence ethylene glycol inhibits the transformation (**Figure 5 b, c, d**). To recall, activation energy barriers were 15.9 ± 4.8 kJ/mol for γ - Al_2O_3 in water and 37.3 ± 3.5 kJ/mol for γ - Al_2O_3 in EG (**Figure 13**).

TPO profiles (**Figure 12**) of samples treated in ethylene glycol show presence of low (320 °C) and high (450 °C) temperature peaks, confirming the presence of carbonaceous deposits. As was shown by Ravenelle *et al.* [23], oxygenates form a layer of carbonaceous deposits on the surface, which protect the surface from hydrolytic attack. It was also suggested by Absi-Halabi *et al.* [33] and Stanislaus *et al.* [34] that in case of acetic acid the formation of acetate bridges suppresses the hydration of alumina. We have shown earlier [12] that during APR of ethylene glycol on Pt/ γ - Al_2O_3 that a coke layer was deposited on the catalyst. Thus, similar to Pt, carbon deposited may be blocking nucleation sites and protecting the surface from hydroxylation to some extent.

Surprisingly, when both Pt and EG are present (as in the case of Pt/ γ -Al₂O₃ in EG) activation energies are similar, the effect is not cumulative. In this case, it is possible that the presence of Pt which enhances steam reforming activity minimizing formation of carbonaceous deposits.

In general, both mechanisms, discussed above, require hydrolysis of the Al-O bond and formation of unit structures of boehmite O=Al-OH. Three dimensional growth of these specie in layers and interlayer connection *via* hydrogen bonding leads to boehmite structure.

5. Conclusions

Development of the high temperature/pressure *in situ* Attenuated Total Reflection Infrared (ATR-IR) spectroscopy allows to study changes that happen to alumina based catalysts used in the Aqueous Phase Reforming (APR) under realistic conditions. Activation energy barriers for the transformation of catalyst support γ -Al₂O₃ to boehmite were calculated based on changes in the characteristic spectral intensities. Formation of boehmite was established by Raman spectroscopy and ²⁷Al MAS NMR analysis of fresh and used samples. Based on the presented results and in agreement with other studies, it is suggested that Pt hinder the transformation by association with mono-coordinated OH groups, which are nucleation points for the transformation to boehmite. The inhibiting effect of ethylene glycol is shown as due to formation of carbonaceous deposits that protect the surface from hydroxylation. *In situ* ATR-IR is a promising technique to investigate catalysis of APR.

6. Acknowledgements

Authors acknowledge CatchBio for the funding of the project (project number 053.70.002). Authors thank Ing. Louise Vrieling for performing XRF and BET measurements and Ing B. Geerdink for setting up the experimental unit including the ATR-IR cell.

7. References

1. Rahimpour, M.R., M. Jafari, and D. Iranshahi, *Progress in catalytic naphtha reforming process: A review*. Applied Energy, 2013. **109**(0): p. 79-93.
2. Azzam, K.G., I.V. Babich, K. Seshan, and L. Lefferts, *Bifunctional catalysts for single-stage water-gas shift reaction in fuel cell applications. Part 1. Effect of the support on the reaction sequence*. Journal of Catalysis, 2007. **251**(1): p. 153-162.
3. Azzam, K.G., I.V. Babich, K. Seshan, and L. Lefferts, *A bifunctional catalyst for the single-stage water-gas shift reaction in fuel cell applications. Part 2. Roles of the support and promoter on catalyst activity and stability*. Journal of Catalysis, 2007. **251**(1): p. 163-171.

4. Tsukada, T., H. Segawa, A. Yasumori, and K. Okada, *Crystallinity of boehmite and its effect on the phase transition temperature of alumina*. Journal of Materials Chemistry, 1999. **9**(2): p. 549-553.
5. Krokidis, X., P. Raybaud, A.E. Gobichon, B. Rebours, P. Euzen, and H. Toulhoat, *Theoretical study of the dehydration process of boehmite to γ -alumina*. Journal of Physical Chemistry B, 2001. **105**(22): p. 5121-5130.
6. Krishna Priya, G., P. Padmaja, K.G.K. Warriar, A.D. Damodaran, and G. Aruldas, *Dehydroxylation and high temperature phase formation in sol-gel boehmite characterized by Fourier transform infrared spectroscopy*. Journal of Materials Science Letters, 1997. **16**(19): p. 1584-1587.
7. Digne, M., P. Sautet, P. Raybaud, P. Euzen, and H. Toulhoat, *Use of DFT to achieve a rational understanding of acid–basic properties of γ -alumina surfaces*. Journal of Catalysis, 2004. **226**(1): p. 54-68.
8. Doudah, A., P. Marécot, and J. Barbier, *Toward a better understanding of the stability of supported platinum catalysts in aqueous phase under hydrogen atmosphere at room temperature*. Applied Catalysis A: General, 2002. **225**(1–2): p. 11-19.
9. Besson, M. and P. Gallezot, *Deactivation of metal catalysts in liquid phase organic reactions*. Catalysis Today, 2003. **81**(4): p. 547-559.
10. El Doukkali, M., A. Iriondo, J.F. Cambra, I. Gandarias, L. Jalowiecki-Duhamel, F. Dumeignil, and P.L. Arias, *Deactivation study of the Pt and/or Ni-based γ -Al₂O₃ catalysts used in the aqueous phase reforming of glycerol for H₂ production*. Applied Catalysis A: General, 2014. **472**(0): p. 80-91.
11. Ram, S., *Infrared spectral study of molecular vibrations in amorphous, nanocrystalline and AlO(OH)·xH₂O bulk crystals*. Infrared Physics & Technology, 2001. **42**(6): p. 547-560.
12. De Vlieger, D.J.M., B.L. Mojet, L. Lefferts, and K. Seshan, *Aqueous Phase Reforming of ethylene glycol - Role of intermediates in catalyst performance*. Journal of Catalysis, 2012. **292**: p. 239-245.
13. Li, H., Y. Xu, C. Gao, and Y. Zhao, *Structural and textural evolution of Ni/ γ -Al₂O₃ catalyst under hydrothermal conditions*. Catalysis Today, 2010. **158**(3-4): p. 475-480.
14. Luo, N., X. Fu, F. Cao, T. Xiao, and P.P. Edwards, *Glycerol aqueous phase reforming for hydrogen generation over Pt catalyst - Effect of catalyst composition and reaction conditions*. Fuel, 2008. **87**(17-18): p. 3483-3489.
15. Koichumanova, K., A.K.K. Vikla, D.J.M. de Vlieger, K. Seshan, B.L. Mojet, and L. Lefferts, *Towards Stable Catalysts for Aqueous Phase Conversion of Ethylene Glycol for Renewable Hydrogen*. Chemsuschem, 2013. **6**(9): p. 1717-1723.
16. Ciftci, A., B. Peng, A. Jentys, J.A. Lercher, and E.J.M. Hensen, *Support effects in the aqueous phase reforming of glycerol over supported platinum catalysts*. Applied Catalysis A: General, 2012. **431-432**: p. 113-119.
17. MacDonald, D.D. and P. Butler, *The thermodynamics of the aluminium-water system at elevated temperatures*. Corrosion Science, 1973. **13**(4): p. 259-274.
18. Carrier, X., E. Marceau, J.-F. Lambert, and M. Che, *Transformations of γ -alumina in aqueous suspensions: 1. Alumina chemical weathering studied as a function of pH*. Journal of Colloid and Interface Science, 2007. **308**(2): p. 429-437.
19. Lefèvre, G., M. Duc, P. Lepeut, R. Caplain, and M. Fédoroff, *Hydration of γ -alumina in water and its effects on surface reactivity*. Langmuir, 2002. **18**(20): p. 7530-7537.
20. Dyer, C., P.J. Hendra, W. Forsling, and M. Ranheimer, *Surface hydration of aqueous γ -Al₂O₃ studied by Fourier transform Raman and infrared spectroscopy-I. Initial results*. Spectrochimica Acta Part A: Molecular Spectroscopy, 1993. **49**(5-6): p. 691-705.

21. Eng, P.J., T.P. Trainor, G.E. Brown Jr, G.A. Waychunas, M. Newville, S.R. Sutton, and M.L. Rivers, *Structure of the hydrated α -Al₂O₃ (0001) surface*. Science, 2000. **288**(5468): p. 1029-1033.
22. Ravenelle, R.M., J.R. Copeland, W.G. Kim, J.C. Crittenden, and C. Sievers, *Structural Changes of γ -Al₂O₃-Supported Catalysts in Hot Liquid Water*. ACS Catalysis, 2011. **1**(5): p. 552-561.
23. Ravenelle, R.M., J.R. Copeland, A.H. Van Pelt, J.C. Crittenden, and C. Sievers, *Stability of Pt/ γ -Al₂O₃ catalysts in model biomass solutions*. Topics in Catalysis, 2012. **55**(3-4): p. 162-174.
24. Jongerius, A.L., J.R. Copeland, G.S. Foo, J.P. Hofmann, P.C.A. Bruijninx, C. Sievers, and B.M. Weckhuysen, *Stability of Pt/ γ -Al₂O₃ catalysts in lignin and lignin model compound solutions under liquid phase reforming reaction conditions*. ACS Catalysis, 2013. **3**(3): p. 464-473.
25. Tunega, D., H. Pasalic, M.H. Gerzabek, and H. Lischka, *Theoretical study of structural, mechanical and spectroscopic properties of boehmite (γ -AlOOH)*. J Phys Condens Matter, 2011. **23**(40): p. 404201.
26. Dickie, S.A. and A.J. McQuillan, *In-situ infrared spectroscopic studies of adsorption processes on boehmite particle films: Exchange of surface hydroxyl groups observed upon chelation by acetylacetone*. Langmuir, 2004. **20**(26): p. 11630-11636.
27. Raybaud, P., M. Digne, R. Iftimie, W. Wellens, P. Euzen, and H. Toulhoat, *Morphology and Surface Properties of Boehmite (γ -AlOOH): A Density Functional Theory Study*. Journal of Catalysis, 2001. **201**(2): p. 236-246.
28. Kiss, A.B., G. Keresztury, and L. Farkas, *Raman and i.r. spectra and structure of boehmite (γ -AlOOH). Evidence for the recently discarded D172h space group*. Spectrochimica Acta Part A: Molecular Spectroscopy, 1980. **36**(7): p. 653-658.
29. Ruan, H.D., R.L. Frost, and J.T. Klopogge, *Comparison of Raman spectra in characterizing gibbsite, bayerite, diaspore and boehmite*. Journal of Raman Spectroscopy, 2001. **32**(9): p. 745-750.
30. Decanio, E.C., J.C. Edwards, and J.W. Bruno, *Solid-State 1H MAS NMR Characterization of γ -Alumina and Modified γ -Aluminas*. Journal of Catalysis, 1994. **148**(1): p. 76-83.
31. Jacobsen, C.J.H., N.Y. Topsoe, H. Topsoe, L. Kellberg, and H.J. Jakobsen, *Quantitative 1H MAS NMR Studies of Structurally Different OH Surface Groups on η -Al₂O₃ and Mol-/ η -Al₂O₃ Catalysts*. Journal of Catalysis, 1995. **154**(1): p. 65-68.
32. Knoezinger, H. and P. Ratnasamy, *CATALYTIC ALUMINAS: SURFACE MODELS AND CHARACTERIZATION OF SURFACE SITES*. Catalysis Reviews-Science and Engineering, 1978. **17**(1): p. 31-70.
33. Absi-Halabi, M., A. Stanislaus, and H. Al-Zaid, *Effect of acidic and basic vapors on pore size distribution of alumina under hydrothermal conditions*. Applied Catalysis A, General, 1993. **101**(1): p. 117-128.
34. Stanislaus, A., K. Al-Dolama, and M. Absi-Halabi, *Preparation of a large pore alumina-based HDM catalyst by hydrothermal treatment and studies on pore enlargement mechanism*. Journal of Molecular Catalysis A: Chemical, 2002. **181**(1-2): p. 33-39.

Calculations of penetration depth of IR radiation for all samples

The penetration depth of evanescent wave during total internal reflection process is determined according to the **Equation 1**:

$$d_p = \frac{\lambda}{2\pi n_1 \sqrt{(\sin^2 \theta - (\frac{n_2}{n_1})^2)}} \quad (\text{Eq. 1})$$

where λ – wavelength, θ – angle of incidence (45°), n_1 , n_2 – refractive indices of ZnSe and porous sample, respectively. Since the samples are porous and the pores are filled with water, calculation of refractive index becomes more complex. It is known that enhanced porosity significantly decreases the refractive index of material [1]. Refractive index of a porous material is calculated according to the **Equation 2**:

$$n_{eff} = \sqrt{(1 - \varphi)n_c^2 + \varphi n_d^2} \quad (\text{Eq. 2})$$

where φ – porosity, n_c , n_d – refractive indices of solid and water, respectively.

Thickness of the layer was estimated based on sample weight and density of alumina assuming that the layer is uniform along the length of the IRE.

Table S1. Calculated properties of the sample layers.

Sample	Sample loading, mg	Depth of penetration, μm	Estimated layer thickness, μm
$\gamma\text{-Al}_2\text{O}_3$	11.8	0.82	3.0
1,5% wt. Pt/ $\gamma\text{-Al}_2\text{O}_3$	10.0	0.82	2.6
AlO(OH)	24.1	0.98	6.2
H ₂ O, no catalyst	-	0.73	-

ATR-IR spectra – complex infrared bands

ATR-IR spectra of Pt/ Al_2O_3 and Al_2O_3 samples in water contain not only peaks of water stretching and deformation vibrations ($3200\text{-}3600$ and 1640 cm^{-1} , respectively), and stretching and deformation vibrations of AlO(OH) (3324 , 3304 , 1064 cm^{-1}) (**Figure 3**), but also complex bands derived from IRE. This complex signal increases with temperature and disappears completely when IRE is cooled down to room temperature after experiment. The origin of this bands is not completely understood yet. Heating and cooling of the bare IRE in water results in similar behavior of these bands.

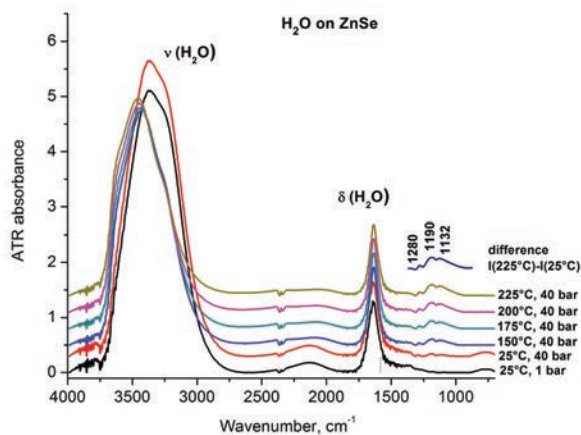


Figure S1. ATR-IR spectra of H₂O on bare ZnSe at 25°C, 40bar and 150-225°C, 40 bar.

Moreover, same phenomenon was observed when IRE was heated in *n*-dodecane (**Figure S2**). *n*-dodecane is a high boiling point liquid (214°C), thus no pressure is needed to keep it in a liquid state unlike water. Similarity of difference spectra on **Figure S1** and **S2** allows to conclude that these complex bands are not related to vibrational bands of liquid or solid material covering IR element.

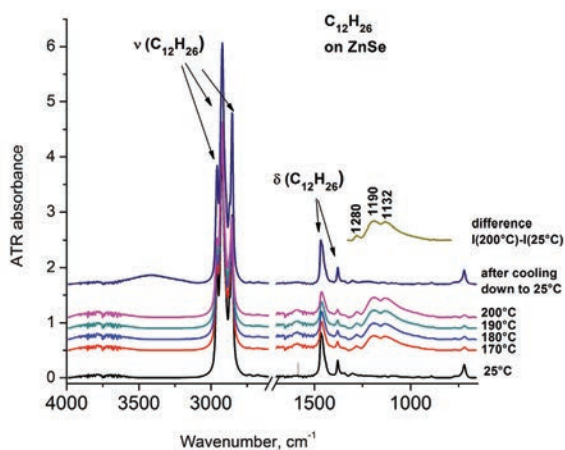


Figure S2. ATR-IR spectra of *n*-dodecane (*n*-C₁₂H₂₆) on bare ZnSe at 25°C, 1 bar and 170-200°C, 1 bar.

We attribute these bands to effect of temperature on ZnSe material. Temperature generally effects refractive index of the optical material, which can cause distortions in total reflection phenomenon. Interestingly, phonon vibrations of ZnSe usually appear at frequencies well below 1000 cm⁻¹ [2]. This phenomenon is yet to be understood.

References

1. Braun, M.M. and L. Pilon, *Effective optical properties of non-absorbing nanoporous thin films*. Thin Solid Films, 2006. **496**(2): p. 505-514.
2. Mitra, S.S., Phonon assignments in ZnSe and GaSb and some regularities in the phonon frequencies of zincblende-type semiconductors. Physical Review, 1963. **132**(3): p. 986-991.

Chapter 5

In situ ATR-IR studies in aqueous phase reforming of hydroxyacetone on Pt/ZrO₂ and Pt/AlO(OH) catalysts: the role of aldol condensation

In situ Attenuated Total Reflection Infrared (ATR-IR) spectroscopy was used to study Aqueous Phase Reforming of hydroxyacetone on Pt/AlO(OH) and Pt/ZrO₂ catalysts at 230 °C/ 30 bar. Formation of strongly adsorbed aldol condensation products were observed on the surface of Pt/ZrO₂ and ZrO₂ in contrast to Pt/AlO(OH) and AlO(OH). Peak assignments were supported by DFT calculations of the theoretical IR spectra of the condensation products in vacuum and in the presence of water. Aldol condensation of hydroxyacetone leading to compounds with high molecular weight with unsaturated bonds was suggested as a first step in coke formation. Amount and type of coke deposits determined by elemental analysis and TPO analysis showed that coke with low oxidation temperatures was deposited mostly on the surface of the ZrO₂ support. Surprisingly, no adsorbed CO was observed in the spectra, suggesting that adsorbed CO is not involved in the rate-determining step in APR of hydroxyacetone.

1. Introduction

Depletion of fossil energy resources have given rise to large number of investigations on development processes based on alternative energy resources such as biomass, solar and wind energy. Biomass pyrolysis is one of the promising processes for production of bio-oil, an alternative to crude oil, which can be further used for the production of fuels and chemicals. The aqueous phase, containing up to 20% of different organic compounds, is a by-product of biomass pyrolysis, which is currently considered a waste.

Aqueous phase reforming (APR) process was suggested [1, 2] for utilization of such streams allowing the production of hydrogen or alkanes at milder temperatures as compared to steam reforming (SR). There is no need for evaporation of water, which saves on energy usage, and the advantage of the process conditions (150-300 °C, up to 350 bar) favoring Water Gas Shift (WGS) reaction, which helps maximize hydrogen, makes the process attractive. Pt/ γ -Al₂O₃ catalyst has been used as a benchmark catalyst in APR of various oxygenates containing more than one carbon atom, *e.g.*, glycerol, sorbitol, acetic acid, acetone, due to ability of Pt to cleave C-C bonds. This cleavage leads to the formation of C₁ species, which are the intermediate species for hydrogen or methane [3, 4]. However, hot compressed water conditions used in APR lead to transformation of alumina support into a hydrated phase, known as boehmite, resulting in catalyst deactivation [5-7]. Thus, hydrothermally stable supports such as carbon [8-10], zirconia or boehmite are preferred as catalyst supports. It has been shown that Pt/AlO(OH) catalyst is active in APR of ethylene glycol with an appreciably high selectivity to hydrogen [6].

The majority of APR studies use alcohols (*e.g.*, methanol, ethanol) or polyols (glycerol, sorbitol) as model compounds, however, the aqueous phase of bio-oil also contains large amounts of organic acids, aldehydes and ketones. Hydroxyacetone (1-hydroxy-2-propanone or acetol) is a component present in significant concentration (3-8 wt. %) [11, 12] in aqueous phase of bio-oil. The APR of hydroxyacetone has not yet been studied, particularly using ZrO₂ and/or AlO(OH) supported Pt catalysts. However, few studies are available on SR of bio-oil derived light oxygenates such as hydroxyacetone, acetic acid, furfural, 1-propanol, *n*-butanol, propanal and acetone [13-18] using base metal catalysts. SR of hydroxyacetone using Ni-Al catalyst was reported [14-16] at temperatures between 450 and 750 °C, showing highest activity at 650 °C and the highest Ni content. Compared to *n*-butanol and acetic acid hydroxyacetone is easier to gasify. Trane-Rastrup *et al.* [13] studied SR of light oxygenates on Ni/MgAl₂O₄ catalyst at temperatures between 400 and 700 °C, concluding that yield of hydrogen and conversion increased with temperature and yield of by-products decreased with temperature. SR of hydroxyacetone at lower temperatures (<600 °C) resulted in the formation of oxygenated by-products, such as, butanediol, 2,5-hexanediol, substituted

cyclopentanedione and furanones, suggesting that condensation reactions leading to larger compounds take place parallel to C-C bond breaking leading to smaller compounds like CO_x and CH₄ [13].

Kinetic studies of APR of hydroxyacetone using Pt/ZrO₂ and Pt/AlO(OH) were reported by Vikla *et al.*, from our group earlier [19]. Deactivation of both catalysts during the reaction was observed. Pt sintering and coke deposition were suggested as the main reasons for catalyst deactivation. In general, spectroscopic investigation of the reaction intermediates and products is likely to provide useful information in understanding the reaction sequences. *In situ* ATR-IR spectroscopy was reported as a promising tool for studies in hot compressed water [6, 7], since it limits the contribution of water to the IR spectra, and helped to reveal identity of the surface species adsorbed on the catalyst. The development of the technique for the applications under high temperature / pressure conditions allows us to use it during APR of hydroxyacetone at 230 °C/30 bar to gain information about reaction pathways leading to formation of desired products or formation of coke.

In this study, the adsorption of hydroxyacetone on Pt/ZrO₂ and Pt/AlO(OH) catalysts under APR conditions, *i.e.* 230 °C/ 30 bar, is studied using *in situ* ATR-IR spectroscopy. The goal of the investigation is to detect surface species formed as a result of hydroxyacetone adsorption and further transformations into desired or undesired products. Correlation between the structure of the surface species observed by ATR-IR and a possible route of catalyst deactivation [19] will be made.

2. Experimental

2.1 Catalyst preparation

Catalysts were prepared by wet impregnation of commercial monoclinic ZrO₂ (RC100, Gimex Technisch Keramik B.V.) and boehmite (AlO(OH)) supports, the latter made by subjecting γ -alumina (BASF) to hydrothermal conditions, *i.e.*, 200 °C, 14 bar for 10 hours in an autoclave. H₂PtCl₆ · 6H₂O (Alfa Aesar) was used as the platinum precursor. Supports (300-600 μ m fraction) were added to an aqueous solution of the precursor (H₂O to catalyst weight ratio of 1,8) followed by evaporation of water in a rotary evaporator under vacuum at 100 °C. Samples were then reduced in H₂ atmosphere (H₂ 100 mL/min, N₂ 100 mL/min) at 100 °C for 5 h and calcined in air (200 mL/min) at 350C (5 °C/min) for 15h.

2.2 Catalyst characterization

The surface areas of the catalysts were measured by N₂ physisorption using the BET adsorption isotherm (Micromeritics, ASAP 2400). The Pt dispersion was established by H₂ pulse chemisorption at room temperature (Micromeritics, Chemisorb

2750), after samples were reduced in pure H₂ at 200 °C for 1 h. TEM microscopy (Philips 300kV, equipped with energy-dispersive X-Ray spectroscopy) was used to determine the Pt particle size distribution of fresh and spent catalysts. Approximately 250 particles across 10 different spots on each sample were measured to give a weighted average size.

The elemental composition was determined using a Perkin-Elmer elemental analyser (Thermo Scientific Flash 2000). Approximately 3-4 mg of sample was used for the analysis. Concentrations of C, H and N were calculated based on amounts of water, CO₂ and N₂ evolved from decomposition of the sample in 35 vol. % O₂/Ar flow (390 mL/min) at 900 °C. Acetanilide was used for calibration, and oxygen content was calculated as rest.

Temperature Programmed Oxidation was used to determine the type of coke deposits on the spent catalysts. Samples (3-4 mg) were pretreated in He (25 mL/min) at 150 °C for 30 min. After cooling down to 25 °C the samples were oxidized in 5 vol. % O₂/He mixture (25 mL/min) during heating to 600 °C with a heating rate of 5 °C/min. An online methanizer (Model 110 Chassis, SRI Instruments Europe GmbH) was used to convert CO and CO₂ to methane using a Ni catalyst. The amount of methane formed was quantified with an FID detector. Al₂(CO₃)₃ was used for calibration of the FID.

2.3 Acidity measured by NH₃ TPD and Pyridine adsorption IR spectroscopy

Fourier transform infrared spectroscopy (FTIR) of adsorbed pyridine was conducted in a Bruker IFS 66 spectrometer equipped with HgCdTe detector (4000-650 cm⁻¹, 2 cm⁻¹ resolution, 32 scans). Prior to pyridine adsorption at room temperature, self-supporting wafers of Pt/ZrO₂ and Pt/AlO(OH) (5 ton/cm², 20 mg, 1 cm²) were degassed under vacuum (10⁻³ mbar) for 2 h at 200 °C. Gaseous and weakly adsorbed pyridine was removed by evacuation for 30 min at 25 °C. To evaluate the adsorption strength of chemisorbed pyridine, catalysts were subsequently treated at 225 °C for 60 min.

Temperature-programmed desorption of ammonia (NH₃-TPD) was performed in a Autochem 2910 II instrument from Micromeritics. The samples were pretreated in He (50 cm³/min) at 200 °C for 1 h. NH₃ adsorption was performed at room temperature for 30 min, followed by removal of physisorbed NH₃ in He flow for 1 h. Desorption of NH₃ was monitored in the range of 20-600 °C using a heating rate of 10 °C/min.

2.4 *In situ* ATR-IR spectroscopy

In situ ATR-IR experiments were performed using a setup consisting of a commercial ATR-IR Tunnel cell (Axiom) modified for high temperature and pressure conditions, which was mounted in a sample chamber of an FTIR spectroscopy bench (Bruker, Tensor 27) equipped with liquid-nitrogen cooled mercury-cadmium-telluride

detector. Water used for pretreatment procedures was saturated with hydrogen, oxygen or helium in bubble saturator bottles, whereas hydroxyacetone solution was degassed with helium. Liquids were fed into the system using an HPLC pump (Dionex P680) and pressure was regulated with a back-pressure regulator. The liquid was preheated to the experimental temperature in the preheater tubing before entering the cell, and the liquid leaving the reactor was cooled with water in a tubular heat exchanger.

The cylindrical internal reflection element (IRE, ZnSe rod, diameter 0.25 inch, length 3.25 inch) was spray-coated with a catalyst slurry (0.150 g in 25 mL of isopropanol, ball-milled for 6 min) according to a home-developed spray-coating technique [6, 20]. The sample was then carefully placed inside the cell using O-rings (Kalrez 7075) and dried at 150 °C in He (25 mL/min) for 1.5 hour.

Spectra were recorded every minute in the spectral range between 4000 and 650 cm^{-1} with a resolution of 4 cm^{-1} averaging of 139 scans. The spectrum in He (25 mL/min) (average of 256 scans) of catalyst/support layer was used as background. Penetration depths of IR light were calculated for Pt/AlO(OH), Pt/ZrO₂, AlO(OH) and ZrO₂ according to **Equation 3** in **Chapter 2**, showing no difference between the samples with and without Pt. Penetration depths for Pt/AlO(OH) and Pt/ZrO₂ were 0.89 and 0.77 μm , respectively, showing only 15% difference between two samples. Thus, small variations in the IR intensity in spectra of the two samples should be expected.

For all ATR-IR experiments, the cell was first filled with water (2 mL/min), and the sample was subjected to a cleaning procedure adopted from literature [21]. In our experiments this procedure consisted of alternating flows of hydrogen-, oxygen- and helium-saturated water (2 mL/min, 30 min each flow) at ambient conditions. Hydrogen-saturated water was used in the final treatment in order to leave the sample in reduced state. Finally, water was flown over the sample again and pressure was increased to the desired experimental pressure (20 or 30 bar). After that, the cell and the preheater lines were heated to the desired experiment temperature (100 °C or 230 °C) and a spectrum of water was collected. The flow was then switched to the hydroxyacetone solution (2.5 wt. %, 0.8 mL/min) with simultaneous acquisition of ATR-IR spectra for 60 min. Further, the flow was switched back to water (0.8 mL/min) and ATR-IR spectra were collected for another hour.

For CO adsorption experiments, water saturated with CO (1 bar) at room temperature was flown over the sample at room temperature and at 230 °C, 30 bar. A pretreatment and experimental procedure as described above was applied.

2.5 ATR-IR data processing

In situ ATR-IR spectra were first pre-processed (subtraction of water and catalyst spectrum, baseline correction) using OPUS software provided together with the Bruker IR spectrometer. Water and catalyst subtraction was performed for all spectra using the respective spectrum of water at the temperature of the experiment. Baseline correction

was done for all spectra using rubber-band correction method. Deconvolution of the spectra was performed using Matlab software. The spectra were fitted using Gaussian peak shapes with fixed peak positions assigned to specific relevant species. However, minor peaks present in the spectral range, but not relevant to hydroxyacetone reaction, have to be included to obtain good quality fit.

2.6 DFT calculations of IR spectra

To support assignments of the IR peaks observed during the experiments, IR spectra of hydroxyacetone, its enols and products of aldol condensation of hydroxyacetone were calculated in vacuum and in the presence of water. All calculations have been performed using Density Functional Theory with the Becke three-parameters (B3LYP) exchange-correlation functional using the Gaussian 09 program[22]. The geometry of all the investigated components has been optimized by employing the correlation consistent polarized valence triple zeta (cc-pVTZ) basis set and the same has been used to calculate harmonic vibrational frequencies.

In order to achieve a more reliable comparison with the experimental spectra, anharmonicity has been taken into account by the following procedure. Since the direct calculation of the anharmonic frequencies of medium sized molecules at the B3LYP/cc-pVTZ level is a demanding task, they have been evaluated with the less extended cc-pVDZ basis set, using optimized geometries at the same level. Anharmonicity corrections have been obtained as the differences between the harmonic and fundamental frequencies, and these corrections were then applied to the harmonic cc-pVTZ frequencies. The reliability of these composite TZ+DZ anharmonic frequency calculations has been checked by comparing them with the entirely TZ anharmonics calculated for the smaller molecules investigated in this work (hydroxyacetone in all its conformations and tautomers) in the frequency range 4000 - 400 cm^{-1} . The results showed that while the composite TZ+DZ anharmonics represent a good improvement over the purely DZ ones and they have a mean absolute percent deviation of only 0.9% with respect to the full TZ fundamentals. Furthermore, a comparison with the experimental data for hydroxyacetone in its most stable conformation yields the following results for the root mean square deviations: $\text{RMSD}(\text{TZ}) = 20$, $\text{RMSD}(\text{DZ}) = 34$, $\text{RMSD}(\text{TZ}+\text{DZ}) = 24 \text{ cm}^{-1}$, which clearly demonstrates excellent reliability of the composite approach for the hydroxyacetone spectrum. Therefore, it was assumed that the TZ+DZ protocol worked well also for the larger molecular systems in this study.

3. Results

3.1 Catalyst characterization

Table 1 shows the characteristics of the two catalysts used in the study. Pt/AlO(OH) had BET surface area of 41 m²/g and Pt particles of 5 nm and Pt/ZrO₂ had BET surface area of 94 m²/g and Pt particles of 1.8 nm. Pt loading for both catalysts was around 1.1 wt. %. The average Pt particle size was determined from TEM micrographs, as well as from H₂ chemisorption. The very small Pt particles in Pt/ZrO₂ could not be detected in TEM because of the limited contrast of Pt with ZrO₂. Details of the Pt size distribution and TEM images can be found in [19]. ZrO₂ and AlO(OH) without Pt were also studied, these supports had surface areas similar to their respective Pt catalysts.

Table 1. Characteristics of fresh catalysts.

Sample	Pt loading, wt. %	BET surface area, m ² /g	Mean Pt particle size (TEM), nm	Mean Pt particle size (H ₂ chemisorption), nm
Pt/AlO(OH)	1.1	41	5.1	4.9
Pt/ZrO ₂	1.1	94	n.a.*	1.8
* not available				

3.2 In situ ATR-IR results

3.2.1 ATR-IR spectra of hydroxyacetone over bare ZnSe

Figure 1 shows water subtracted *in situ* ATR-IR spectra of 2.5 wt.% hydroxyacetone flown over a bare ZnSe element at 25 °C, 1 bar and at 230 °C, 30 bar. During filling of the cell with the hydroxyacetone solution, the intensity of IR peaks increased gradually and reached saturation within a few minutes. Observed peaks were assigned to different vibrational modes of hydroxyacetone based on literature [23, 24]: C=O stretching (1722 cm⁻¹), CO-C-OH coupling (1085 cm⁻¹), C-C stretching (1191 cm⁻¹), H-C-H bending in CH₃ (1427 cm⁻¹), symmetric CH₃ bending (1363 cm⁻¹), C-OH bending (1236 cm⁻¹), CH₂ deformation coupled with CO (1085 cm⁻¹). The peak at 1635 cm⁻¹ is an artifact due to water subtraction and positive peaks between 1600 and 1500 cm⁻¹ are caused by increased noise level during the experiment due to moisture leakage around the cell. No other peaks other than those for hydroxyacetone were observed.

Spectra of hydroxyacetone without a catalyst at 230 °C, 30 bar (**Figure 1b**) were slightly different compared to spectra at 25 °C. Peaks were less intense and minor shifts in peak positions were observed. Similarly, no other peaks except the peaks assigned to hydroxyacetone were observed.

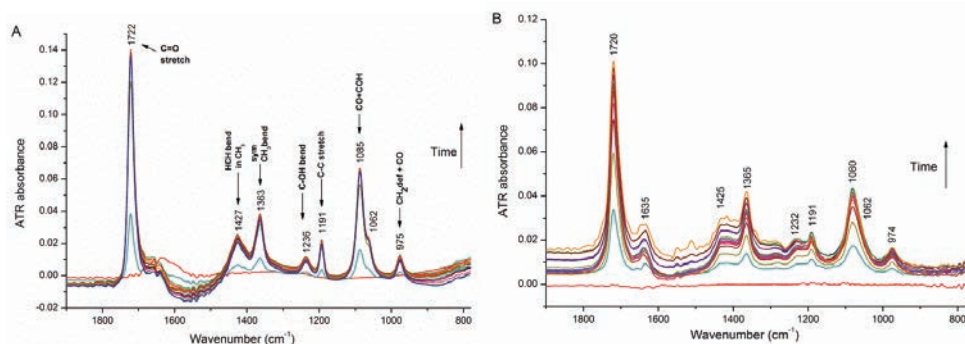


Figure 1. Water subtracted *in situ* ATR-IR spectra of hydroxyacetone over bare ZnSe without a catalyst at (a) 25 °C, 1 bar and (b) at 230 °C, 30 bar during 60 min. Spectra with time difference of 1 min are presented during the first 10 min, further spectra have a time difference of 10 min.

3.2.2 Hydroxyacetone adsorption on Pt/ZrO₂ and Pt/AlO(OH)

Figure 2 shows water subtracted *in situ* ATR-IR spectra of hydroxyacetone adsorption on Pt/ZrO₂, ZrO₂, Pt/AlO(OH) and AlO(OH) after 60 min. Spectrum in the absence of the catalyst at 25 °C, is also shown, which is identical to the final spectrum in **Figure 1a**. Peaks in the spectra of hydroxyacetone adsorption on Pt/AlO(OH) and AlO(OH) were almost the same as on bare ZnSe, except for peaks at 1583 cm⁻¹ and in the 1150-1000 cm⁻¹ region. Boehmite has an additional IR peak at 1060 cm⁻¹, which was assigned to OH deformation vibrations of structural hydroxyls [7, 25-27]. This made it difficult to decide if any peaks of adsorbate species were present in the spectra next to hydroxyacetone.

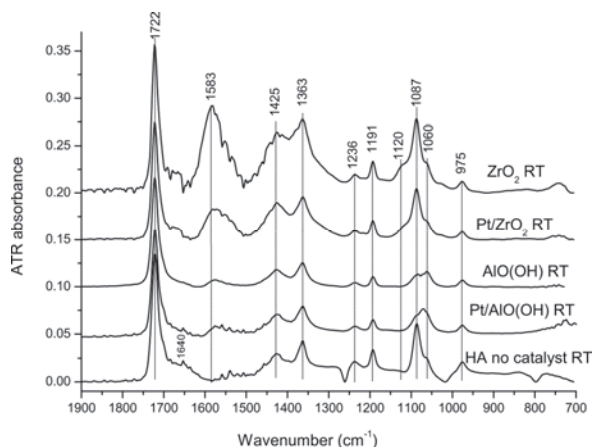


Figure 2. Water subtracted *in situ* ATR-IR spectra of hydroxyacetone adsorption on Pt/ZrO₂, ZrO₂, Pt/AlO(OH), AlO(OH) at RT, 1 bar after 60 min.

The two new peaks at 1583 and 1120 cm⁻¹ appeared on both Pt/ZrO₂ and ZrO₂ samples. The peak positions observed on both ZrO₂ and Pt/ZrO₂ were identical, but the

intensity was significantly higher on ZrO₂. This indicated that same type of adsorbates were formed on the surface of zirconia for both samples. The ratio between intensities of 1583 cm⁻¹ and intensities of 1722 cm⁻¹ was much higher for ZrO₂-based samples, than for AlO(OH)-based samples, indicating that higher amounts of adsorbates were formed on ZrO₂-based samples.

Hydroxyacetone adsorption at 100 °C (**Figure S1**) resulted in appearance of peaks at 1588 cm⁻¹ for Pt/AlO(OH) and 1601 cm⁻¹ and 1120 cm⁻¹ for ZrO₂-based samples similar to the peaks observed at room temperature (**Figure 2**). Relative ratios of the intensities of the peaks at 1588/1722 and 1601/1722 were again higher for ZrO₂-based samples compared to Pt/AlO(OH).

Adsorption spectra of hydroxyacetone on Pt/ZrO₂ and Pt/AlO(OH) at 230 °C are presented in **Figure 3**. Few differences were observed when compared to spectra at RT or at 100 °C (**Figures 2 and S1**). Firstly, the 1718 cm⁻¹ peak had an asymmetrical shape with apparent shoulders at 1697 and 1679 cm⁻¹, secondly, the 1419 cm⁻¹ peak became broader. The peak at 1583 cm⁻¹ observed at RT and 100 °C also shifted to lower wavenumber of 1544 cm⁻¹. Finally, the quality of the spectra deteriorated by an increasing level of noise, which was caused by leakage of moisture around the cell inside the IR chamber.

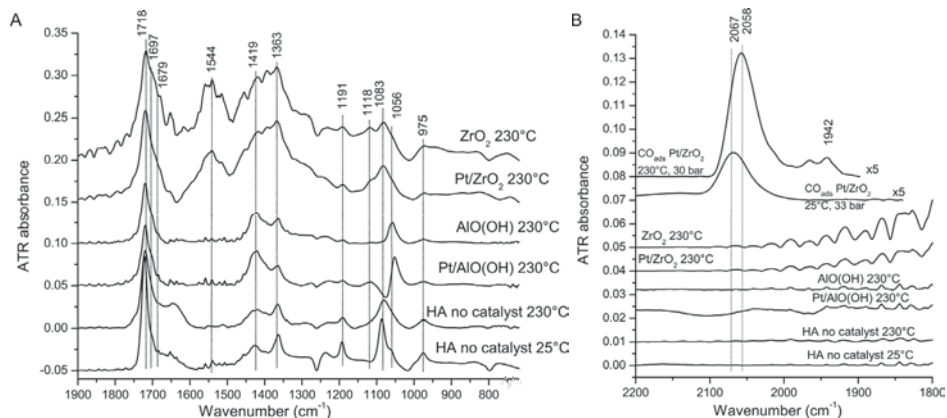


Figure 3. Water subtracted *in situ* ATR-IR spectra of hydroxyacetone adsorption on Pt/ZrO₂, ZrO₂, Pt/AlO(OH), AlO(OH) at 230 °C, 30bar after 60 min in the frequency range (a) 1900-720 cm⁻¹, (b) 2200-1800 cm⁻¹. ATR-IR adsorption spectra of CO adsorbed on Pt/ZrO₂ from CO dissolved in water at 25 °C, 33 bar and 230 °C, 30 bar after 60 min are added for comparison. Intensities of the peaks of adsorbed CO were multiplied by 5 times for clarity.

Surprisingly, adsorption on AlO(OH)-based samples at 230 °C did not show characteristic changes compared to ZrO₂-based samples (**Figure 3**). Only the shoulder at 1697 cm⁻¹ was observed, whereas no peaks were observed around 1600 cm⁻¹. Peaks at 1425 and 1365 cm⁻¹ were still well-resolved, suggesting that broadening observed for ZrO₂-based samples was due to surface chemistry on zirconia, and not due to any influence of temperature on the resolution of IR spectra.

The spectral region between 2200 and 1800 cm^{-1} , which is typical for CO adsorption on Pt, is shown in **Figure 3b**. It is clear that no adsorbed CO was observed during hydroxyacetone adsorption on both catalysts. When H_2O saturated with CO at 1 bar (26 ppm of CO, feed rate of 10^{-6} mol/min) was flown over the Pt/ ZrO_2 catalyst at the same conditions (230 °C, 33 bar), linear and bridge-bonded CO on Pt were observed at 2058 and 1942 cm^{-1} , respectively (**Figure 3b**), in agreement with literature [28]. CO adsorption at room temperature resulted in linearly bound CO on Pt at 2067 cm^{-1} with lower peak intensity compared to 230 °C. No bridge bound CO was observed during adsorption at 25 °C.

Adsorption profile of linearly adsorbed CO at 25 °C, presented as normalized intensities in **Figure 4 a**, showed an initial rapid increase and further saturation of CO signal around 60 min. After subsequent heating to 230 °C in CO/ H_2O flow, spectra were collected during 60 min while keeping the temperature constant. Intensities normalized to the initial intensity are presented in **Figure 4b**, showing decrease in intensity of the CO signal. The decrease of CO intensity at 230 °C suggests that at this temperature CO was also consumed and/or desorbed. However, together with the top two spectra in **Figure 3b** it is clear that under the conditions of APR and at 25 °C it is possible to detect adsorbed CO on Pt using ATR-IR.

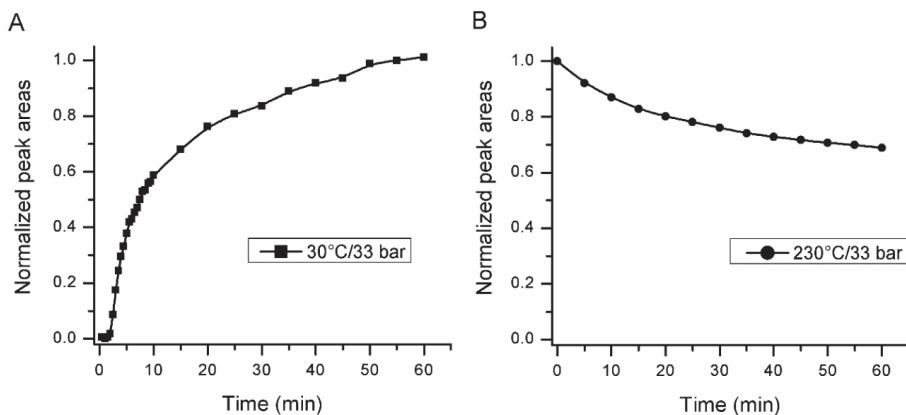


Figure 4. Normalized CO peak areas (linear CO peak 2067 and 2058 cm^{-1} at 30 °C, 33 bar and 230 °C, 33 bar, respectively) during 60 min of CO/ H_2O adsorption on Pt/ ZrO_2 .

3.2.3 Initial adsorption of hydroxyacetone on Pt/ ZrO_2 and ZrO_2

Spectra collected during the first minutes of hydroxyacetone adsorption on Pt/ ZrO_2 are presented in **Figure 5**. Similar results were also obtained for ZrO_2 (**Figure S2** in Supporting information). During the first 5 min no peaks were observed in the spectra, however between 5 and 10 min the intensities of the peaks at 1718 cm^{-1} and 1083 cm^{-1} started increasing slowly together with intensities of peaks at 1604, 1382, 1120 and 1056 cm^{-1} . After 10 min and up until 20 min peaks continued growing, with

peaks 1718 cm^{-1} and 1083 cm^{-1} growing faster than other peaks (**Figure 5**). This behavior was different when compared to the gradual increase of intensities of all peaks observed on the same samples at room temperature and $100\text{ }^{\circ}\text{C}$ (**Figures S3 and S4** in Supporting information). Interestingly, the frequency of the adsorbate peak at 1604 cm^{-1} , observed during 0-10 min, was similar to the frequency of the adsorbate observed on Pt/ZrO₂ at $100\text{ }^{\circ}\text{C}$, 20 bar (1601 cm^{-1} on **Figure S1**). Furthermore, after 20 minutes, a broad band, containing both 1604 and 1541 cm^{-1} was observed. Longer exposure to hydroxyacetone caused a further increase in the intensity of the peak at 1541 cm^{-1} , while the peak at 1604 cm^{-1} remained as a shoulder.

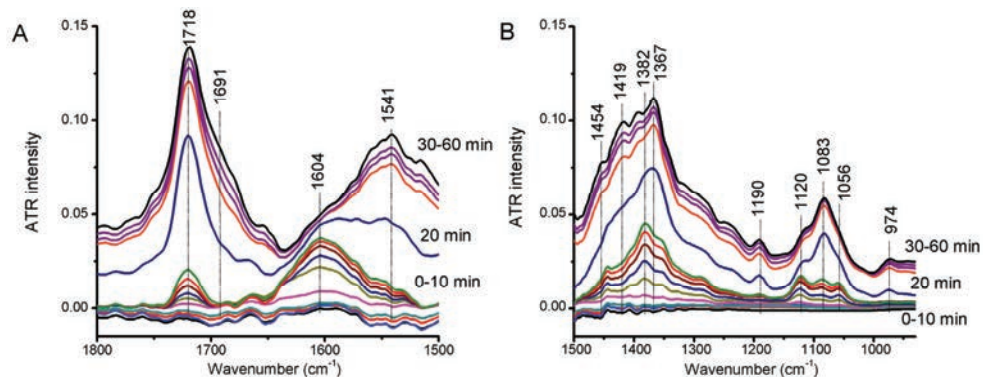


Figure 5. Time resolved water corrected *in situ* ATR-IR spectra during adsorption of hydroxyacetone on Pt/ZrO₂ at $230\text{ }^{\circ}\text{C}$, 30 bar. Spectra with time difference of 1 min are presented during the first 10 min; further spectra have the time difference of 10 min. The spectrum after 60 min is identical to the Pt/ZrO₂ spectrum in Figure 3.

3.2.4 Reactivity of adsorbates during flushing with water: ZrO₂ and Pt/ZrO₂

In order to study the adsorbates on the surface, the catalyst was flushed with water to remove hydroxyacetone in liquid phase. **Figure 6a** shows the spectra collected during flushing of the cell with water after exposure to hydroxyacetone at the same temperature. Gradual decrease in the peak intensities due to disappearance of hydroxyacetone from the cell was observed. However, there were still peaks remaining after flowing water for one hour.

There were two different types of peaks according to their disappearance rate in H₂O: fast disappearing peaks belonging to hydroxyacetone in liquid phase and slowly disappearing peaks assigned to adsorbates. A fast decrease was observed for peaks at 1718 , 1419 , 1367 , 1191 , 1083 and 975 cm^{-1} . Similar behavior was observed for the same set of peaks when hydroxyacetone was flushed from the cell with bare ZnSe at $230\text{ }^{\circ}\text{C}$, without a catalyst (**Figure 6b**). The intensities of other peaks (1691 , 1593 , 1540 , 1116 cm^{-1}) in **Figure 6a** decreased slower and even stabilized at a certain level. The fact that these peaks did not disappear after 60 min in H₂O in reactive conditions indicated that they belonged to strongly adsorbed and relatively unreactive surface species.

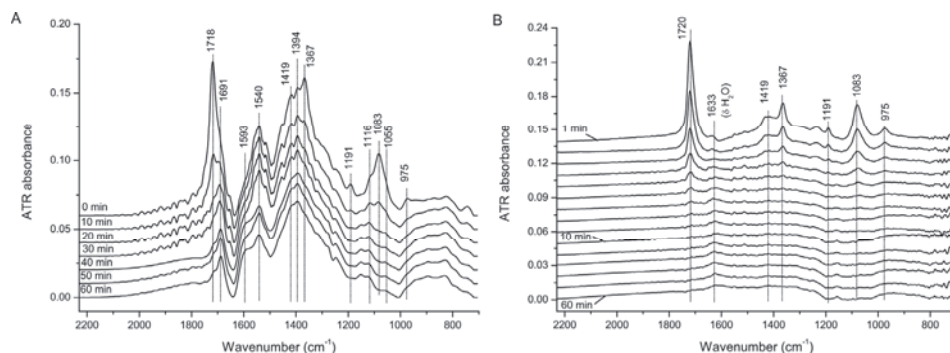


Figure 6. Time resolved water corrected *in situ* ATR-IR spectra during hydroxyacetone removal with H₂O at 230 °C, 30 bar on (a) Pt/ZrO₂, (b) bare ZnSe element. Spectra with time difference of 10 min are presented during 60 min. Spectrum at 0 min in (a) is identical to Pt/ZrO₂ spectrum on Figure 3.

Similar peaks were observed in the spectra of ZrO₂ (without Pt) after flushing with water for 60 min (**Figure S5** in Supplementary Information), suggesting that the detected species reside on the ZrO₂ surface, rather than on the Pt particles. Removal of hydroxyacetone from the cell was also studied at 25 °C and 100 °C in the absence (**Figure S6**) and in the presence of the Pt/ZrO₂ catalyst (**Figures S7 and S8**) and on Pt/AlO(OH) and AlO(OH) at 230 °C (**Figure S9**), showing similar trends as discussed above.

3.3 Acidity of supports studied by pyridine IR and TPD NH₃

FTIR spectra of pyridine adsorbed on Pt/ZrO₂ and Pt/AlO(OH) after evacuation at RT and 225 °C are shown in **Figure 7**. Spectra were collected at RT after the sample had been evacuated at the given temperatures. Peaks of higher intensity can be seen for Pt/ZrO₂ compared to Pt/AlO(OH). Intensities of all of the peaks decreased after evacuation at 225 °C. This was especially significant for Pt/AlO(OH), since most of the peaks decreased to below the noise level. Peaks were assigned based on literature [29, 30].

Results showed that Pt/ZrO₂ has Lewis acidity (LPy; 1605 and 1456 cm⁻¹) and weak Brönsted acidity (BPy; 1641 cm⁻¹), as well as Lewis basicity (LB, Py-ox₁ and Py-ox₂; 1488, 1548 cm⁻¹). Py-ox₁ and Py-ox₂ were assigned to pyridine oxidation species (Py-ox₁ to carboxylate species and Py-ox₂ to carbonaceous species) based on the observation of Zaki *et al.* [29] that these species can be formed on metal oxides due to presence of Lewis basic sites at temperatures above 100 °C. For Pt/ZrO₂, pyridine was also found in hydrogen-bonded state (HPy) according to peaks at 1593 and 1442 cm⁻¹.

After evacuation at 225 °C LPy shifted to 1608 cm⁻¹, but BPy almost disappeared suggesting the presence of weak and strong Lewis acid sites and weak Brönsted acid sites. Intensities and rates of disappearance of BPy compared to LPy suggest that Pt/ZrO₂ has more Lewis acid sites than Brönsted acid sites.

Pt/AlO(OH) has Lewis acid sites (LPy; 1616, 1492 cm^{-1})[29] and no Brønsted acidity, which is in agreement with the results of Takagaki *et al.* [31]. However, hydrogen-bonded pyridine was detected as well (HPy; 1595, 1577 and 1446 cm^{-1}). The peak shift of LPy to 1622 cm^{-1} after evacuation at 225 °C suggested that both weak and strong Lewis acid sites are present on Pt/AlO(OH). Pt/AlO(OH) had less intense peaks in all spectra compared to Pt/ZrO₂, which suggested a lower concentration of Lewis sites on Pt/AlO(OH). No Lewis base sites were detected on Pt/AlO(OH). The difference in acidity between the two catalysts is much larger than the difference in their surface areas (**Table 1**), indicating that Pt/ZrO₂ has higher surface concentration of acid and basic sites on compared to Pt/AlO(OH).

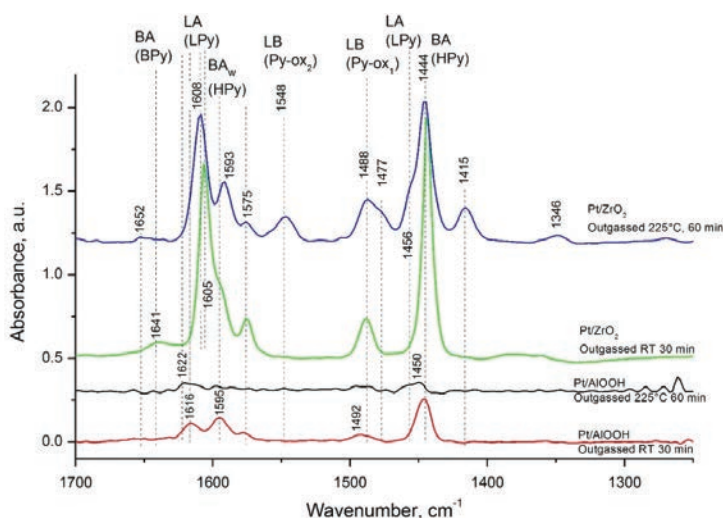


Figure 7. FTIR spectra after pyridine adsorption on Pt/ZrO₂ and Pt/AlO(OH) after evacuation at RT and 225 °C.

Spectra obtained on Pt/Al₂O₃ (**Figure S10** in Supplementary Information) were rather similar to the results on Pt/AlO(OH) in terms of peak positions and types of adsorbed pyridine, suggesting materials are similar in types of acid sites present despite the differences in Al coordination.

TPD NH₃ profile of Pt/ZrO₂ revealed two peaks at 93 °C and 329 °C (**Figure 8**). Total acidity calculated from the area under the curve was 604 mmol/g. TPD NH₃ profile of Pt/AlO(OH) showed a small peak at 97 °C and a very intense peak at about 500 °C with a shoulder at 300 °C. The peak at 500 °C was most likely due to water desorbing as a result of phase transformation of AlO(OH) into γ -Al₂O₃. This phase transfer was reported to happen at 500 °C [32-34]. The total acidity of Pt/AlO(OH) during NH₃ desorption could not be accurately calculated due to interference from H₂O in TCD signal.

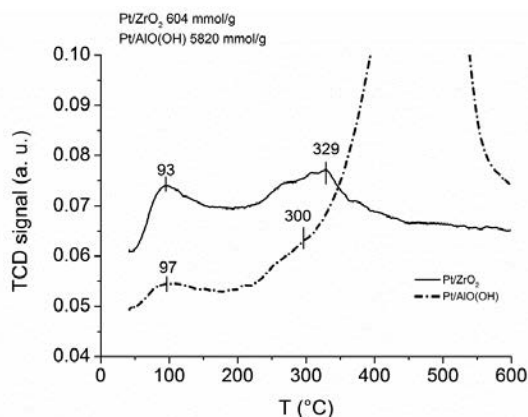


Figure 8. TPD NH_3 profiles of fresh Pt/ ZrO_2 and Pt/ $\text{AlO}(\text{OH})$.

3.4 Characterization of deactivated catalysts and supports

3.4.1 Elemental analysis of samples after ATR-IR experiments

CHN analysis was performed to quantify the coke content on catalysts and supports after hydroxyacetone adsorption in the ATR-IR cell, flushing with water and drying, as reported in experimental section. The results presented in **Table 2** showed that both Pt/ ZrO_2 and Pt/ $\text{AlO}(\text{OH})$ have a lower amount of coke compared to their respective supports. Coke content on $\text{AlO}(\text{OH})$ was 4 times higher than on Pt/ $\text{AlO}(\text{OH})$ indicating the role of Pt in removing or preventing coke formation. The amount of carbon deposited per m^2 was also significantly different, i.e. 0.11 and 0.07 $\text{mg C}/\text{m}^2$ for Pt/ ZrO_2 and Pt/ $\text{AlO}(\text{OH})$, respectively. The tendency of ZrO_2 to form more carbon deposits was therefore not just an effect of surface area.

Table 2. Elemental analysis of samples after ATR-IR experiments, including hydroxyacetone adsorption, flushing with water and drying.

Catalyst	Elemental composition, wt.%	
	C	H
Pt/ $\text{AlO}(\text{OH})$	0.27	
Pt/ ZrO_2	1.05	0.32
$\text{AlO}(\text{OH})$	0.50	
ZrO_2	1.61	0.38

3.4.2 Temperature programmed oxidation

Temperature programmed oxidation was performed for Pt/ ZrO_2 and Pt/ $\text{AlO}(\text{OH})$ samples after hydroxyacetone adsorption in the ATR-IR cell, flushing with water and drying. TPO profile (**Figure 9**) of Pt/ ZrO_2 showed one broad peak at 303 °C and small peak around 450 °C, whereas Pt/ $\text{AlO}(\text{OH})$ showed three overlapping peaks at 286, 338 and 450 °C. The higher intensity of the TPO peaks on Pt/ ZrO_2 as compared to

Pt/AlO(OH) suggested that more coke was formed on the surface of Pt/ZrO₂, in agreement with the observations based on the elemental analysis (**Table 2**).

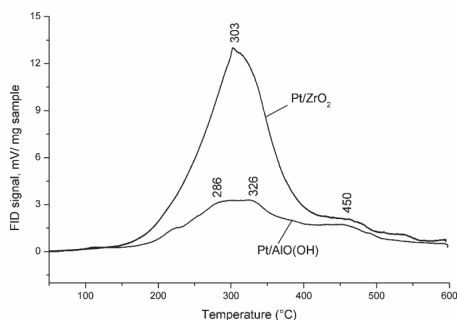


Figure 9. TPO profiles of Pt/ZrO₂ and Pt/AlO(OH) after ATR-IR experiment, which included hydroxyacetone adsorption, flushing with water and drying.

4. Discussion

4.1 Hydroxyacetone appearance in the cell

The spectra in **Figure 5** were curve fitted with peaks positioned at 1718, 1541, 1604, 1123 and 1083 cm⁻¹, and evolution of the areas of the peaks is shown in **Figure 10**. The peaks of hydroxyacetone in liquid phase (1718 and 1083 cm⁻¹) grew after an initial delay of 5 min and after 30 min peak areas stabilized.

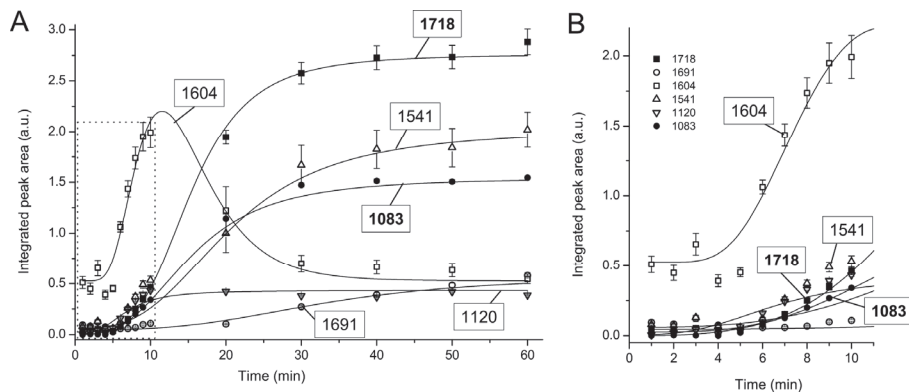


Figure 10. Integrated areas of peaks assigned to hydroxyacetone (1718 cm⁻¹ and 1083 cm⁻¹) and peaks assigned to adsorbates at 1691 cm⁻¹, 1541 cm⁻¹, 1604 cm⁻¹ and 1120 cm⁻¹ during initial adsorption of hydroxyacetone on Pt/ZrO₂ at 230 °C, 30 bar, showing time (a) 0 to 60 min, (b) zoomed to first 10 min. Error bars represent fitting error, the lines are presented to guide the eye.

Peaks assigned to adsorbates at 1120, 1604 and 1541 cm⁻¹ also appeared after 5 min and continued to increase up until 10 min. The initial delay of 5 min can be explained as the time needed for the hydroxyacetone solution to fill the volume of the feed lines and the preheater before the cell.

The peak at 1604 cm^{-1} dominated over 1541 cm^{-1} during the first 10 minutes (**Figure 10b**), however after 10 min the intensity of the 1541 cm^{-1} peak increased further, and 1604 cm^{-1} remained as a shoulder.

Interestingly, temperature had an influence on the overall spectral pattern, especially on the frequency of the adsorbate peak around 1600 cm^{-1} and the noise level of the spectra (**Figures 2, 3 and S1**). For clarity reasons these spectral changes in the case of Pt/ZrO₂ and ZrO₂ are summarized in **Figure 11**. At $25\text{ }^{\circ}\text{C}$ and $100\text{ }^{\circ}\text{C}$ only one peak at 1583 cm^{-1} was observed, however at $230\text{ }^{\circ}\text{C}$ a second peak at 1544 cm^{-1} developed. This suggests that similar types of adsorbates were formed on ZrO₂ surface at lower temperatures, while at $230\text{ }^{\circ}\text{C}$ another type of adsorbate appeared. The asymmetric shape of the carbonyl peak (1718 cm^{-1}) at $230\text{ }^{\circ}\text{C}$ compared to symmetrical shape at $25\text{ }^{\circ}\text{C}$ and $100\text{ }^{\circ}\text{C}$ as well as the broad peak around 1400 cm^{-1} supported the assumption that several types of adsorbates were present at $230\text{ }^{\circ}\text{C}$ together with hydroxyacetone in liquid.

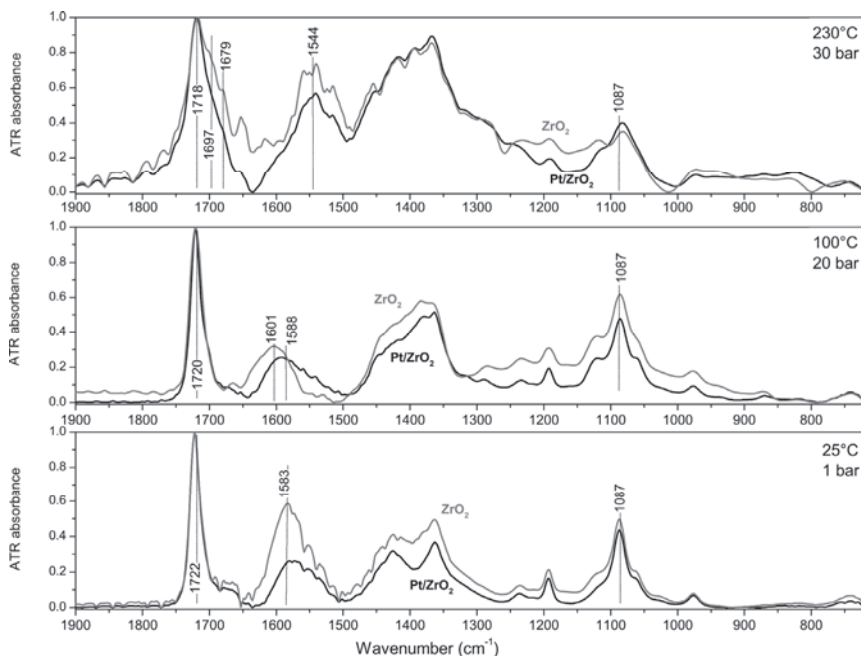


Figure 11. Water subtracted *in situ* ATR-IR spectra of hydroxyacetone adsorption on Pt/ZrO₂, ZrO₂ at (a) $25\text{ }^{\circ}\text{C}$, 1 bar, (b) $100\text{ }^{\circ}\text{C}$, 20 bar and (c) $230\text{ }^{\circ}\text{C}$, 30 bar after 60 min.

The peaks in the spectral range $1500\text{--}1300\text{ cm}^{-1}$ were better resolved and had a lower intensity at lower temperatures. The broadening and overlapping of peaks was seen as temperature was increased. However, the resolution of these peaks in case of Pt/AlO(OH) did not change (**Figure 3**), thus the peak broadening was not caused by an increase in temperature, but by presence of other types of adsorbates. Differences in relative intensities of the peaks at 1583 , 1601 and 1544 cm^{-1} compared to their

respective carbonyl peaks at 1718 cm^{-1} (**Figure 11**) indicated that more adsorbates were formed on the ZrO_2 surface at $230\text{ }^\circ\text{C}$ as compared to lower temperatures.

4.2 Hydroxyacetone washout with water

Spectra presented in **Figure 6a** were fitted with a set of peaks similar to the ones used to interpret **Figure 5** and to construct **Figure 10** during adsorption step (1718 , 1691 , 1541 , 1120 , 1057 cm^{-1}). Results of the fitting are presented in **Figure 12** for the case of Pt/ZrO_2 . Results of peak fitting for the same experiments with ZrO_2 are given in **Figure S11** Supplementary Information.

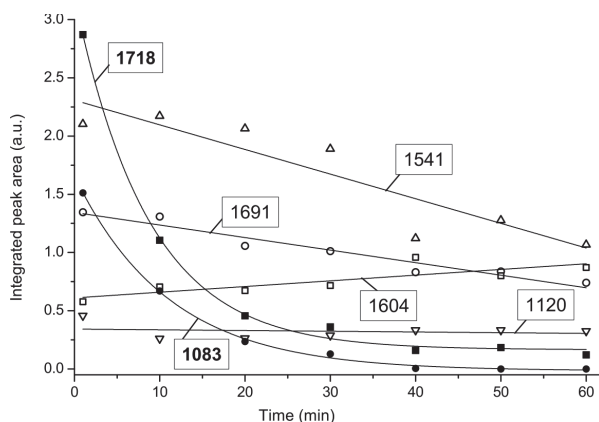


Figure 12. Integrated areas of peaks at 1718 cm^{-1} and 1083 cm^{-1} assigned to hydroxyacetone and peaks at 1691 , 1604 , 1541 and 1120 cm^{-1} assigned to adsorbates while hydroxyacetone is being washed out from the cell with Pt/ZrO_2 at $230\text{ }^\circ\text{C}$, 30 bar during 60 min . Error bars represent fitting error, the lines are presented to guide the eye.

In **Figure 12** the profile of the carbonyl peak of hydroxyacetone in the liquid phase was very different from the profile of adsorbate peaks. The fact that adsorbate peak areas decreased slightly or did not decrease at all indicated that they were strongly adsorbed on the surface. The slight decrease in peak area may be explained by consecutive reactions of adsorbates with water that can take place at these conditions, although slow desorption cannot be ruled out.

4.3 Adsorbed CO – water gas shift reaction

In **Figure 3b** no CO peak was seen in the region where linearly adsorbed CO on Pt is usually expected. To confirm the ability to detect CO using ATR-IR spectroscopy, H_2O saturated with CO at room temperature (CO concentration of 26 mg/L , feed rate of $1,9 \cdot 10^{-6}\text{ mol/min}$) was flown over Pt/ZrO_2 catalyst at $25\text{ }^\circ\text{C}$ and $230\text{ }^\circ\text{C}$. As shown in **Figure 3b** chemisorbed CO was easily observable (top two spectra). The peak position of linearly bound CO was slightly different at $25\text{ }^\circ\text{C}$ and $230\text{ }^\circ\text{C}$ and intensity of the peak was higher at $230\text{ }^\circ\text{C}$. This effect is not understood at this time and requires a rigorous

analysis. However, the absence of CO in the spectra during exposure to hydroxyacetone at 230 °C was not due to limited sensitivity of the technique.

The activity of both Pt/AlO(OH) and Pt/ZrO₂ used in this study in aqueous phase reforming of hydroxyacetone was measured by Vikla *et al.* [19] using catalysts from the same batch in a fixed-bed reactor at conditions (225 °C/35 bar) similar to the conditions used in this study. Typical yields of H₂, CO and CO₂ were 14.7%, 2.2% and 19% for Pt/AlO(OH), and 3.4%, 0.4% and 12.2% for Pt/ZrO₂, respectively, clearly demonstrating that the catalysts are active. Both catalysts also deactivated with time. WHSV value in the fixed bed reactor was significantly lower compared to the ATR-IR cell (3 g hydroxyacetone g cat⁻¹ h⁻¹ vs. 300 g hydroxyacetone g cat⁻¹ h⁻¹, respectively), suggesting 100 times lower conversion in the ATR-IR cell.

Dumesic *et al.* [35] have reported on formation of adsorbed CO on 2,1 wt. % Pt/Al₂O₃ catalyst during APR of methanol in liquid phase at 150 °C, 5,84 bar. CO coverage of 0.29 and 0.4 on Pt was observed for liquid phase reforming of 2 and 5 wt. % methanol, respectively. Similar results were obtained by Wawrzetz *et al.* [36] in APR of 20 wt.% glycerol on 3 wt.% Pt/Al₂O₃ at 225 °C, 29 bar. Two small peaks at 2050 and 1940 cm⁻¹ were observed [36] in the ATR-IR spectra, which were assigned to linear and bridge bound CO on Pt. However, this assignment can be debated because boehmite, which was formed from alumina during APR, has IR peaks in the same window. Copeland *et al.* [21] have studied activation of glycerol on 5 wt. % Pt/Al₂O₃ using ATR-IR spectroscopy at room temperature. Formation of two types of adsorbed CO was reported (i) CO interacting with co-adsorbed H₂ and (ii) CO interacting with molecularly adsorbed H₂O. The authors emphasized that the rates of CO formation and consumption strongly depend on the cleaning procedure of the catalyst layer prior to kinetic studies. The cleaning pretreatment included alternating flows of H₂- and O₂-saturated water. The cleaning procedure used in the current study was based on suggestions of Copeland *et al.* [21], thus the influence of the cleaning pretreatment on the formation of CO from hydroxyacetone can be neglected.

The absence of adsorbed CO in the APR experiment in the ATR-IR cell could be due to the following. It is possible that adsorbed CO is not involved in the rate-determining step in APR of hydroxyacetone, and desorption, water gas shift or methanation are fast compared to CO formation. It is also possible, as seen from the experiments in the fixed-bed reactor, that deactivation of the catalysts occurs and this prevents CO adsorption. In order to confirm this, analysis of gas phase products and determination of conversion levels simultaneously is required.

4.3.1 Other reforming products

Liquid phase reactions of hydroxyacetone such as hydrogenation, oxidation, hydration or dehydrogenation can result in the formation of various saturated/unsaturated C₃-alcohols and acids. However, the concentrations of these

products were much smaller than the concentration of the hydroxyacetone in the reaction mixture, which made it difficult to distinguish them in an IR spectrum, as it was dominated by hydroxyacetone peaks (**Figure S12** in Supplementary Information). Nevertheless, adsorption of these products or their consecutive conversion into other products or coke cannot be ruled out.

4.4 Identification of adsorbed species

In order to determine the origin of the new peaks at 1691, 1593, 1540, 1116 and 1055 cm^{-1} possible reactions of hydroxyacetone were considered. Generally, the bands around 1750-1650 cm^{-1} were assigned to carbonyl groups of various classes of molecules (carboxylic acids, aldehydes, ketones and esters). The frequency range between 1650 and 1500 cm^{-1} is assigned to unsaturated carbon-carbon vibrations and the bands in the range between 1500 and 1200 cm^{-1} are assigned to various deformation vibrations of CH_x groups [37]. This suggests that adsorbates contain carbonyl groups as well as unsaturated carbon-carbon bond.

Apart from undergoing reforming reaction, hydroxyacetone can undergo enolization and aldol condensation reactions. In both cases unsaturated carbon-carbon bond is formed, thus either enolization or aldol condensations products can be responsible for appearance of adsorbates peaks observed at 230 °C. Both options will be discussed in the following sections.

4.4.1 Enolization of hydroxyacetone

Hydroxyacetone can go through tautomerization, resulting in two types of enolic isomers – prop-1-ene-1,2-diol (enol 1) and prop-2-ene-1,2-diol (enol 2) (**Figure 13**). Low extent of enolization of hydroxyacetone in D_2O and in thiethylamine solution was reported by Yaylayan *et al.*[24]

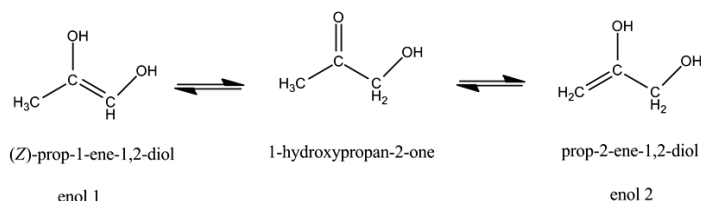


Figure 13. Structure of enols of hydroxyacetone.

DFT calculations of IR spectra of both enols in vacuum were performed. Calculated frequencies and intensities can be found in the **Table S1** in the Supplementary Information. According to the results obtained, enol 1 is ca. 20 kJ/mol more stable than enol 2 in vacuum. Both enols have C=C stretching vibrations together with C-OH stretching vibrations. However, the calculated frequencies of enols do not match the experimental frequencies observed on Pt/ZrO₂ at 230 °C, suggesting that adsorbed

species do not include enols. This qualitatively agrees with a DFT study on adsorption, tautomerization and decomposition of acetone on Pt (111) surface by Xu *et al.* [38], reporting that only a small amount of acetone could tautomerize into enol Pt (111) surface at room temperature.

4.4.2 Aldol condensation of hydroxyacetone

The structure of the two products of aldol condensation is influenced by the structure of the enol that condenses with hydroxyacetone (**Figure 14**). Thus, enol 1 produces 3,4,5-trihydroxy-4-methylpentan-2-one, whereas enol 2 gives 1,4,5-trihydroxy-4-methylpentan-2-one as addition products. The two addition compounds can further dehydrate giving (Z)-3,5-dihydroxy-4-methylpent-3-en-2-one (3,5-DH) and (Z)-1,5-dihydroxy-4-methylpent-3-en-2-one (1,5-DH) as products.

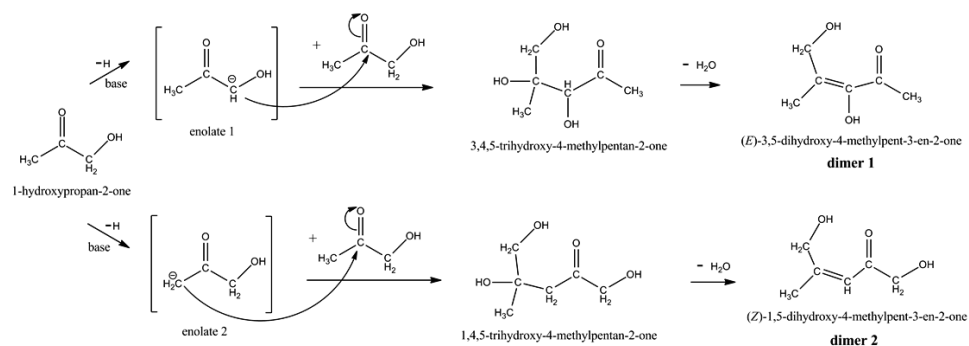


Figure 14. Two possible pathways of aldol condensation of hydroxyacetone.

Infrared spectra of both aldol condensation products were calculated in order to support peak assignments. It is important to note that all spectra have been calculated for the most stable conformations of the investigated molecules in the isolated state, thus deviations in peak positions and peak intensities can be expected when molecules are adsorbed on surfaces in presence of water. The validity of the DFT method was shown by comparing IR frequencies of hydroxyacetone obtained experimentally with those obtained from calculations. The calculated hydroxyacetone spectrum (**Table S1**) shows good agreement with the 2.5 wt. % experimental spectrum in water (**Figure 1a**). The influence of the presence of three water molecules on hydroxyacetone spectrum was also evaluated. Results reported for the two strongest hydroxyacetone peaks showed that the influence of water is negligible, since only minor shifts in frequencies and minor changes in the intensities were observed.

Furthermore, the calculated spectra of both of the enols and the addition products (**Table S1** in Supplementary Information) did not show peaks around 1600 cm^{-1} , thus they cannot be responsible for new peaks observed during the experiment of hydroxyacetone adsorption on catalysts. Finally, IR spectra of both aldol condensation products were calculated (**Table S1**) both in vacuum and in the presence of water.

Influence of water was estimated by the intermolecular interactions between the condensation product and six water molecules, which can be explained as the elongation of the C=O bond caused by hydrogen bonds and the delocalization of charge in the C=O and C=C coupled stretching vibrations. The results showed a decrease of 30 cm⁻¹ for the peaks located in the region between 1500 and 1700 cm⁻¹ and a negligible effect on the peaks below 1500 cm⁻¹. Comparison of the most important vibrational frequencies of both dimers in vacuum and in the presence water with experimental data is given in **Table 3**.

Table 3. Comparison of experimental frequencies (last spectrum in Figure 6a) with calculated frequencies of aldol condensation products of hydroxyacetone in vacuum and in the presence of six water molecules.

Experimental frequencies, cm ⁻¹	1691 (s) ^a	1593 (ms)	1540 (s)	1380 (vs)	1116 (w)	-	1055 (w)
Calculated frequencies, cm ⁻¹ :							
3,5-DH in vacuum	1684 (s) (-0.4 %) ^b	1637 (vs) (2.8 %)	1637 (vs) (6.3 %)	1370 (s) (-0.7 %)	1123 (s) (0.6 %)	-	1044 (ms) (-1.0 %)
3,5-DH surrounded by 6H ₂ O molecules	1654 (w) (-2.2 %)	1611 (vs) (1.1 %)	1611 (vs) (4.4 %)	1355 (s) (-1.8 %)	1115 (s) (-0.1 %)	-	1037 (s) (-1.7 %)
1,5-DH in vacuum	1687 (s) (-0.2 %)	1608 (vs) (0.9 %)	1608 (vs) (4.4 %)	1401 (s) (1.5 %)	1129 (ms) (1.2 %)	1086 (vs)	1056 (ms) (0.1 %)
1,5-DH surrounded by 6H ₂ O molecules	1651 (s) (-2.4 %)	1587 (vs) (-0.4 %)	1587 (vs) (3.1 %)	1396 (s) (1.2 %)	1128 (ms) (1.1 %)	1071 (vs)	1058 (w) 0.3 %)

^a Intensities of the peaks are presented as (vs) very strong, (s) strong, (ms) medium strong, (w) weak.

^b Deviations of calculated frequencies from experimental frequencies are given in the brackets. Peak assignments: 1691 cm⁻¹ - asymmetric stretching of C=O and C=C coupled vibrations, 1593 and 1540 cm⁻¹ - symmetric stretching of C=O and C=C coupled vibrations, 1116 cm⁻¹ - C-H bending in C=CH, 1055 cm⁻¹ - coupled C-OH stretching.

The calculated spectra of two condensation products are similar in the region of C=O and C=C vibrations, both having two coupled stretching vibrations around 1680 and 1600-1630 cm⁻¹. The coupling with the C=C stretching determines the shift of the C=O band to lower frequencies. Analysis of the deviations in peak positions and intensities (deviations are given in the brackets in **Table 3**) for both dimers shows good agreement with experimental results. These deviations are within the estimated accuracy of the calculation method. The calculated C=O frequency in the presence of water is shifted by around 2% compared to experimentally observed frequency. The comparison of C=C frequency is less clear, since two peaks at 1593 and 1540 cm⁻¹ were observed in the experimental spectrum and deviations between theory and experiment are somewhat larger.

Dimers 3,5-DH and 1,5-DH can be distinguished based on the vibrational band at 1086 cm^{-1} or 1071 cm^{-1} when corrected for water. This peak is absent in the spectrum of 3,5-DH and in the experimental spectrum (**Figure 6a**); thus, 3,5-DH seems to be dominant in aldol condensation of hydroxyacetone. The absence of this band is attributed to the presence of a hydrogen bond between the hydroxyl groups that determines the shift of the C-OH stretching band to the lower frequencies ($1044\text{--}1025\text{ cm}^{-1}$).

4.5 Nature of the support in aldol condensation

The different IR adsorption spectra for Pt/ZrO₂ and Pt/AlO(OH) presented in **Figure 3a** suggested that aldol condensation, as discussed in the previous section, does not occur on the surface of boehmite. This is probably due to the lower surface acidity of boehmite compared to zirconia. TPD NH₃ results (**Figure 8**) showed that total acidity of zirconia is higher than boehmite. Pyridine adsorption measured with IR (**Figure 7**) also suggested that Pt/ZrO₂ has high concentration of Lewis and Brønsted acid sites and Lewis basic sites, while Pt/AlO(OH) has low concentration of Lewis acid sites. It was suggested in literature [30, 39, 40] that zirconia can catalyze aldol condensation of acetone, due to its Lewis basicity. Thus, the condensation would proceed according to the mechanism suggested in **Figure 14**. However, since acidity of boehmite and $\gamma\text{-Al}_2\text{O}_3$ is similar, based on the pyridine desorption data, one can assume that boehmite may also catalyze aldol condensation *via* an acidic route. In fact, Ferri *et al.* [41] reported aldol condensation of ethyl pyruvate catalyzed by alumina, and Dumitriu *et al.* [42] studied aldol condensation of acetaldehyde on MFI zeolites. Our IR results, however, do not indicate formation of any condensation products on boehmite. Possibly, condensation products are not detected on AlO(OH) supported catalyst because Pt/AlO(OH) is more active in formation gaseous reforming products (CO_x, H₂, etc.) than Pt/ZrO₂ [19]; as reforming to CO_x competes with condensation reactions, this may well contribute to the difference in the formation of condensation products between AlO(OH) and ZrO₂.

4.6 Deactivation of the catalysts due to coke formation

TPO analysis of the samples after hydroxyacetone adsorption in the ATR-IR cell (**Figure 9**) showed higher peak intensities for Pt/ZrO₂ compared to Pt/AlO(OH), suggesting higher amount of coke on Pt/ZrO₂. Two different regions of oxidation temperatures around 300 °C and 450 °C were observed for both samples, with Pt/ZrO₂ having most of the coke burning at lower temperatures. Elemental analysis of the same samples (**Table 2**) showed the highest amount of coke on ZrO₂ sample, and the lowest coke amount on Pt/AlO(OH), which is in agreement with TPO results. The amount of coke on supports was higher than on Pt/support samples. These results suggest that

reactions on the surface of supports are possibly causing the accumulation of coke. The aldol condensation reaction is probably the first step in this sequence, since it leads to formation of molecules with long carbon chain with unsaturations. Oxidation temperatures of carbon deposits for Pt/ZrO₂ are well below the oxidation temperatures of hydrocarbon coke that is observed in *e.g.* methane dry reforming [43-45], suggesting that coke on Pt/ZrO₂ is a “soft” coke with high oxygen content. The results presented here are qualitatively in agreement with the characterization results obtained by Vikla *et al.* [19] by characterizing the same catalysts after APR of hydroxyacetone at 225 °C, 35 bar in a fixed-bed reactor.

Thus, aldol condensation of hydroxyacetone, resulting in formation of (E)-3,5-dihydroxy-4-methylpent-3-en-2-one, is likely to be the first step in the formation of oxygen rich deposits, significantly responsible for the catalyst deactivation in aqueous phase reforming of hydroxyacetone. The reforming reaction that takes place on Pt surface is competing with the condensation reaction; however, the acid-base properties of the support clearly influences the condensation reactions, leading to coke formation independent of the presence of Pt.

5. Conclusions

In situ Attenuated Total Reflection Infrared (ATR-IR) spectroscopy allows to study adsorbed species that form during exposure to hydroxyacetone on Pt/AlO(OH) and Pt/ZrO₂ catalysts under conditions of aqueous phase reforming, *i.e.* 230 °C/ 30 bar. In addition to reforming reaction, hydroxyacetone undergoes aldol condensation resulting in strongly adsorbed species when brought in contact with ZrO₂-based catalyst due to the presence of Lewis acid and basic sites. However, no condensation products were observed on AlO(OH)-based catalyst due to its weak Lewis acidity. Carbonaceous deposits with low oxidation temperatures, as showed by elemental analysis and TPO analysis, are suggested to be due to hydroxyacetone condensation, leading to catalyst deactivation. Additionally, absence of adsorbed CO in the spectra suggests that either CO consumption is not rate-limiting or catalyst deactivation prevents CO adsorption. In order to confirm this analysis of gas phase products and determination of conversion levels simultaneously is required.

6. Acknowledgements

This research has been performed within the framework of the CatchBio program (project number 053.70.002). The authors gratefully acknowledge the support of the Smart Mix Program of the Netherlands Ministry of Economic Affairs and the Netherlands Ministry of Education, Culture and Science. A.K.K. Vikla gratefully acknowledges the funding of the European Union Seventh Framework Programme (FP7/2007-2013)

within the SusFuelCat project under grant agreement No 310490 (www.susfuelcat.eu). Authors thank Tom Velthuizen and Karin Altena - Schildkamp for BET and XRF analyses, Ing. Bert Geerdink for technical help in building the ATR-IR setup. K. Koichumanova thanks Erik Dietrich for help with data processing in Matlab.

7. References

1. Cortright, R.D., R.R. Davda, and J.A. Dumesic, *Hydrogen from catalytic reforming of biomass-derived hydrocarbons in liquid water*. *Nature*, 2002. **418**(6901): p. 964-967.
2. Huber, G.W., J.W. Shabaker, and J.A. Dumesic, *Raney Ni-Sn catalyst for H₂ production from biomass-derived hydrocarbons*. *Science*, 2003. **300**(5628): p. 2075-2077.
3. Davda, R.R., R. Alcalá, J. Shabaker, G. Huber, R.D. Cortright, M. Mavrikakis, and J.A. Dumesic, *DFT and experimental studies of C-C and C-O bond cleavage in ethanol and ethylene glycol on Pt catalysts*. 2002. p. 79-84.
4. Davda, R.R., J.W. Shabaker, G.W. Huber, R.D. Cortright, and J.A. Dumesic, *A review of catalytic issues and process conditions for renewable hydrogen and alkanes by aqueous-phase reforming of oxygenated hydrocarbons over supported metal catalysts*. *Applied Catalysis B-Environmental*, 2005. **56**(1-2): p. 171-186.
5. De Vlieger, D.J.M., B.L. Mojet, L. Lefferts, and K. Seshan, *Aqueous Phase Reforming of ethylene glycol - Role of intermediates in catalyst performance*. *Journal of Catalysis*, 2012. **292**: p. 239-245.
6. Koichumanova, K., A.K.K. Vikla, D.J.M. de Vlieger, K. Seshan, B.L. Mojet, and L. Lefferts, *Towards Stable Catalysts for Aqueous Phase Conversion of Ethylene Glycol for Renewable Hydrogen*. *Chemsuschem*, 2013. **6**(9): p. 1717-1723.
7. Koichumanova, K., K.B. Sai Sankar Gupta, L. Lefferts, B.L. Mojet, and K. Seshan, *In situ ATR-IR spectroscopy study of aluminas under aqueous phase reforming conditions*. *Physical Chemistry Chemical Physics*, 2015.
8. DeVlieger, D.J.M., D.B. Thakur, L. Lefferts, and K. Seshan, *Carbon Nanotubes: A Promising Catalyst Support Material for Supercritical Water Gasification of Biomass Waste*. *ChemCatChem*, 2012. **4**(12): p. 2068-2074.
9. De Vlieger, D.J.M., L. Lefferts, and K. Seshan, *Ru decorated carbon nanotubes-a promising catalyst for reforming bio-based acetic acid in the aqueous phase*. *Green Chemistry*, 2014. **16**(2): p. 864-874.
10. Ciftci, A., D.A.J. Michel, and E.J.M. Hensen, *Influence of Pt particle size and Re addition by catalytic reduction on aqueous phase reforming of glycerol for carbon-supported Pt(Re) catalysts*. *Applied Catalysis B: Environmental*, 2015. **174-175**: p. 126-135.
11. Oasmaa, A. and D. Meier, *Norms and standards for fast pyrolysis liquids: 1. Round robin test*. *Journal of Analytical and Applied Pyrolysis*, 2005. **73**(2): p. 323-334.
12. Vitasari, C.R., G.W. Meindersma, and A.B. de Haan, *Water extraction of pyrolysis oil: The first step for the recovery of renewable chemicals*. *Bioresource Technology*, 2011. **102**(14): p. 7204-7210.
13. Trane-Restrup, R., D.E. Resasco, and A.D. Jensen, *Steam reforming of light oxygenates*. *Catalysis Science & Technology*, 2013. **3**(12): p. 3292-3302.
14. Bimbela, F., M. Oliva, J. Ruiz, L. García, and J. Arauzo, *Catalytic steam reforming of model compounds of biomass pyrolysis liquids in fixed bed: Acetol and n-butanol*. *Journal of Analytical and Applied Pyrolysis*, 2009. **85**(1-2): p. 204-213.

15. Ramos, M.C., A.I. Navascués, L. García, and R. Bilbao, *Hydrogen production by catalytic steam reforming of acetol, a model compound of bio-oil*. Industrial and Engineering Chemistry Research, 2007. **46**(8): p. 2399-2406.
16. Medrano, J.A., M. Oliva, J. Ruiz, L. García, and J. Arauzo, *Catalytic steam reforming of model compounds of biomass pyrolysis liquids in fluidized bed reactor with modified Ni/Al catalysts*. Journal of Analytical and Applied Pyrolysis, 2009. **85**(1-2): p. 214-225.
17. Dubey, V.R. and P.D. Vaidya, *Kinetics of steam reforming of acetol over a Pt/C catalyst*. Chemical Engineering Journal, 2012. **180**: p. 263-269.
18. Hakim, S.H., B.H. Shanks, and J.A. Dumesic, *Catalytic upgrading of the light fraction of a simulated bio-oil over CeZrOx catalyst*. Applied Catalysis B: Environmental, 2013. **142-143**: p. 368-376.
19. Vikla, A.K.K., K. Koichumanova, K. Seshan, and L. Lefferts, *Comparison of hydrothermally stable catalysts supports for APR of hydroxyacetone*. in preparation, 2015.
20. Koichumanova, K., A. Visan, R.G.H. Lammertink, B. Geerdink, B.L. Mojet, K. Seshan, and L. Lefferts, *ATR-IR cell to study reactions in situ at elevated temperatures and pressures*. in preparation, 2015.
21. Copeland, J.R., G.S. Foo, L.A. Harrison, and C. Sievers, *In situ ATR-IR study on aqueous phase reforming reactions of glycerol over a Pt/ γ -Al₂O₃ catalyst*. Catalysis Today, 2013. **205**(0): p. 49-59.
22. Frisch, M.J., *Gaussian 09*, F. M.J., Editor. 2009, Gaussian, Inc.: Wallingford, CT, USA.
23. Mohaček-Grošev, V., *Vibrational analysis of hydroxyacetone*. Spectrochimica Acta Part A: Molecular and Biomolecular Spectroscopy, 2005. **61**(3): p. 477-484.
24. Yaylayan, V.A., S. Harty-Majors, and A.A. Ismail, *Monitoring carbonyl-amine reaction and enolization of 1-hydroxy-2-propanone (acetol) by FTIR spectroscopy*. Journal of Agricultural and Food Chemistry, 1999. **47**(6): p. 2335-2340.
25. Dickie, S.A. and A.J. McQuillan, *In-situ infrared spectroscopic studies of adsorption processes on boehmite particle films: Exchange of surface hydroxyl groups observed upon chelation by acetylacetone*. Langmuir, 2004. **20**(26): p. 11630-11636.
26. Tunega, D., H. Pasalić, M.H. Gerzabek, and H. Lischka, *Theoretical study of structural, mechanical and spectroscopic properties of boehmite (γ -AlOOH)*. Journal of Physics Condensed Matter, 2011. **23**(40).
27. Ram, S., *Infrared spectral study of molecular vibrations in amorphous, nanocrystalline and AlO(OH)· n H₂O bulk crystals*. Infrared Physics & Technology, 2001. **42**(6): p. 547-560.
28. Mojet, B.L., S.D. Ebbesen, and L. Lefferts, *Light at the interface: the potential of attenuated total reflection infrared spectroscopy for understanding heterogeneous catalysis in water*. Chem Soc Rev, 2010. **39**(12): p. 4643-55.
29. Zaki, M.I., M.A. Hasan, F.A. Al-Sagheer, and L. Pasupulety, *In situ FTIR spectra of pyridine adsorbed on SiO₂-Al₂O₃, TiO₂, ZrO₂ and CeO₂: General considerations for the identification of acid sites on surfaces of finely divided metal oxides*. Colloids and Surfaces A: Physicochemical and Engineering Aspects, 2001. **190**(3): p. 261-274.
30. Zaki, M.I., M.A. Hasan, and L. Pasupulety, *Surface reactions of acetone on Al₂O₃, TiO₂, ZrO₂, and CeO₂: IR spectroscopic assessment of impacts of the surface acid-base properties*. Langmuir, 2001. **17**(3): p. 768-774.
31. Takagaki, A., J.C. Jung, and S. Hayashi, *Solid Lewis acidity of boehmite γ -AlO(OH) and its catalytic activity for transformation of sugars in water*. RSC Advances, 2014. **4**(82): p. 43785-43791.
32. Krishna Priya, G., P. Padmaja, K.G.K. Warriar, A.D. Damodaran, and G. Aruldas, *Dehydroxylation and high temperature phase formation in sol-gel boehmite characterized by*

- Fourier transform infrared spectroscopy*. Journal of Materials Science Letters, 1997. **16**(19): p. 1584-1587.
33. Tsukada, T., H. Segawa, A. Yasumori, and K. Okada, *Crystallinity of boehmite and its effect on the phase transition temperature of alumina*. Journal of Materials Chemistry, 1999. **9**(2): p. 549-553.
 34. Krokidis, X., P. Raybaud, A.E. Gobichon, B. Rebours, P. Euzen, and H. Toulhoat, *Theoretical study of the dehydration process of boehmite to γ -alumina*. Journal of Physical Chemistry B, 2001. **105**(22): p. 5121-5130.
 35. He, R., R.R. Davda, and J.A. Dumesic, *In situ ATR-IR spectroscopic and reaction kinetics studies of water-gas shift and methanol reforming on Pt/Al₂O₃ catalysts in vapor and liquid phases*. J Phys Chem B, 2005. **109**(7): p. 2810-20.
 36. Wawrzetz, A., B. Peng, A. Hrabar, A. Jentys, A.A. Lemonidou, and J.A. Lercher, *Towards understanding the bifunctional hydrodeoxygenation and aqueous phase reforming of glycerol*. Journal of Catalysis, 2010. **269**(2): p. 411-420.
 37. Colthup, N.B., L.H. Daly, and S.E. Wiberley, *Introduction to Infrared and Raman Spectroscopy*. 1990, USA: Academic Press.
 38. Xu, M., X.L. Huai, and H. Liu, *Role of keto-enol isomerization on surface chemistry and hydrogenation of acetone on pt(111): A DFT study*. Industrial and Engineering Chemistry Research, 2014. **53**(13): p. 5451-5454.
 39. Crocellà, V., G. Cerrato, and C. Morterra, *On the adsorption/reaction of acetone on pure and sulfate-modified zirconias*. Physical Chemistry Chemical Physics, 2013. **15**(32): p. 13446-13461.
 40. Zaki, M.I., M.A. Hasan, F.A. Al-Sagheer, and L. Pasupulety, *Surface chemistry of acetone on metal oxides: IR observation of acetone adsorption and consequent surface reactions on silica-alumina versus silica and alumina*. Langmuir, 2000. **16**(2): p. 430-436.
 41. Ferri, D., S. Diezi, M. Maciejewski, and A. Baiker, *Alumina-catalysed degradation of ethyl pyruvate during enantioselective hydrogenation over Pt/alumina and its inhibition by acetic acid*. Applied Catalysis a-General, 2006. **297**(2): p. 165-173.
 42. Dumitriu, E., V. Hulea, I. Fechete, A. Auroux, J.-F. Lacaze, and C. Guimon, *The aldol condensation of lower aldehydes over MFI zeolites with different acidic properties*. Microporous and Mesoporous Materials, 2001. **43**(3): p. 341-359.
 43. Guo, J., H. Lou, H. Zhao, D. Chai, and X. Zheng, *Dry reforming of methane over nickel catalysts supported on magnesium aluminate spinels*. Applied Catalysis A: General, 2004. **273**(1-2): p. 75-82.
 44. Guo, J., H. Lou, and X. Zheng, *The deposition of coke from methane on a Ni/MgAl₂O₄ catalyst*. Carbon, 2007. **45**(6): p. 1314-1321.
 45. Tsyganok, A.I., T. Tsunoda, S. Hamakawa, K. Suzuki, K. Takehira, and T. Hayakawa, *Dry reforming of methane over catalysts derived from nickel-containing Mg-Al layered double hydroxides*. Journal of Catalysis, 2003. **213**(2): p. 191-203.

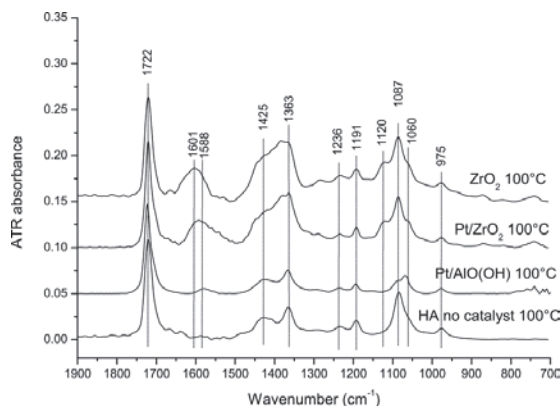


Figure S1. Water subtracted *in situ* ATR-IR spectra of hydroxyacetone adsorption on Pt/ZrO₂, ZrO₂, Pt/AlO(OH) at 100 °C, 20 bar after 60 min.

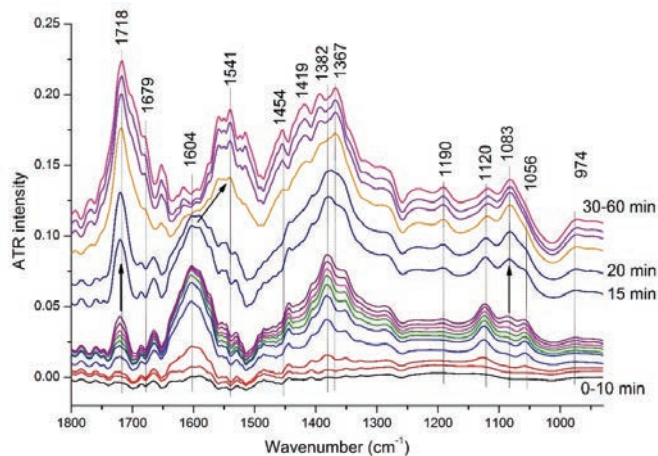


Figure S2. Time resolved water corrected *in situ* ATR-IR spectra of hydroxyacetone initial adsorption over ZrO₂ at 230°C, 30 bar. Spectra with time difference of 1 min are presented during the first 10 min, further spectra have time difference of 5 or 10 min.

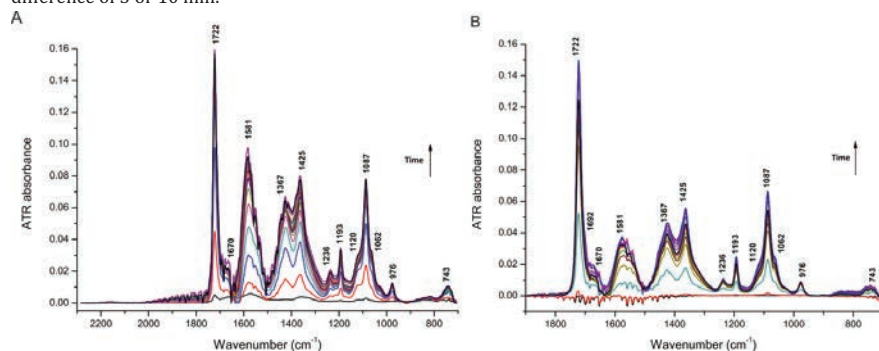


Figure S3. Time resolved water corrected *in situ* ATR-IR spectra of hydroxyacetone initial adsorption at 25°C, 1 bar over (a) ZrO₂ and (b) Pt/ZrO₂. First 10 spectra have time difference of 1 min, further spectra have time difference of 10 min.

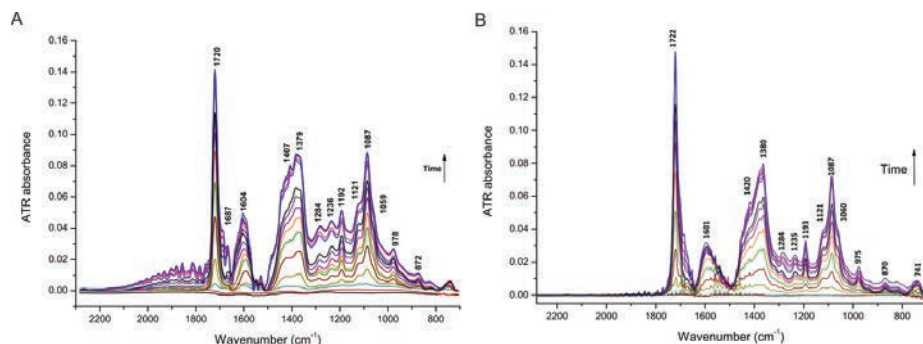


Figure S4. Time resolved water corrected *in situ* ATR-IR spectra of hydroxyacetone initial adsorption at 100°C, 20 bar over (a) ZrO₂ and (b) Pt/ZrO₂. First 10 spectra have time difference of 1 min, further spectra have time difference of 10 min.

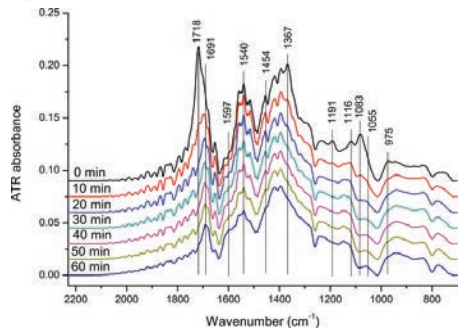


Figure S5. Time resolved water corrected *in situ* ATR-IR spectra during hydroxyacetone removal with H₂O on ZrO₂ at 230°C, 30 bar. Spectra with time difference of 10 min are presented during 60 min.

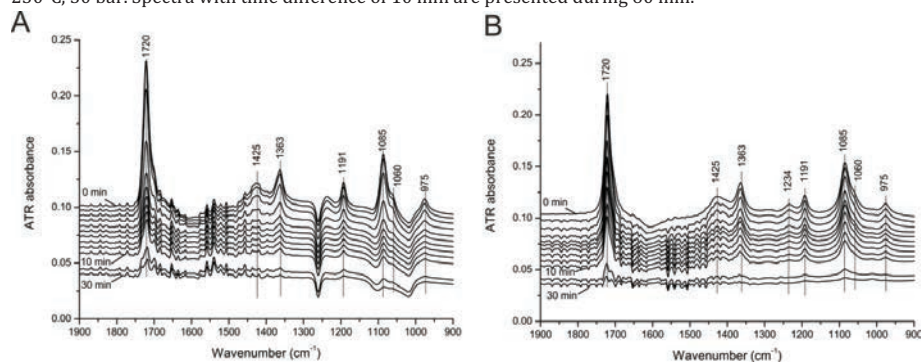


Figure S6. Time resolved water corrected *in situ* ATR-IR spectra during hydroxyacetone removal with H₂O on bare ZnSe at (a) 30°C, 1 bar and (b) 100°C, 20 bar. Spectra with time difference of 1 min are presented during first 10 min, further spectra have time difference of 10 min.

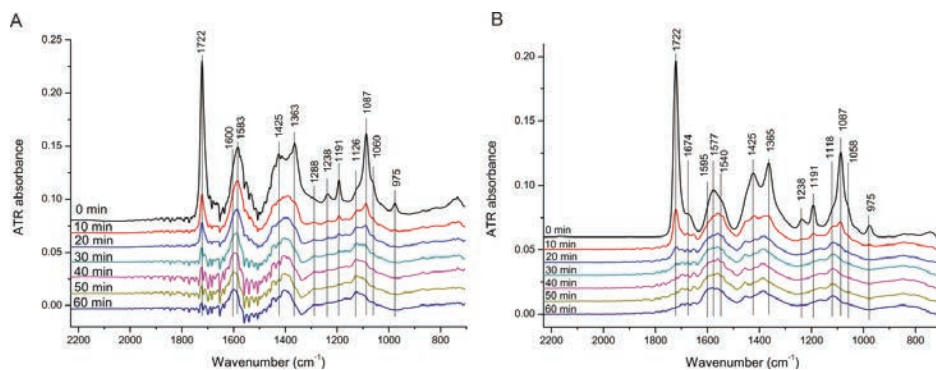


Figure S7. Time resolved water corrected *in situ* ATR-IR spectra during hydroxyacetone removal with H₂O on (a) ZrO₂ at 30°C, 1 bar and (b) Pt/ZrO₂ at 30°C, 1 bar. Spectra with time difference of 10 min are presented during 60 min.

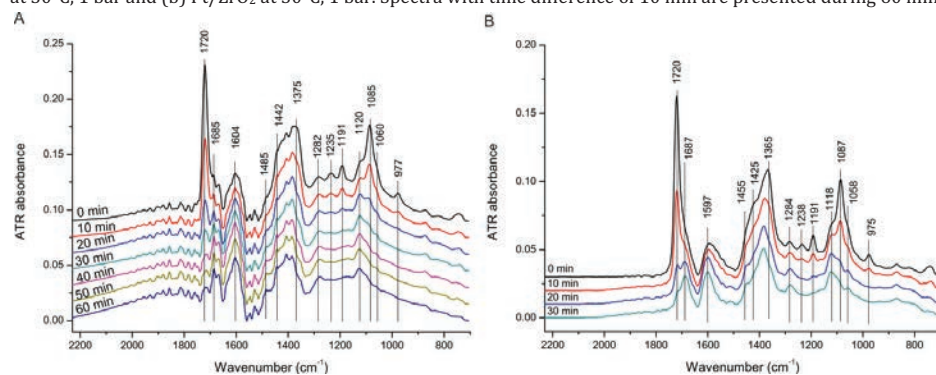


Figure S8. Time resolved water corrected *in situ* ATR-IR spectra during hydroxyacetone removal with H₂O on (a) ZrO₂ at 100°C, 20 bar and (b) Pt/ZrO₂ at 100°C, 20 bar. Spectra with time difference of 10 min are presented during 60 min.

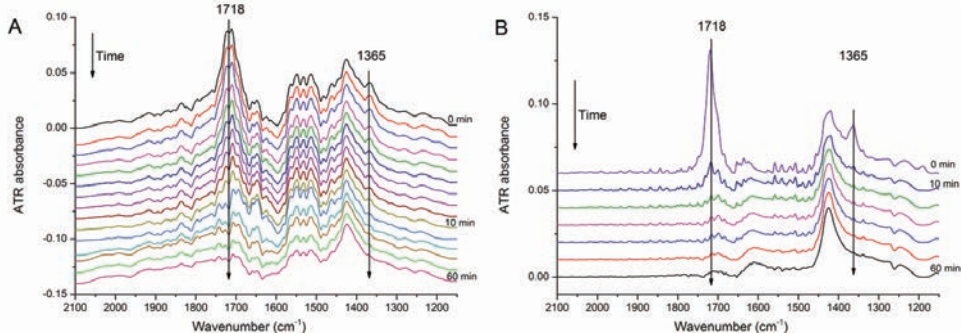


Figure S9. Time resolved water corrected *in situ* ATR-IR spectra during hydroxyacetone removal with H₂O on (a) Pt/AlO(OH) and (b) AlO(OH) at 230°C, 30 bar. (a) Spectra with time difference of 1 min are presented during first 10 min, further spectra have time difference of 10 min, (b) Spectra with time difference of 10 min are presented during 60 min.

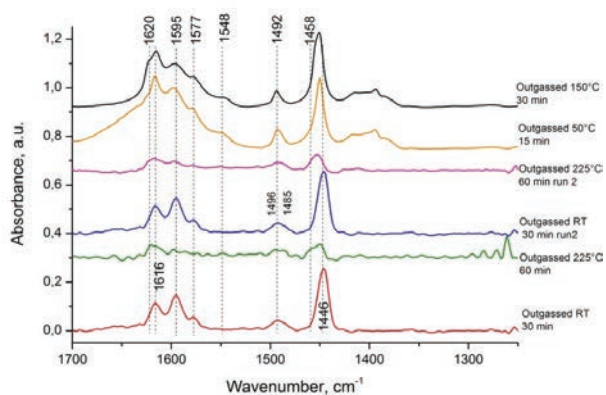


Figure S10. FTIR spectra of pyridine adsorption on Pt/AlO(OH) after evacuation at RT (red and blue), 225 °C (green and purple) and on Pt/Al₂O₃ after evacuation at 50 °C (orange) and 150 °C (black).

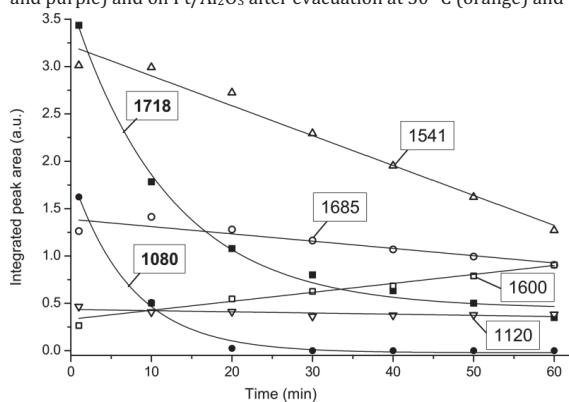


Figure S11. Integrated areas of peaks at 1718 cm⁻¹ and 1080 cm⁻¹ assigned to hydroxyacetone and peaks at 1685, 1600, 1541 and 1120 cm⁻¹ assigned to adsorbates while hydroxyacetone is being washed out from the cell with ZrO₂ at 230°C, 30 bar during 60 min. The purpose of the lines is to guide the eye.

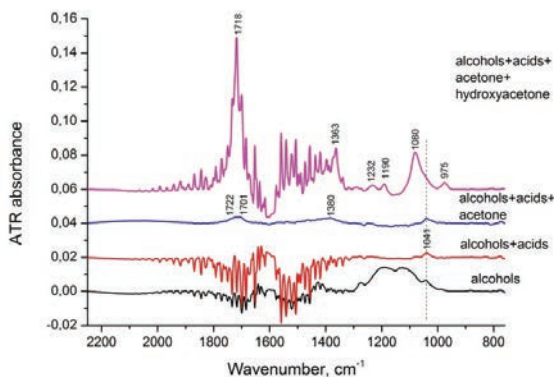


Figure S12. ATR-IR spectra of mixtures of liquid products detected by HPLC.

Table S1. Infrared spectra of hydroxyacetone, enols, addition products and condensation products in vacuum and in the presence of water, according to DFT calculations. Intensities of the peaks are given in the brackets and marked as following: vs - very strong ($I > 139$ a.u.), s - strong ($I = 70-138$ a.u.), ms - medium strong ($I = 22-69$ a.u.), w - weak ($I < 22$ a.u.)

Hydroxyacetone	Hydroxyacetone+3 H ₂ O	enol form 1	enol form 2	(Z)-1,5-dihydroxy-4-methyl-pent-3-en-2-one (from enol 1)	(Z)-1,5-dihydroxy-4-methyl-pent-3-en-2-one + 6H ₂ O	(Z)-3,5-dihydroxy-4-methyl-pent-3-en-2-one (from enol 2)	(Z)-3,5-dihydroxy-4-methyl-pent-3-en-2-one + 6H ₂ O
v, cm ⁻¹	v, cm ⁻¹	v, cm ⁻¹	v, cm ⁻¹	v, cm ⁻¹	v, cm ⁻¹	v, cm ⁻¹	v, cm ⁻¹
1751 (vs)	1749 (vs)		1715 (ms)				
		1688 (s)		1687 (s)	1651 (s)	1684 (s)	1654 (w)
				1608 (vs)	1587 (vs)	1637 (vs)	1611 (vs)
		1509 (w)					
1447 (w)			1465 (w)	1448 (w)	1396 (s)	1462 (w)	1355 (s)
1436 (w)				1442 (ms)		1459 (w)	
1427 (w)		1421 (w)	1427 (w)	1436 (w)		1448 (w)	
			1397 (w)	1433 (w)		1447 (w)	
1403 (ms)			1358 (w)	1430 (w)		1434 (w)	
						1408 (ms)	
1363 (ms)		1373 (ms)	1333 (s)	1401 (s)		1393 (w)	
		1345 (w)		1388 (w)		1370 (s)	
		1321 (w)		1358 (w)		1360 (ms)	
						1338 (ms)	
1276 (s)		1204 (ms)	1215 (s)	1272 (s)		1233 (vs)	
1224 (w)				1250 (w)			
				1233 (s)			
				1222 (w)			
1181 (ms)		1136 (s)	1160 (s)	1170 (w)		1183 (ms)	
1092 (vs)	1094 (s)	1022 (s)	1077 (s)	1129 (ms)	1228 (ms)	1123 (s)	1115 (s)
1078 (w)			1045 (w)	1086 (vs)	1071 (vs)	1044 (ms)	1037 (s)
				1056 (ms)	1058 (w)	1029 (ms)	
				1054 (w)	1055 (w)	1025 (ms)	
						1013 (w)	
943 (w)		977 (ms)	990 (w)	997 (w)		976 (ms)	
		959 (w)		992 (s)		916 (w)	
				935 (w)			
				910 (ms)			
852 (w)		847 (w)	890 (w)	813 (w)		888 (w)	
780 (w)		820 (ms)	722 (w)	782 (w)			
		702 (w)		723 (w)			

Chapter 6

Conclusions and Recommendations

Conclusions and Recommendations

Correlation of catalyst activity to its structure is an important step in the development of an efficient catalyst for a heterogeneously catalyzed process. *In situ* spectroscopic studies of the catalyst's state and the adsorbed species under the reaction conditions can contribute significantly to the understanding of the reaction sequences and the structure of the catalytic active site. For example, information about the surface species responsible for catalyst deactivation or the changes in catalyst structure under the reaction conditions can be obtained, thus suggesting routes for catalyst improvement. However, the reaction conditions and the presence of a solvent can be a challenge for *in situ* investigations due to the limitations of the techniques.

Attenuated Total Reflection Infrared (ATR-IR) spectroscopy, discussed in detail in this thesis, is a technique of choice when phenomena at the solid-liquid interface, especially at solid/water interface, are studied. Applicability of the ATR-IR spectroscopy for *in situ* studies of water/catalyst interface in Aqueous Phase Reforming (APR) was the main target of the work presented in this thesis. Since APR reaction requires high temperatures and pressures (150 - 350 °C and 10 - 50 bar), an ATR-IR cell suitable for these conditions had to be designed and tested. Hence, results presented in **Chapter 2** describe the design of *in situ* ATR-IR Tunnel cell with cylindrical IRE coated with a mechanically stable catalyst layer. Hydrodynamic flow simulations showed non-plug flow behavior in the cell. Residence time distributions obtained from simulations show good agreement with the experimental results for acetone and glycerol solutions. In our opinion, such a simulation is essential to support concentration changes that occur during reactions to be able to establish operational regions *i.e.*, transient *vs* steady state. The results of simulation also allow one to correlate changes in IR spectra with concentration changes during kinetic experiments, allowing to follow changes in concentration of surface species. The information about residence time distribution in the cell is important for Modulation excitation spectroscopy (MES) where sensitivity toward both bulk and surface species is enhanced by periodic perturbation of a parameter, *e.g.* concentration or temperature, leading to oscillating response of certain species [1].

The diffusion in the porous catalyst layer is another important factor influencing residence time distribution, which was not included in the current simulations. Further studies are needed on this topic.

Applicability of ATR-IR spectroscopy under APR conditions was demonstrated by studying the real-time conversion of γ -Al₂O₃ to boehmite under hydrothermal conditions of APR (**Chapters 3 and 4**). The results showed that this transformation leads to catalyst deactivation together with Pt sintering and blockage of the Pt surface with boehmite. Activation energy barriers for the transformation of γ -Al₂O₃ to boehmite were calculated based on changes in the characteristic spectral intensities. The formation of

boehmite was established by Raman spectroscopy and ^{27}Al MAS NMR analysis of samples before and after exposure to APR conditions. Based on the presented results and in agreement with other studies, it was suggested that Pt hinders the transformation by association with mono-coordinated OH groups of $\gamma\text{-Al}_2\text{O}_3$, which are nucleation points for the transformation to boehmite. The inhibiting effect of ethylene glycol is shown as due to formation of carbonaceous deposits that protect the surface from hydroxylation. Additionally, it was shown that boehmite is a stable phase at APR conditions and is efficient as a support for Pt based catalysts for APR of ethylene glycol. Additionally, the Pt/AlO(OH) catalyst shows good activity for hydrogen formation. This may be caused by both the extensively hydroxylated boehmite surface, possibly favoring the bifunctional reforming mechanism involving adsorbed carbonaceous species on Pt and water activation *via* hydroxyl groups on the support, as well as by enhancing the oxidation of Pt. Additional studies on surface hydroxyls of boehmite are needed to determine the acid strength that is responsible for APR activity.

In situ ATR-IR spectroscopy was also used to study adsorption of hydroxyacetone on Pt/AlO(OH) and Pt/ZrO₂ catalysts at 230 °C / 30 bar (**Chapter 5**). Formation of aldol condensation products of hydroxyacetone strongly adsorbed on the surface was observed on Pt/ZrO₂ and ZrO₂ in contrast to Pt/AlO(OH) and AlO(OH). Peak assignments were supported by DFT calculations of the theoretical IR spectra of the condensation products in vacuum and in the presence of water. The amount and type of coke deposits determined by elemental analysis and TPO showed that coke with low oxidation temperatures was deposited mostly on the surface of the ZrO₂ support. Surprisingly, no adsorbed CO was observed in the spectra, suggesting that either CO consumption is not rate-limiting or catalyst deactivation prevents CO adsorption. In order to confirm this analysis of gas phase products and determination of conversion levels simultaneously is required. Further investigations of hydroxyacetone adsorption states on the surface of both Pt and support (boehmite, zirconia or other supports) can help to understand the pathways of aldehydes and ketones conversion under APR conditions. This will contribute significantly to the development of the efficient catalyst for APR of oxygenates mixtures.

The ATR-IR spectra of hydroxyacetone reaction coupled with spectra collected during washout with water showed the ability of ATR-IR to detect strongly adsorbed surface species. Additionally, it was concluded that it is not possible to detect liquid phase products of hydroxyacetone reforming that are present in smaller quantities compared to the reactant. This is an inherent limitation of the technique.

There are also recommendations for technical upgrading of the ATR-IR cell based on the experimental results obtained. These recommendations can be taken into account for future investigations using the ATR-IR Tunnel cell. Such improvements include (i) installation of additional thermocouples and thermal insulation for the conical mirrors in the cell for uniform temperature profile and (ii) improving the performance of O-rings

minimizing leakage into the IR cell chamber, which decreases the signal quality, making it difficult to distinguish peaks with low intensity. Correlation of IR peak intensities to concentrations of the adsorbed species and the amount of catalyst will help quantification of the results.

Additionally, the possibility of an on-line/off-line reactant and product analysis using UV-Vis spectroscopy or HPLC chromatography can be considered for *operando* studies. The simultaneous measurements of the conversions together with IR spectral changes from the surface of the catalyst will make the investigations more complete.

Thorough understanding and refinement of the spray coating technique for catalyst deposition, that is suggested in this thesis, are needed. Before coating, catalyst particle size in a slurry can be measured by using Dynamic Light Scattering analysis, and a uniform size distribution of particles can be achieved by ball-milling the slurry. This can help decreasing inhomogeneity and existence of the voids in the resulting layer.

The characterization of the layer using additional techniques is recommended. For example, properties such as layer thickness, porosity and complex refractive index of the layer can be evaluated by using ellipsometry, which is a common technique for characterization of thin films [2, 3]. Optimization of the coating technique is also needed for other types of catalysts apart from the ones used in this thesis and, if applicable, dip coating technique should be considered.

Furthermore, the appearance of reversible broad bands in the region between 1200 and 1000 cm^{-1} at high temperatures as discussed in **Chapter 2** is still an issue influencing the assignment of peaks in the IR spectra. The nature of these bands still has to be understood. Modelling of the optical pathways of IR beam within the cylindrical IRE can help to reveal the exact patterns of the total internal reflection for the case of curved crystal/sample boundary. This information can potentially give an explanation for the broad bands observed in the spectra. Moreover, little is known about the nature the attachment between the catalyst and the crystal. Surface properties of ZnSe, its electronic state and longtime influence of the catalyst particles on surface roughness of the polished crystal was not studied yet. This can be a subject of further investigations.

Finally, the data analysis can be improved by applying chemometric methods reported in literature such as multivariate analysis [4, 5]. Attempts have been made by other scientists to distinguish spectra of the solvent from those of the reactant to accurately define the concentration profiles of the reactant.

We have shown successfully that ATR-IR spectroscopy is a useful tool for studies of reactions at water/catalyst interface, using APR as an example reaction. Both catalyst structure and surface species can be studied under realistic reaction conditions, suggesting improvements for catalyst development. Further studies in the field of APR, such as performance of bimetallic catalysts and utilization of carbon-based supports, are possible. The kinetics of WGS reaction can also be monitored separately by following rates of adsorbed CO formation or consumption.

The applicability of the ATR-IR cell for operation at high temperature and high pressure liquid conditions opens up the possibilities of using this technique for other liquid phase reactions in heterogeneous catalysis, for example hydrogenation reactions. Summarizing, the design and the operation limits of the technique can be adjusted to required reaction conditions, broadening its applicability for heterogeneous liquid-phase catalysis.

References

1. Meier, D.M., A. Urakawa, R. Mäder, and A. Baiker, *Design and performance of a flow-through polarization-modulation infrared reflection-absorption spectroscopy cell for time-resolved simultaneous surface and liquid phase detection under concentration and temperature perturbations*. Review of Scientific Instruments, 2009. **80**(9).
2. Gâlcă, A.C., E. Stefan Kooij, H. Wormeester, C. Salm, V. Leca, J.H. Rector, and B. Poelsema, *Structural and optical characterization of porous anodic aluminum oxide*. Journal of Applied Physics, 2003. **94**(7): p. 4296-4305.
3. Aguilar-Gama, M.T., E. Ramírez-Morales, Z. Montiel-González, A. Mendoza-Galván, M. Sotelo-Lerma, P.K. Nair, and H. Hu, *Structure and refractive index of thin alumina films grown by atomic layer deposition*. Journal of Materials Science: Materials in Electronics, 2014.
4. Ortiz-Hernandez, I., D. Jason Owens, M.R. Strunk, and C.T. Williams, *Multivariate analysis of ATR-IR spectroscopic data: Applications to the solid-liquid catalytic interface*. Langmuir, 2006. **22**(6): p. 2629-2639.
5. Guzman, M., J. Ruzicka, G.D. Christian, and P. Shelley, *Enhancement of Fourier transform infrared spectrometry by the flow-injection technique: Transmittance and internal total reflectance cell in a single-line system*. Vibrational Spectroscopy, 1991. **2**(1): p. 1-14.

Summary

Development of an efficient catalyst in heterogeneous catalysis includes understanding the relationship between catalyst structure and its activity. *In situ* spectroscopy methods can be used to study structure of the catalytic active site and reaction sequences under reaction conditions. Information obtained from such analyses, *e.g.* the structure of the surface species responsible for catalyst deactivation or the changes in catalyst structure under the reaction conditions, can suggest routes for catalyst improvement. However, the limited applicability of the techniques in real reaction conditions and especially in the presence of a solvent can be a challenge for *in situ* investigations.

Attenuated Total Reflection Infrared (ATR-IR) spectroscopy, discussed in detail in this thesis, is a technique used for studies at solid-liquid interface, especially at solid/water interface. The main target of the work presented in this thesis is applicability of the ATR-IR spectroscopy for *in situ* studies of the water/catalyst interface in Aqueous Phase Reforming (APR). APR reaction requires high temperatures and pressures (150 - 350 °C and 10 - 50 bar), therefore a suitable ATR-IR cell had to be designed and tested for these conditions. Results presented in Chapter 2 describe the design of an *in situ* ATR-IR Tunnel cell with a cylindrical Internal Reflection Element coated with a mechanically stable catalyst layer. Hydrodynamic flow simulations showed non-plug flow behavior in the cell. Residence time distributions obtained from simulations show good agreement with the experimental results for acetone and glycerol solutions. Such a simulation is essential to support concentration changes that occur during reactions to be able to establish specific operational modes *i.e.*, transient vs steady state. The results of simulation also allow one to correlate changes in IR spectra with concentration changes during kinetic experiments, allowing to exclude changes related to hydrodynamics of the flow and follow changes in concentration of surface species.

Applicability of ATR-IR spectroscopy under APR conditions was demonstrated by studying the conversion of γ -Al₂O₃ to boehmite in real-time under hydrothermal conditions of APR. The results presented in Chapter 3 and 4 showed that this transformation leads to catalyst deactivation together with Pt sintering and blockage of the Pt surface with boehmite. Activation energy barriers for the transformation of γ -Al₂O₃ to boehmite were calculated based on changes in the characteristic spectral intensities. The formation of boehmite was established by Raman spectroscopy and ²⁷Al MAS NMR analysis of samples before and after exposure to APR conditions. Based on the presented results and in agreement with other studies, it was suggested that Pt hinders the transformation by association with mono-coordinated OH groups of γ -Al₂O₃, which seem to act as nucleation points for the transformation to boehmite. The inhibiting effect

of ethylene glycol is shown as due to formation of carbonaceous deposits that protect the surface from hydroxylation. Additionally, it was shown that boehmite is a stable phase at APR conditions and is efficient as a support for Pt based catalysts for APR of ethylene glycol. Moreover, the Pt/AlO(OH) catalyst shows good activity for hydrogen formation. This may be caused by both the extensively hydroxylated boehmite surface, possibly favoring the bifunctional reforming mechanism involving adsorbed carbonaceous species on Pt and water activation *via* hydroxyl groups on the support, as well as by enhancing the oxidation of Pt.

Chapter 5 describes the adsorption of hydroxyacetone, another model oxygenate for APR, on Pt/AlO(OH) and Pt/ZrO₂ catalysts at 230 °C/ 30 bar studied by *in situ* ATR-IR spectroscopy. Formation of aldol condensation products of hydroxyacetone strongly adsorbed on the surface was observed on Pt/ZrO₂ and ZrO₂ in contrast to Pt/AlO(OH) and AlO(OH). The theoretical IR spectra of the condensation products in vacuum and in the presence of water calculated using DFT methods were used to support peak assignments. The ATR-IR spectra of hydroxyacetone reaction combined with spectra collected during washout with water showed the ability of ATR-IR to detect strongly adsorbed surface species. The amount and type of coke deposits determined by elemental analysis and TPO showed that coke with low oxidation temperatures was deposited mostly on the surface of the ZrO₂ support. Surprisingly, no adsorbed CO was observed in the spectra, suggesting that either CO consumption is not rate-limiting or catalyst deactivation prevents CO adsorption. In order to confirm this, analysis of gas phase products and simultaneous determination of conversion levels is required.

Summarizing, we have shown successfully that ATR-IR spectroscopy is a useful tool for studies of reactions at water/catalyst interface, using APR as an example reaction. Both catalyst structure and surface species can be studied under realistic reaction conditions, suggesting improvements for catalyst development. The applicability of the ATR-IR cell for operation at high temperature and high pressure liquid conditions opens up the possibilities of using this technique for other liquid phase reactions in heterogeneous catalysis, for example hydrogenation reactions.

Краткое содержание

Разработка эффективного катализатора для гетерогенного каталитического процесса включает в себя выявление зависимости между структурой катализатора и его активностью. Спектроскопические методы *in situ* (лат. «на месте», т.е. в реакционной смеси) могут быть использованы для изучения структуры каталитического активного центра и последовательности реакций в условиях реакции. Информация, полученная при помощи таких методов анализа, например, о структуре поверхностного комплекса (вида), ведущего к деактивации катализатора, или об изменениях в структуре катализатора под воздействием условий реакции, может помочь в определении методов по улучшению катализатора. Однако, ограничения в применении данных методов в реальных условиях реакции, а также в присутствии растворителя могут препятствовать проведению *in situ* исследований.

Инфракрасная спектроскопия нарушенного полного внутреннего отражения (ИК-НПВО), рассмотренная в деталях в данной диссертации, является методом изучения поверхности раздела между жидкостью и твердым телом, в частности поверхности раздела между твердым телом и водой. Основной целью исследований, представленных в данной диссертации, является изучение применимости ИК-НПВО спектроскопии для *in situ* исследований поверхности раздела между водой и катализатором в процессе Жидкофазного Реформинга (ЖР). Процесс ЖР протекает при высоких температурах и давлениях (150 - 350 °С и 10 - 50 бар), поэтому необходим подбор и проверка подходящей ячейки-реактора. Результаты, представленные в Главе 2, дают полное описание и дизайн Туннельной ячейки-реактора для *in situ* ИК-НПВО спектроскопии с использованием Элемента Внутреннего Отражения цилиндрической формы, покрытого механически стабильным слоем катализатора. Моделирование гидродинамики жидкостного потока внутри ячейки-реактора показало, что тип потока значительно отличается от реактора идеального вытеснения. Распределение времен пребывания молекул, полученное при моделировании, находится в согласовании с экспериментальными результатами, полученными при изучении водных растворов ацетона и глицерина. Подобное моделирование необходимо для изучения изменений концентрации веществ, происходящих во время реакции, а также для установления операционных режимов во время реакции, а именно переходного или устойчивого состояний. Результаты моделирования также позволяют установить зависимости между изменениями в ИК спектрах и изменениях концентрации веществ во время кинетических экспериментов, что позволит исключить градиенты концентраций, связанные с гидродинамикой потока, и выявить концентрационные профили поверхностных комплексов (видов).

ИК-НПВО спектроскопия в условиях процесса ЖР была применена для изучения превращения гамма оксида алюминия в «бемит» (boehmite, $\text{AlO}(\text{OH})$) под воздействием гидротермических условий. Результаты, представленные в Главе 3, показали, что данное превращение ведет к деактивации катализатора с одновременным спеканием частиц платины и блокированию поверхности платины бемитом. Кроме того, была определена энергия активации превращения гамма оксида алюминия в бемит на основании изменений характеристических ИК спектральных полос. Образование бемита было также подтверждено Рамановской спектроскопией и Твердотельной ЯМР ^{27}Al спектроскопией образцов до и после воздействия гидротермических условий. На основании представленных результатов, находящихся в согласии с другими исследованиями, нами было предложено, что частицы платины препятствуют превращению гамма оксида алюминия в бемит путем присоединения к моно-координированным гидроксильным группам на поверхности гамма оксида алюминия, которые по-видимому являются нуклеационными центрами при образовании бемита. Также было выявлено, что присутствие этиленгликоля в растворе замедляет данное превращение, благодаря образованию углеродистых отложений, которые защищают поверхность от гидроксирования. Кроме этого, было показано, что бемит является устойчивой фазой оксида алюминия в условиях ЖР и в свою очередь является эффективным носителем для платиносодержащих катализаторов при жидкофазном реформинге этиленгликоля. Катализатор $\text{Pt}/\text{AlO}(\text{OH})$ показал высокую активность в образовании водорода. Это может быть вызвано либо (i) обширным гидроксированием поверхности бемита, благоприятствующим бифункциональному механизму реформинга, состоящего из адсорбции углеродистых комплексов на поверхности платины и активации молекул воды путем образования гидроксильных групп на поверхности носителя, либо (ii) увеличенным содержанием оксидов платины.

В Главе 5 представлены результаты адсорбции гидроксиацетона, используемого в качестве модельного соединения в процессе ЖР, на поверхности $\text{Pt}/\text{AlO}(\text{OH})$ и Pt/ZrO_2 катализаторов при $230\text{ }^\circ\text{C}/30\text{ бар}$ с использованием *in situ* ИК-НПВО спектроскопии. Во время экспериментов наблюдалось образование продуктов альдольной конденсации гидроксиацетона, адсорбированных на поверхности Pt/ZrO_2 и ZrO_2 образцов в отличие от $\text{Pt}/\text{AlO}(\text{OH})$ и $\text{AlO}(\text{OH})$ образцов. Теоретические ИК спектры продуктов конденсации, рассчитанные при помощи DFT методов в вакууме и в присутствии молекул воды, были использованы для интерпретации экспериментальных ИК спектров. ИК спектры адсорбции гидроксиацетона вместе со спектрами, полученными при вымывании реагента водой, показали возможность определения структуры сильно адсорбированных поверхностных комплексов (видов) с помощью ИК-НПВО спектроскопии. Количество и тип образованных углеродных отложений были определены при

помощи элементного анализа и термопрограммируемого окисления. Результаты показали, что углеродные отложения имеют низкую температуру окисления и расположены главным образом на поверхности носителя оксида циркония. Кроме того, в ИК спектрах не было обнаружено ИК полос адсорбированного монооксида углерода (CO), что означает либо высокую скорость реакции потребления CO, либо предотвращение образования CO за счет деактивации катализатора. Требуется дополнительный анализ газофазных продуктов и одновременное определение конверсии реагента для подтверждения данного предположения.

Таким образом, мы показали, что *in situ* ИК-НПВО спектроскопия является полезным инструментом в исследованиях реакций на поверхности раздела между водой и катализатором, в особенности в процессе жидкофазного реформинга. Структура катализатора, а также поверхностные комплексы (виды) могут быть исследованы в реальных условиях реакции, предлагая способы улучшения катализатора. Применимость ячейки-реактора для ИК-НПВО спектроскопии в изучении реакции при высоких температурах и давлениях в присутствии растворителя открывает широкий спектр возможностей по использованию данного метода для изучения других жидкофазных реакций в гетерогенном катализе, таких как, например, реакций гидрирования.

Samenvatting

Ontwikkeling van een efficiënte katalysator voor heterogene katalyse omvat het begrip van de relatie tussen de structuur van katalysator en zijn activiteit. Methoden van *in situ* spectroscopie kunnen gebruikt worden om de structuur van het katalytisch actieve centrum en reactiesquenties onder reactieomstandigheden te studeren. Informatie verkregen van dergelijke analyse methoden, bijvoorbeeld de structuur van de oppervlakte-molecuul-soorten of veranderingen in de structuur van de katalysator onder reactieomstandigheden, kan gebruikt worden om manieren te vinden om de katalysator te verbeteren. De gelimiteerde toepasbaarheid van de methoden kan, onder echte reactieomstandigheden en met name in aanwezigheid van een oplosmiddel, een uitdaging zijn voor *in situ* onderzoeken.

Attenuatie van de Totale Reflectie Infrarood Spectroscopie (ATR-IR), wat in detail besproken is in dit proefschrift, is een techniek die wordt gebruikt om de interface tussen vaste stoffen en vloeistoffen te bestuderen. Het belangrijkste doel van dit proefschrift is de toepasbaarheid van de ATR-IR spectroscopie om de water-katalysator interface te bestuderen in de Aqueous Phase Reforming (APR) reactie. De APR reactie vereist hoge temperaturen en drukken (150 - 350 °C and 10 - 50 bar). Daarom moest er eerst een geschikte ATR-IR cel (reactor) ontworpen en getest worden voor deze omstandigheden. De resultaten gepresenteerd in Hoofdstuk 2 beschrijven het ontwerp van een *in situ* ATR-IR Tunnel cel met een cilindrisch Interne Reflectie Element dat is bekleed met een mechanisch stabiele katalysatorlaag. Simulatie van de hydrodynamica van de stroming heeft niet-propstroomgedrag in de cel vertoond. Verblijftijd distributies van moleculen verkregen uit simulaties, komen overeen met de experimentele resultaten voor aceton en glycerol oplossingen. Een dergelijke simulatie is essentieel om concentratie wijzigingen tijdens de reactie te ondersteunen en een operationeel modus vast te stellen, d.w.z. transiente of stabiele staat. De resultaten van de simulatie maken het ook mogelijk om te correleren tussen wijzigingen in IR spectra en concentratie wijzigingen in kinetische experimenten, wat het mogelijk maakt om wijzigingen dankzij hydrodynamica van de stroming uit te sluiten en om de concentraties van oppervlakte-molecuul-soorten te volgen.

De toepasbaarheid van ATR-IR spectroscopie onder APR omstandigheden is gedemonstreerd door het bestuderen van de real-time transformatie van $\gamma\text{-Al}_2\text{O}_3$ naar boehmiet onder hydrothermale omstandigheden. Resultaten van Hoofdstuk 3 en 4 tonen aan dat deze transformatie leidt tot deactivatie van de katalysatorsamen met het sinteren van het Pt en dekking van het Pt-oppervlak met boehmite. Activatie energie van de transformatie van $\gamma\text{-Al}_2\text{O}_3$ in boehmiet was berekend gebaseerd op karakteristieke IR spectrale intensiteiten. De formatie van boehmiet was vastgesteld met Raman spectroscopie en met een ^{27}Al MAS NMR analyse van monsters voor en na belichting in APR omstandigheden. Gebaseerd op verkregen resultaten en in

overeenkomst met andere studies, werd voorgesteld dat Pt de transformatie hindert door een verbinding met mono-gecoördineerde OH-groepen van $\gamma\text{-Al}_2\text{O}_3$, die nucleatie centers lijken te zijn voor de transformatie naar boehmiet. Het inhiberende effect van ethyleenglycol werd aangetoond dankzij de formatie van koolstofhoudende afzettingen die het oppervlak van hydroxylatie beschermen. Daarnaast werd aangetoond dat boehmiet een stabiele fase van aluminiumoxide onder APR omstandigheden is en een efficiënte ondersteuning voor Pt-gebaseerde katalysatoren in APR van ethyleenglycol is. Bovendien heeft de Pt/AlO(OH) katalysator een goede activiteit in waterstof productie getoond. Dit zou veroorzaakt kunnen worden door (i) een uitgebreide hydroxylatie van het boehmiet oppervlak, wat mogelijk het bifunctionele mechanisme van APR begunstigt met adsorberende koolstofhoudende molecuul-soorten en water activatie via hydroxyl groepen op de ondersteuning en door (ii) een verbeterde oxidatie van Pt.

Hoofdstuk 5 beschrijft adsorptie van hydroxyaceton, een ander model oxygenaat voor APR, over Pt/AlO(OH) and Pt/ZrO₂ katalysatoren bij 230 °C/ 30 bar bestudeerd met behulp van *in situ* ATR-IR spectroscopie. Vorming van aldol condensatie producten van hydroxyaceton, die sterk zijn geadsorbeerd, werd op het oppervlak van Pt/ZrO₂ en ZrO₂ gezien, in tegenstelling tot het oppervlak van Pt/AlO(OH) en AlO(OH). De theoretische IR spectra van condensatieproducten in vacuum en in aanwezigheid van water moleculen, berekend met DFT methoden, werden gebruikt om IR piek toewijzingen te ondersteunen. De ATR-IR spectra van de hydroxyaceton reactie in combinatie met de spectra verkregen tijdens de uitspoeling met water toonden aan dat ATR-IR spectroscopie de mogelijkheid heeft om sterk geadsorbeerde oppervlakte-molecuul-soorten te ontdekken. De hoeveelheid en het type coke afzettingen, bepaald met behulp van element analyse en Temperatuur Geprogrammeerde Oxydatie (TPO) analyse, toonden aan dat coke met lage oxydatie temperaturen voornamelijk op het oppervlak van de ZrO₂ ondersteuning afzetten. Verrassend genoeg was er geen adsorbeerde CO in de spectra gezien, wat suggereert dat of CO consumptie niet snelheidsbeperkend is of deactivatie van de katalysator CO adsorptie voorkomt. Om dit te bevestigen is een analyse van de gasfase producten en tegelijkertijd een bepaling van de conversie nodig.

In conclusie, wij hebben met success aangetoond dat ATR-IR spectroscopie een bruikbare methode is voor het bestuderen van reacties op een water/katalysator interface, met een APR reactie als voorbeeld. Zowel katalysator structuur als oppervlakte-molecuul-soorten kunnen bestudeerd worden onder realistisch reactie omstandigheden, wat voor een verbeteringen in de ontwikkeling van katalysatoren kan zorgen. De toepasbaarheid van de ATR-IR cel om onder hoge temperaturen en drukken in vloeibare condities te werken, stelt mogelijkheden open om andere vloeibare fase reacties in heterogene katalyse te onderzoeken, bijvoorbeeld hydrogenatie reacties.

Acknowledgements

This thesis would not exist without the help of many people, who have contributed scientifically, intellectually and emotionally. I would like to thank them all in this chapter.

First, I would like to thank my supervisors, Prof. K. Seshan and Prof. Leon Lefferts for offering me a PhD position in Catalytic Processes and Materials group at the University of Twente. I can say with confidence that your guidance, support, comments and suggestions throughout these years have helped me a lot in becoming a good scientist. Seshan, I knew I could always come to you with any crazy scientific question and you would always help me. I appreciate your curiosity in learning more about my country and my culture and that you always asked about my life outside work. Leon, it was a challenging project, where both of us had to learn more about the topic. I thank you for your fast and critical comments about my papers. I am sure that your input made them much more professional and well structured. I also appreciate your honesty during our discussions that we had in France.

I would like to thank my daily supervisor Dr. Barbara Mojet, who introduced me into the world of IR spectroscopy and spectra processing. Barbara, your enthusiasm and open mind always inspired me for new ideas and gave the motivation for new work. I will always remember our long meetings where we discussed not only the results, but also general questions about research world. I wish you lots of health and success in everything you do.

I am also thankful to committee members for the time they spent evaluating my work and for their comments.

The work would not be complete without contributions of our collaborators. Dr. Francesco Ferrante and Dr. Remedios Cortese from Università degli Studi di Palermo have helped with DFT calculations of condensation products. Prof. Rob Lammertink and Aura Visan have performed simulations of the flow hydrodynamics in the Tunnel cell. Dr. Karthick Babu Sai Sankar Gupta has performed NMR analysis of the alumina samples. I am very grateful for your help and for the fruitful discussions.

Dr. Mark Smithers and Dr. Rico Keim deserve special mentioning for their beautiful TEM and SEM images of the catalysts and catalyst layers.

The project would not be successful without the technical knowledge and skills of Ing. Bert Geerdink, who has contributed enormously in building the setup and troubleshooting during experiments. Bert, I really appreciate your advices not only about the equipment, but also about life. Thanks for being supportive and protecting and for all the lessons that you taught me.

Thanks to professionalism and support of CPM secretaries Maaïke de Jong, Lidy Harryvan and Sabine Hartman, I always had my documents and other paperwork in good order. Thank you for your great work and personal approach.

I would like to thank Ing. Louise Vrieling, Ing. Tom Velthuis and Karin Altena for their technical and analytical help in the lab, and for their friendliness and warm hearts. I would specially like to thank Tom for helping me with the Dutch translation of the summary.

I had an excellent opportunity to supervise a bachelor student, Marcel Klompmaker, during my project. Marcel, thank you for your willingness to learn and productive time we have spent in the lab.

There are not enough words to describe all the help and support that I received from current and former CPM members, who have become a family to me. Joline van Beek, Roger Brunet Espinosa, Guido Giammaria, Tushar Sakpal, Marta Albuquerque Machado, Reza Taheraslani, Kaisa Vikla, Songbo He, Pramod Chodimella, Chau Hoang, Son Nguyen, Cristina Franch, Koteswara Rao Nidadavolu, Heikki Harju, Marijana Kovačević, Masoud Zabeti, Ganesan Raman, Arturo Susarrey Arce, Shilpa Agarwal, Dennis de Vlieger, Sergio Pacheco Benito, Chris Reed, José Medrano Catalán, Vijay Thakur, Ruben Lubkemann, Yejun Guan, Gonzalo Ríos Cruellas, Annemiek te Boekhorst, Yingnan Zhao, Arie van Houselt – thank you all! I am truly grateful for the wonderful moments that we have shared in the lab, at the coffee table, during our borrels, group trips, international dinners and conferences. Getting to know so many motivated, inspired, funny and friendly people from all over the world that was the best thing I have experienced in the Netherlands.

I would also like to thank friends I met during lindy hop lessons in Swing Out Loud - Jolet de Ruiten, Riëlle de Ruiten, Erik Linnartz, Dieter 't Mannetje, Erik Garbacik, Kathrin Surmann, Erik Nieland and others - for the great fun we had during dancing.

My special thanks go to my paranymphs Roger Brunet Espinosa and Kaisa Vikla. Apart from scientific discussions, we have shared many nice moments talking, eating and playing games. Thank you for supporting me on my PhD defense day.

This thesis would not exist without one man, his name is Andrew Fussell. Andrew, I cannot express how much I am grateful to you. I thank you for believing in me, supporting me every day and being a good motivator for new achievements. I am very happy that I came to Enschede and met you.

Finally, I would like to thank my family for supporting me in everything I do, even though long distances separate us. Мама и папа, спасибо за вашу поддержку, веру в меня и за все, что вы вложили в мое воспитание и обучение. Я очень рада, что вы держите в своих руках результат моего труда и можете гордиться мной. Аселя, несмотря на расстояния между нами, я всегда знаю, что ты веришь в меня и поддерживаешь. Апашка, Аймана-тате, Данияр-ага, Айнагуль-эже, спасибо за ваши теплые слова и постоянную поддержку. Без вас, моя семья, я бы не стала тем, кто я есть сейчас. Вы – моя команда! Спасибо.

Scientific Contributions

Publications:

K. Koichumanova, A.K.K. Vikla, D.J.M. de Vlieger, K. Seshan, B.L. Mojet, L. Lefferts
Towards Stable Catalysts for Aqueous Phase Conversion of Ethylene Glycol for Renewable Hydrogen,
ChemSusChem, Volume 6, Issue 9, p. 1717–1723, **2013** (Chapter 3)

K. Koichumanova, K.B. Sai Sankar Gupta, L. Lefferts, B. L. Mojet, K. Seshan
In situ ATR-IR spectroscopy study of aluminas under aqueous phase reforming conditions,
Physical Chemistry Chemical Physics, accepted, **2015** (Chapter 4)
DOI: 10.1039/C5CP02168E

K. Koichumanova, A.K.K. Vikla, R. Cortese, F. Ferrante, K. Seshan, D. Duca, L. Lefferts
In-situ ATR-IR studies in aqueous phase reforming of hydroxyacetone on zirconia and boehmite supported Pt catalysts: the role of aldol condensation reaction, to be submitted to **ACS catalysis**, **2015** (Chapter 5)

K. Koichumanova, A. Visan, B. Geerdink, R.G.H. Lammertink, B.L. Mojet, K. Seshan, L. Lefferts
ATR-IR spectroscopic cell for in situ studies at solid-liquid interface at elevated temperatures and pressures, to be submitted to **Applied Spectroscopy**, **2015** (Chapter 2)

Conference contributions:

Oral presentations:

Kamila Koichumanova, K. Seshan, L. Lefferts (May **2015**)
International Congress Operando V, Deauville, France
“High temperature and pressure ATR-IR spectroscopy study of Aqueous Phase Reforming of Hydroxyacetone on Pt/zirconia and Pt/boehmite”

K. Koichumanova, L. Lefferts, K. Seshan, B.L. Mojet (June, **2013**)
23rd Northern American Catalysis Society Meeting (NAM), Louisville, KY, USA
“High Temperature and High Pressure Infrared Spectroscopy for heterogeneous liquid phase catalysis”

K. Koichumanova, L. Lefferts, K. Seshan, B.L. Mojet (March **2014**)

XV Netherlands Catalysis and Chemistry Conference, Noordwijkerhout, The Netherlands

“High temperature and pressure ATR-IR spectroscopy study of catalyst support in catalyst development for Aqueous Phase Conversion of Ethylene Glycol”

K. Koichumanova, L. Lefferts, K. Seshan, B.L. Mojet (28-29 January **2014**)

CatchBio Progress Meeting, Amsterdam, The Netherlands

“In-situ ATR-IR studies in Aqueous Phase Reforming”

K. Koichumanova, L. Lefferts, K. Seshan, B.L. Mojet (23-24 January **2013**)

CatchBio Progress Meeting, Nunspeet, The Netherlands

“High Temperature and High Pressure Infrared Spectroscopy for heterogeneous liquid phase catalysis”

Poster presentations:

K. Koichumanova, A.K.K. Vikla, B.L. Mojet, L. Lefferts, K. Seshan (March **2015**)

XVI Netherlands Catalysis and Chemistry Conference, Noordwijkerhout, The Netherlands

“High temperature / pressure ATR-IR spectroscopy in Aqueous Phase Reforming of Hydroxyacetone on Pt/zirconia and Pt/boehmite catalysts”

K. Koichumanova, L. Lefferts, K. Seshan, B.L. Mojet (March **2013**)

XIV Netherlands Catalysis and Chemistry Conference, Noordwijkerhout, The Netherlands

“High Temperature and High Pressure Infrared Spectroscopy for heterogeneous liquid phase catalysis”

K. Koichumanova, L. Lefferts, K. Seshan, B.L. Mojet (March **2012**)

XIII Netherlands Catalysis and Chemistry Conference, Noordwijkerhout, The Netherlands

“ATR - IR studies in aqueous phase reforming”

K. Koichumanova, L. Lefferts, K. Seshan (September **2011**)

CatchBio Poster session Mid-Term Review, Urmond, The Netherlands

“ATR - IR studies in aqueous phase reforming”

Kamila Koichumanova was born in Almaty, Kazakhstan in 1987. She received her Bachelor degree in Chemical Engineering in 2008 from Lomonosov Moscow State Academy of Fine Chemical Technology. In 2010, she received her Master degree from the same university with specialization in Petrochemical Synthesis and Artificial Liquid Fuel Engineering. During her Master project she worked on isobutane alkylation using zeolites. In 2010, she started PhD project in Catalytic Processes and Materials group at the University of Twente, The Netherlands, on Application of Attenuated Total Reflection FTIR spectroscopy in Aqueous Phase Reforming. The results of the PhD research are presented in this book.



UNIVERSITY OF TWENTE.

ISBN 9789036539630



9 789036 539630